We are IntechOpen,
the world's leading publisher of
Open Access books
Built by scientists, for scientists

4,800
Open access books available

122,000
International authors and editors

135M
Downloads

Our authors are among the

154
Countries delivered to

TOP 1%
most cited scientists

12.2%
Contributors from top 500 universities

CLARIVATE ANALYTICS
BOOK CITATION INDEX
INDEXED

WEB OF SCIENCE™

Selection of our books indexed in the Book Citation Index
in Web of Science™ Core Collection (BKCI)

Interested in publishing with us?
Contact book.department@intechopen.com

Advanced Nanomatericals for Solar Photocatalysis

Le Li and Minqiang Wang

Abstract

Heterogeneous photocatalysis using semiconductors and renewable solar energy has been regarded as one of the most promising processes to alleviate and even solve both the world crises of energy supply and environmental pollution. Recently, numerous semiconducting materials and its composites have been studied for their photocatalytic applications. In this chapter, we briefly summarize recent progress in the binary oxide system (including TiO_2 and α-Fe_2O_3), ternary oxide (Bi system), and the semiconducting materials and their composites which have remarkable applications in photocatalytic degradation of toxic pollutants, hydrogen production and as an adsorbent for wastewater treatment. In addition, we highlight the challenges and opportunities when we implement photocatalytic materials to help on the development of energy research and find ways to approach major problems.

Keywords: Photocatalysis, TiO_2, α-Fe_2O_3, $BiVO_4$, Bi_2WO_4, BiOX, Binary oxide, Ternary oxide

1. Introduction

Ever-increasing environmental issues and consumption of fossil fuels have stimulated extensive research on the utilization of sustainable solar energy [1]. The extensive use of fossil fuels has led to a serious energy crisis and environmental pollution, which are the two major challenges facing the world in the 21st century. Among the many advanced technologies available today, heterogeneous photocatalysis in view of semiconductors taking advantage of regeneration solar energy has been identified as one of the most prospective strategies for resolving both the environmental and energy problems and has thus caused much attention during the recent decades [2–4]. In the past decades, numerous results have been reported for photocatalysis and their applications to produce hydrogen from water (see Fig.1 a) [5–8], convert solar energy into electric energy (see Fig.1 b) [9,10], degrade organic pollutants (see

Fig.1 c) [11–13] and reduce CO_2 into organic fuels (see Fig.1 d) [13–15]. Besides the naturally abundant in nonrenewable energy sources such as solar energy can be renewed into chemical or electrical and thermal energies by using semiconductors having persisting materials in the process of photocatalysis [17-20]. Generally speaking, the mechanism of a typical power-driven photocatalysis process is mainly owing to three critical related synergistic steps: (i) light absorption and charge excitation; (ii) charge separation and transport from the semiconductor particle to its surface active sites; (iii) surface photocatalytic chemical reactions, and this process is similar to the fundamental mechanism of photocatalysis in power systems.
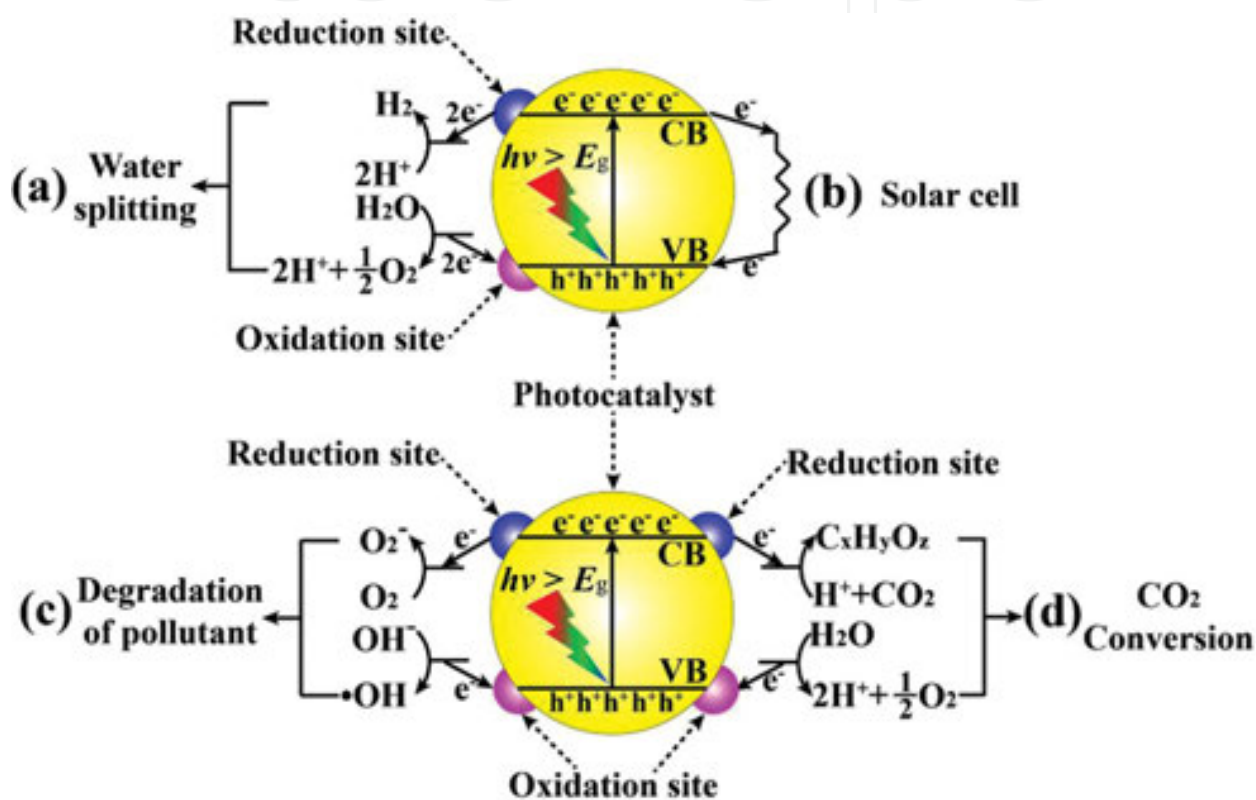

Figure 1. Photocatalytic mechanisms of water splitting, solar cell, degradation of pollutants, CO_2 reduction via one-step photoexcitation. CB and VB represent the conduction and valence bands, respectively [16].

Typically, the electron-hole pair with specific reduction and oxidation potential will be created on its conduction band (CB) and valence band (VB) under the irradiation of incident light with energy greater than the band gap of a given semiconductor. Here, the band gap of the semiconductor determines the utilization rate of the energy of the incident light, and the CB and VB values are the origin of the reduction and oxidation abilities of the photoexcited electrona and holes [21]. However, in practical process, the performance of photocatalysts is mainly related to two conditions: (i) the energy (hv) of the incident photon should be larger than the energy gap (Eg) of the photocatalyst; (ii) the redox potential of reactants should be located between the CB and VB of the semiconductor photocatalyst. One the one hand, the former condition indicates a narrow band gap, which can facilitate the efficient utilization of

incident solar-light. On the other hand, the latter condition demonstrate that a more higher CB potential and a more lower VB potential, which are thermodynamically beneficial for the reduction and oxidation reactions of the reactants, respectively. But a high CB and low VB potential means a broad band gap of a photocatalyst, which leads to the poor solar–light utilization as discussed in condition (i). It is obvious that these conditions above are mutually contradiction, and it is important to find the balance point to design the photocatalyst. However, for a single component photocatalyst, it is difficult to possess both wide light –absorption range and strong redox ability concurrently. Besides, in the single-component structure, the photogenerated electrons in the CB can easily return to the VB or trap in the defect state and recombine with the holes, which seriously reduces the utilization efficiency of solar energy [22-24]. Hence, designing appropriate heterogeneous photocatalytic systems should be an effective way to overcome this problem.

The chapter is divided into four main sections. In the first part, we describe the importance of binary oxide system photocatalytic matericals in the case of two prominent and widely studied matel oxides: Titania (TiO_2), hematite (α-Fe_2O_3). In the second part, we do focus on materials with a specific ternary oxide photocatalytic matericals, such as Bi systems photocatalytic materials. In the third part, we discuss the semiconducting materials and its composites which have promising applications in the area of energy and environment especially in photocatalysis. In the end, we highlight the challenges and opportunities on the way to implement photocatalytic materials to help on the development of energy research and finding ways to approach for the major problems. Hence, we believe that a comprehensive chapter on advanced nanomatericals for solar photocatalytic is desirable for the further development of the novel photocatalytic materials and deeper understanding of photocatalytic mechanisms will be achieved in the near future, through more fundamental interdisciplinary research.

2. Binary oxide system

2.1. TiO_2

TiO_2 has turned out to be one of the most commonly investigated semiconductors due to its low cost, long–term thermodynamic stability in aqueous solution, low toxicity, and high efficiency in the removal of pollutants in water and air as well as hydrogen generation [25-28]. There following are the four commonly known polymorphs of TiO_2 found in nature: anatase (tetragonal), rutile (tetragonal), brookite (orthorhombic), and TiO_2(B) (monoclinic) [29,30]. Rutile TiO_2 has a tetragonal crystal structure and contains six atoms per unit cell as shown in Fig. 2 [31]. Rutile is the most thermodynamically stable polymorph of TiO_2 at all temperatures, exhibiting lower total free energy than metastable phases of anatase and brookite. Anatase TiO_2 has a crystalline structure that corresponds to the tetragonal system but the distortion of the TiO_6 octahedron is slightly larger for the anatase phase. Anatase is the most commonly used in photocatalytic applications due to its inherent superior photocatalytic properties [32-34].
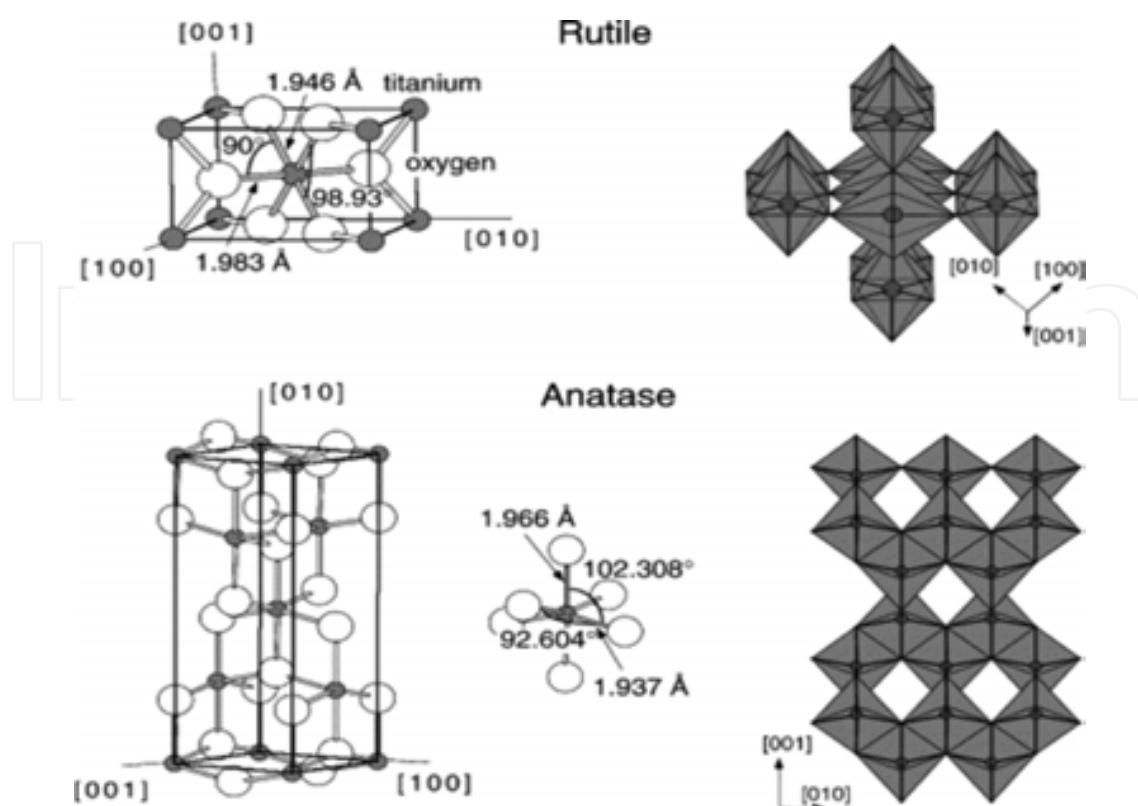
Figure 2. Representations of the TiO$_2$ anatase and rutile forms [31].

Anatase is the least thermodynamically stable TiO$_2$ polymorph as a bulk phase, although, from energy calculations, it appears as the most stable phase when the grain size is below 10–20 nm [35,36]. The crystalline structure of the TiO$_2$ oxides can be described in terms of TiO$_6$ octahedral chains. These differ by the distortion of each octahedron and the assembly pattern of the resulting octahedral chains. The Ti–Ti distances in the anatase structure are greater than in rutile, while the Ti–O distances are shorter [37]. These structural differences lead to different mass densities as well as different electronic band structures. As a result, the anatase phase is 9% less dense than rutile and it presents more pronounced localization of the Ti 3d states and further a narrower 3d band. Also, the O 2p–Ti 3d hybridization is different in the two structures. Anatase exhibits a valence and conduction band with more pronounced O 2p–Ti 3d character and less nonbonding self-interaction between similar ions (e.g., anion-anion and cation-cation interactions) [38]. The importance of the covalent vs ionic contributions to the metal-oxygen bond has already been discussed in a more general context for Ti oxides [39,40]. Therefore, it could be claimed that differential structural characteristics between anatase and rutile of TiO$_2$ are possibly attributed to the difference in the mobility of the charge carriers upon light excitation.

In 1972, K. Honda and A. Fujishima discovered the photosensitization effect of a TiO$_2$ electrode on the electrolysis of H$_2$O into H$_2$ and O$_2$ using a Pt metal electrode as cathode and a TiO$_2$ photoanode irradiated with UV light. They found that, under UV light irradiation of the TiO$_2$ electrode, the electrolysis of H$_2$O proceeded at a much lower bias voltage as compared

with normal electrolysis [41]. From then on, the TiO_2-based photocatalyst have been exten‐ sively studied in the past few decades due to its proper energy bandgap that matches the UV −visible light irradiation, which favors many light-driven applications [42-47]. Moreover, TiO_2 has got many advantages and the nature of this material is naturally abundant, commer‐ cially available, economically viable, chemically stable, non-toxic and environmental eco −friendly [44]. However, TiO_2 has also faced few problems as photocatalysts in applying solar energy processes due to its low sunlight spectrum matching, limited activity and reduced sensitivity [48]. To overcome this shortage, recently many researchers have developed many different modification methods to TiO_2 material to make it as a potential challenging material for highly active photocatalyst [48-55]. Among these works, crystal growth, doping and heterostructuring of semiconductor photocatalysts are commonly used and can substantial tune the light-response range, redox potentials of photoinduced charge carriers, and electron-hole pair separation probability within the photocatalysts. Specifically, crystal growth can be critical in controlling the phase, shape, and size of photocatalysts, as well as their crystallinity and specific surface area. By rationally controlling crystal growth, the intrinsic surface atomic structure and resultant surface states of the derived photocatalysts can be adjusted. For materials design, doping effect can exert a substantial influence on modifying the electronic structure and the construction of heteroatomic surface structures of the aiming material. In particular, nonmetal doping (N [56,57], C [58-60], S [61,62], B [63-65], F [66-68], Br [69], I [70-73], P [74]) in photocatalyst has attracted increasing attention due to its effectiveness in realizing visible−light photocatalytic activity of wide bandgap semiconductor photocatalysts. The chemical states and locations of dopants are considered to be key factors in adjusting the spectral distribution of the induced electronic states of those dopants and reconstructing favorable surface structure for photocatalysis. The hybrids of two or more semiconductor systems, that is, heterostructures, seem to be possess advantageous in more efficiently utilizing solar light by combining different electronic structures when compared with sing-phase semiconductor photocatalysts. Furthermore, an efficient photo-excited electron or hole transfer from one component to another with proper band edge matching can greatly decrease the electron-hole recombination probability and increase the lifetime of charge carriers, which further promoting the photocatalytic efficiency. In addition to the basic requirements of electronic structure for each unit in the integrated photocatalytic systems, a favorable interface contact between the two materials is essential in promoting interface charge carrier transfer through different pathways. Fig. 3 demonstrates the connection between crystal growth, doping and hetero-structure of semiconductors for heterogeneous photocatalysis, (CB: conduction band; VB: valence band) [75].

According to the Wulff construction and calculated surface energy, the shape of anatase under equilibrium conditions is a slightly truncated tetragonal bipyramid enclosed with eight isosceles trapezoidal surfaces of {101} and two top squares of {001}, as shown in Fig. 4 [76] It is predicted that the percentage of {101} is as high as 94%. Although the surface energy of {010} (0.53 J m $^{-2}$) was calculated to be between {001} (0.90 J m $^{-2}$) and {101} (0.44 J m $^{-2}$) [77], it is surprising that no {010} will appears in the equilibrium shape of anatase. Anatase TiO_2 is usually exposed with low-index facets. Theoretical calculations indicate that the (101) surface (0.44 J m^{-2}) is the thermodynamically the most stable surface, the (001) surface (0.90 J m^{-2}) is
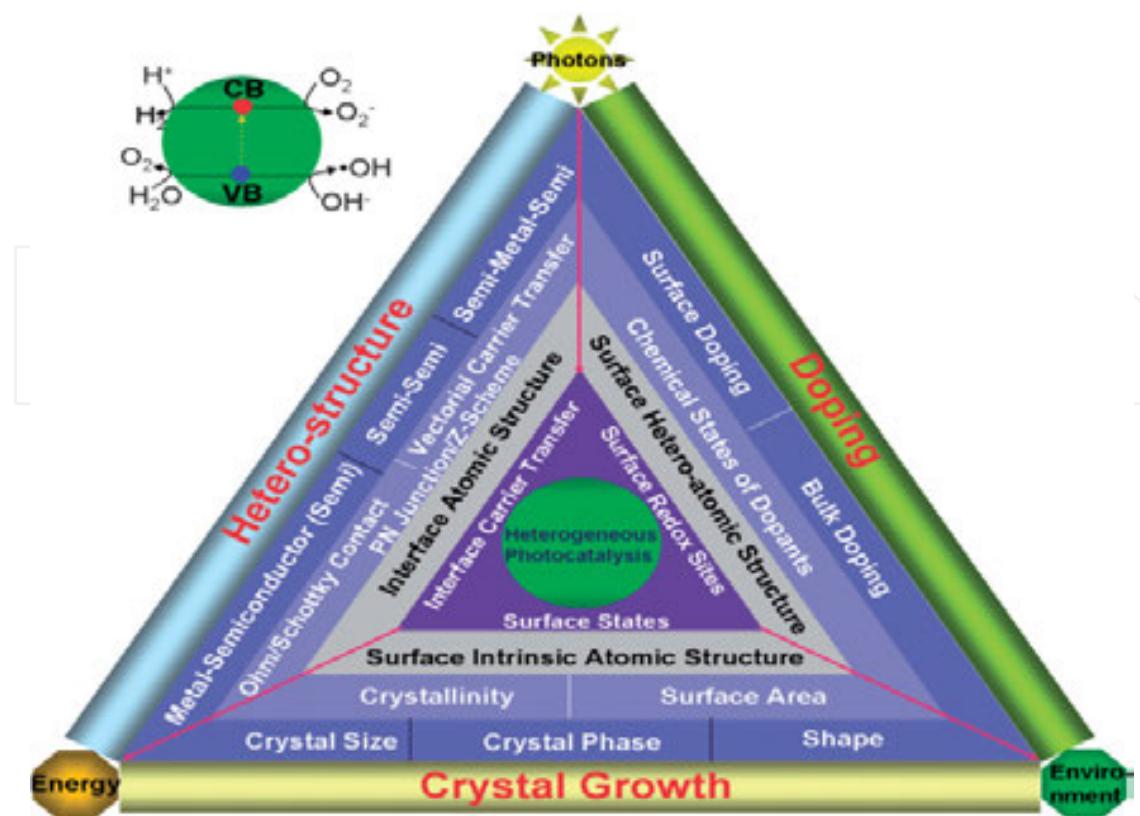
Figure 3. Correlation of key factors in crystal growth, doping and heterostructuring of semiconductors for photocatalysis. (CB: conduction band; VB:valence band) [75].

the most active and the (100) and (110) surfaces are between the (101) and (001) surfaces. As a consequence, facets that have a high surface energy diminish quickly in the minimization of surface energy during the crystal-growth process. Therefore, a large percentage of high active facets has become a popular target in the synthesis of anatase TiO_2 crystals. In the case of rutile, the predicted equilibrium shape of a macroscopic crystal was constructed with (110), (100), (001) and (011) faces (see Fig. 4) [78]. It is found that in the equilibrium shape, the most stable (110) face with the lowest surface energy of 15.6 meV au^{-2} dominates the shape, whereas (001) with the highest surface energy of 28.9 meV au^{-2} does not exist at all. Gong et al. demonstrated the systematic results of the structures and energetics of 10 stoichiometric 1×1 low-index surfaces with different possible terminations of brookite [79]. The determining factors of the relative stabilities of different faces are found to be negatively related to the concentration of exposed coordinatively unsaturated Ti atoms. The equilibrium shape of brookite crystal is shown in Fig. 4, we can observe that the most of it is composed of (111), (210), (010) and reconstructed (001) facets. It is worth noting that brookite (210) is one of the most stable facets, which has a very similar atomic structure to the most stable facet (101) of anatase. However, their electronic states are different, which may result in different chemical reactivities [80].

Usually, different facets of a single–crystalline material possess distinctive adsorption, catalytic reactivity and selectivity, which are caused by its different geometric and electronic structures [81]. Since Lu and his coworkers first reported that the uniform anatase single
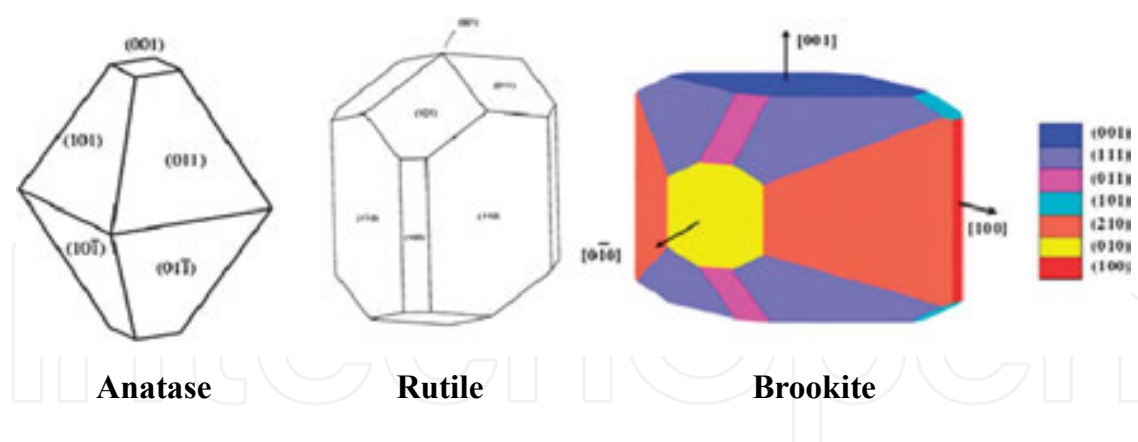
Figure 4. The equilibrium shape of a TiO_2 crystal in the anatase, rutile and brookite, according to the Wulff construction and the calculated surface energies [76, 78,79].

crystals with 47% {001} facets displayed superior photoactivity [82], crystal facet engineering has proven to be an effective strategy to finely tune the efficiency and selectivity of heterogeneous photocatalysts for different applications. Besides, different crystal facets can also facilitate the separation of electrons and holes [83]. To date, many improved synthesis procedures have been successfully developed and lots of exciting advances have been achieved [84-99]. Lu and coworkers demonstrated that, under UV light irradiation, the sheet-like anatase TiO_2 crystal dominated by {001} facets is capable of producing OH that is more than five times higher than that of Degussa P25 TiO_2 [85]. They concluded that the high density unsaturated five-fold Ti and their unique electronic structures of the {001} facets should be responsible for the improved photoactivity. Similar results also have been reported by other groups. For example, Han et al. [84] reported that the photocatalytic ability of TiO_2 nanosheets with {001} facets was higher than that of P25 in the degradation of methyl orange(MO) molecules. Zhang et al. [86] successfully synthesized the a remarkable 80% level of reactive {001} facets microsheet anatase TiO_2 single–crystal photocatalyst, which exhibited much better photocatalytic performance in the oxidative decomposition of organic pollutant. By tuning the percentage of the {001} facets, the photoreactivity was enhanced from 40.0% to 84.5%. The reactive {001} facets played an important role in the photocatalytic reaction owing to their strong ability to dissociatively adsorb water to form hydrogen peroxide and peroxide radicals. Although high-energy {001} facets have been widely studied, anatase TiO_2 crystals with higher-energy {100} facets have been less well developed. Recently, Li and Xu [100] reported a facile hydrothermal route for the synthesis of tetragonal–faceted nanorods (NRs) of anatase TiO_2 with highly exposed higher-energy {100} facets, which exhibited higher reactivity owing to the large percentage of {100} facets compared with crystals that have normal majority {101} facets.

These results discussed above demonstrated that a higher density of surface–unsaturated atoms will lead to a high surface energy of the crystal facets, which generally exhibit better photocatalytic performance. However, recent studies have shown that a high surface energy does not always make the crystal facets highly reactive in photocatalytic reactions. For example, Liu et al. [97] demonstrated a raised conduction band of nanosized single crystals of anatase TiO_2 with 82% {101} facets compared to the crystals with 72% {001} facets, which is

determined by UV/Vis adsorption spectroscopy. This different electronic–band difference will further lead to a difference in atomic coordination, and this decrease will result in an enhanced photoactivity in the splitting of water into hydrogen. This example shows that the band-gap of crystal facets or crystal plates will change as the change in the arrangement of surface atoms. As a result, the redox power of the photoexcited electrons and holes will be correspondingly changed.

Generally speaking, the {101} facets are more reductive than {001} facets, which could act as possible tanks of photogenerated electrons, while {001} facets act as oxidation sites, which play a major role in the photooxidative processes [101,102]. For example, Pan et al. reported that low–index facets of anatase TiO_2 follow the photoreactivity order of {001} < {101} < {010} for photocatalytic hydrogen evolution and·OH radical generation [103]. Similarly, a seeded growth technique also demonstrated that the {101} facets of anatase TiO_2 are more active than the {001} facets for photocatalytic water splitting [104]. Surprisingly, it was even found that the photocatalytic activity for H_2 production over the {111} facet exposed anatase TiO_2 is about 5, 9, and 13 times higher than that of the TiO_2 sample exposed with dominant {010}, {101}, and {001} facets, respectively [105]. However, most researchers ignored the synergetic effects of various co-exposed facets in one sample. More attention has to be paid to finding special facets rather than the balanced ratio of different exposed facets for the best photocatalytic efficiency of water splitting.

Recently, Yu's group found that an optimal ratio of the exposed {101} and {001} facets of TiO_2 played a significant role in the enhancement of photocatalytic performance for the reduction of CO_2 [106]. As shown in Fig. 5, the surplus electrons on the {101} facets will overflow onto the {001} facets and then have a fast recombination with the holes on the {001} facets if the percentage of {101} facets is too low to hold all the photoexcited electrons, this process will lead to a decrease in the photocatalytic activity. The results clearly showed that it is of great importance to find the balanced ratio of different exposed facets in achieving the best photo-catalytic efficiency [107]. This finding may shed light on the design and fabrication of advanced nanosheet-based semiconductors for water splitting.
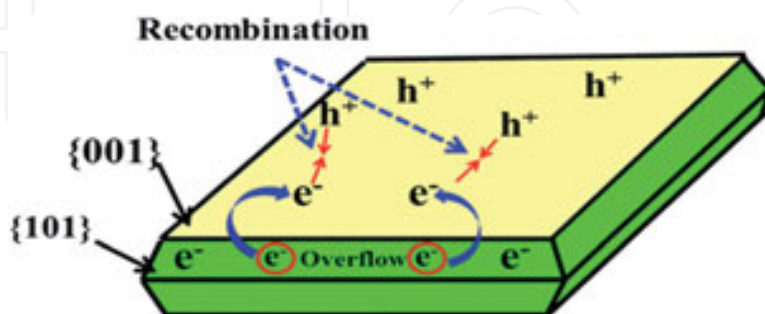

Figure 5. The electron overflow effect on the {101} facets of TiO_2 [107].

In 2011, crystal facet dependence of TiO_2 photocatalysis has been evidenced by using single-molecule imaging and kinetic analysis [108]. Single–particle spectroscopy (microscopy) has been used to explore the structural and kinetic features of "bulk" catalysis because of its high

sensitivity and selectivity. This study demonstrated that the reaction sites for the effective reduction of the probe molecules were preferentially located on the {101} facets of the crystal rather than on the high surface energy {001} facets. This preference originated from the unique properties of the {101} facets in terms of their electron-trapping probability induced by the specific facet. This observation emphasizes the important role of the {101} surfaces as the reductive site in TiO_2 photocatalysis and is in agreement with the conclusion that the reactivity of the {001} facets towards oxidation is higher than that of the {101} facets.

This aforementioned investigation shows that the reactivity of a photocatalyst can be controlled by tuning the exposed facets. Another tool-morphology control, which means the formation of different surface facets with different surface atomic structures, also provides an effective method to tune the selectivity of the photocatalysts. For example, Liu et al. [95] reported a fluoride-mediated self-transformation method for fabricating hollow TiO_2 microspheres (HTS) with anatase polyhedra with about 20% exposed {001} facets. The fluorinated HTS exhibited preferential decomposition of methyl orange (MO) compared with methyl blue (MB). In contrast, surface-modified HTS that was either washed with NaOH or calcined at 600°C favored the decomposition of MB over MO. This example demonstrated the importance of the surface structure in modifying the catalytic selectivity of titania. Therefore, it is expected that, by controlling the exposed facets, we can design photocatalysts with both high reactivity and high selectivity. The photocatalysts that are terminated by specific facets allow the same adsorption states of reactant molecules and generate photoexcited electrons of similar energies on the specific facets. It is worth noting that these properties will be beneficial for the solar-induced selective photoconversion of carbon dioxides into specific valuable fuels because this process typically requires an undesired separation process and produces mixed hydrocarbons, including CH_4, CH_3OH, and $HCOOH$. It is believed that the breakthrough in making specific facets will intensify the development of selective organic transformations that are based on semiconductor photocatalysts.

High-index facets of nanomaterials usually have unique surface atomic structures, such as a high density of atomic steps, dangling bonds, kinks, and ledges, which can all act as active sites. Unfortunately, these unique surface atomic structures always have a high surface energy and high crystal growth rate, which is not naturally preferential growth and is easy to rapidly diminish during the crystal-growth process, so it is quite challenging to synthesize tailor−made crystals.

Yang and coworkers first reported the formation of anatase TiO_2 crystals that are exposed by high−index {105} facets [109]. They produced the product with well−faceted surface by a modified high−temperature gas−phase oxidation route with titanium tetrachloride ($TiCl_4$) as the Ti source. During the $TiCl_4$ oxidization process, the co−adsorption of oxygen, chlorine, or other related species will occur and may specifically lower the Gibbs free energy of the {105} facets thus the typical atomic configuration on the {105} facets can be stabilized and reserved. The unique stepped atomic configuration on the high−index {105} facets makes these materials promising candidates in the areas of renewable clean energy and environmental remediation.

Rutile is the thermodynamically stable phase of TiO_2 polymorphs, which can be obtained by typically three methods: (i) the hydrolysis of Ti precursors and subsequent crystallization; (ii)

the post–transformation from anatase/brookite phase via thermal treatment (phase transformation temperature required depends on the particle size of TiO_2) [110] and (iii) mechanical processing [111]. Although rutile is considered to be less active in photocatalytic reactions compared to anatase, nanostructured rutile has also been used photocatalysis applications and in some cases show even higher activity than anatase. Band gap of rutile TiO_2 is 0.2 eV smaller than anatase one and further results in a wider absorption range, which may be the advantage of this phase.

Afterwards, various morphologies of rutile have been developed [112-119], with the nanorod being is a common morphology. The synthesis routes of such rutile nanorods with a high aspect ratio have been well documented in the literature [114,119,120-129]. Generally speaking, the presence of Cl ions as mineralizer in the synthesis system is favourable for rutile TiO_2, regardless of the source of Cl. In the case of the specific synthesis routes of controlling morphology of rutile, there are two representative examples demonstrate the formation of faceted rutile crystals. One is the rapid formation of self-assembled microspheres with rutile nanorods by microwave heating of $TiCl_3$ at 200°C for only 1 min [115]. The nanorods are exposed with {110} and {111} facets, but because of the extremely rapid growth rate, the surface is not smooth. Interestingly, the synthetic rutile nanorods have a smaller bandgap of 2.8 eV compared with the conventional 3.0 eV, which may facilitate the photocatalysis ability under visible light irradiation. The other one is reported by Kakiuchi et al. [116], who observed the dependence of degree of perfection of facets on hydrothermal temperature, where $TiCl_3$ was also used as a precursor together with NaCl additive. For example, at low temperature (80°C), only needle–like nanorods without well–recognized facets were formed. However, when elevating the temperature to 200°C, well–developed lateral {110} and top {111} facets can be observed. Apparently, this result indicates that a higher temperature is favorable for growing crystals with well-developed facets.

Compared with anatase and rutile, brookite phase TiO_2 has attracted little interest due to the generally considered lack of photocatalytic activity. However, increasing literatures have shown that brookite is also photocatalytically active and even has unique photocatalytic properties in some cases [130-133]. However, among the synthetic brookites, crystal facets are usually non-recognizable. Interestingly, Buonsanti et al. [134] developed a nonhydrolytic synthesis route to successfully prepare high–quality anisotropically shaped brookite nanorods with a length of 30–200 nm. These rods are determined to be dominantly enclosed with the longitudinal {210}/{100} and basal {001} facet, which is in agreement with the equilibrium shape of brookite crystals predicted from the Wulff construction.

2.2. α-Fe_2O_3

Hematite (α-Fe_2O_3) is the most thermodynamically stable form of iron oxide under ambient conditions and it is also the most common form of crystalline iron oxide. The iron and oxygen atoms are naturally arranged in the corundum structure, which is trigonal–hexagonal scalenohedral (3 2/m) with space group R−3c, lattice parameters a = 5.0356 Å, c = 13.7489 Å, and six formula units per unit cell [135,136]. It is easy to understand hematite's structure based on the packing of the anions, O^{2-}, which are arranged in a hexagonal closed–packed lattice along the

[001] direction. The cations (Fe^{3+}) occupy the two−thirds of the octahedral interstices (regularly, with two filled followed by one vacant) in the (001) basal planes, and the tetrahedral sites remain unoccupied. The arrangement of cations can also be considered as producing pairs of FeO_6 octahedra that share edges with three neighboring octahedra in the same plane and one face with an octahedron in an adjacent plane in the [001] direction (Fig. 6). The face−sharing is responsible for a trigonal distortion of the octahedra as the proximal iron atoms are repelled to optimize the crystal's Madelung energy. As a result, hematite exhibits a C_{3v} symmetry and there are two different Fe−O bond lengths (Figure 6). However, the electronic structures of the distorted FeO_6 octahedral are thought to be similar to undistorted clusters [133,136]. Hematite is antiferromagnetic at temperatures below 260 K and is a weak (parasitic) ferromagnet at room temperatures. While the magnetic properties of hemitate are not particularly dependent on its photo electrochemical performance, the iron spin configuration does influence the optoelec‐ tronic and carrier transport properties of hematite. The absorption of photons by hematite starts from the near−infrared spectral region where weak absorption bands (with absorption coefficients, a, of the order 10^3 cm^{-1}) are due to transition states electrons between two d orbital energy levels of the Fe^{3+} ion, which are split by an intrinsic crystal field [136,138]. Analysis by means of a Tauc plot shows the indirect nature of the band gap for the $\alpha\text{-}Fe_2O_3$ involving d orbital to d orbital transition sand a direct transitions from O (2p) to Fe (3d), which occurs only for band gaps > 3.2 eV [139-141].
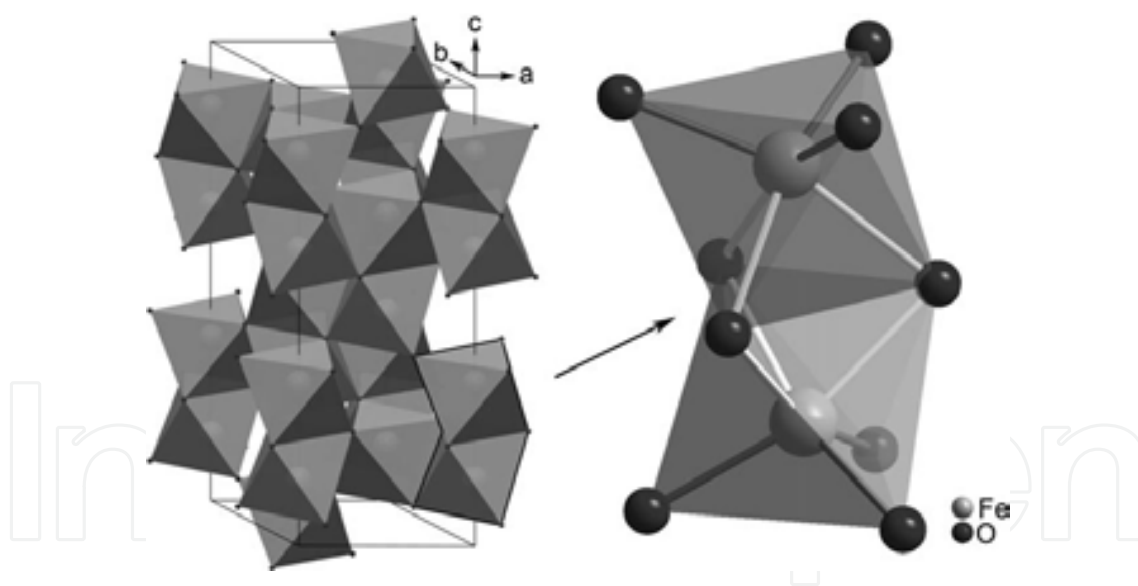

Figure 6. The unit cell (left) of hematite shows the octahedral face−sharing Fe_2O_9 dimers forming chains in the c direc‐ tion. A detailed view (right) of one Fe_2O_9 dimer shows how the electrostatic repulsion of the Fe^{3+} cations produce long (light grey) and short (dark grey) Fe−O bonds [136,137].

Hematite ($\alpha\text{-}Fe_2O_3$), an environmental friendly n-type semiconductor (*Eg* = 2.1 eV), has been widely used in many fields such as lithium−ion batteries [142], gas sensors [143–145], photo‐ catalysis [146,147], water treatment [148] and water splitting for generating H_2. Hematite is one promising candidate for photocatalytic applications due to its narrow band gap of about 2.0−2.2 eV. Further, hematite absorbs light up to 600 nm, collects up to 40% of the solar spectrum

energy, is stable in most aqueous solutions (pH > 3), and is one of the cheapest semiconductor materials available. Due to the band gap value α-Fe_2O_3 and the fact that it,s valence band edge is substantially lower than the water oxidation potential, it is a promising photoanode material for photoelectrochemical (PEC) water splitting. Photochemical water splitting involves a dispersed material in pure water and accordingly produces hydrogenand oxygen homogeneously throughout the solution [149]. The theoretical photocurrent density of α-Fe_2O_3 is ~12.6 mA/cm^2 under AM 1.5 G solar irradiation, and the solar energy conversion efficiency is ~15.5% in an ideal tandem PEC cell [150,151]. However, the photocatalytic performance of α-Fe_2O_3 is limited by certain factors such as high recombination rate of electrons and holes, low diffusion lengths of holes (2–4 nm), and poor conductivity, which led to both low efficiencies and a larger requisite over potential for photo-assisted water oxidation [152-156]. Many attempts have been made by researchers to overcome these anomalies of α-Fe_2O_3 such as lowering the recombination rate by forming nanostructures, enhancement in conductivity by doping with suitable metals and improving the charge transfer ability [157,158]. Apart from water-splitting applications, the photocatalytic activity of hematite can be used for the elimination of organic compounds in water treatment applications.

As the surface area plays an important role in determining the photocatalytic activity of materials, researchers have attempted to reduce the size of photocatalytic materials and enhance the photocatalytic properties of these materials by producing hematite in a nanoscale powder form. Many methods have been followed to synthesize α-Fe_2O_3 in a nanocrystalline form and in different shapes including hydrolysis [159], co-precipitation [160,161], hydrothermal methods [162-164], solvothermal methods [165,166], ionic liquid-assisted synthesis [167], thermal decomposition [168], combustion methods [169], and a combination reflex condensation and hydrothermal method [170].

Hosseinian et al. [171] synthesized nanostructured iron oxide of different morphologies and different phase compositions (α-Fe_2O_3 and Fe_3O_4) by a solid–state reaction (SSR) route. The photocatalytic activity was checked with respect to degradation of rhodamine B(RhB), and it was observed that the samples containing a mixture of α-Fe_2O_3 and Fe_3O_4 showed better photocatalytic activity than that of the pure α-Fe_2O_3. The higher photocatalytic activity observed for a mixed-phase sample was attributed to the higher transfer of electrons and holes generated during the photoreaction of α-Fe_2O_3 to the valence band of Fe_3O_4, which limits the recombination rates [172]. Yang et al. [173] synthesized α-Fe_2O_3 nanoparticles of uniform size (170nm to 2μm) by a hydrothermal route to study both magnetic as well as photocatalytic properties. The α-Fe_2O_3 powders with the smaller crystallite sizes show the highest photocatalytic degradation efficiency than that of the powders with larger crystallite sizes. Further, all the samples showed higher efficiency for degradation of the dye than that of the commercially available Degussa P25. Apte et al. [169] synthesized nano structured α-Fe_2O_3 powders in size ranging 25–55nm and their photocatalytic activity was analyzed with respect to the decomposition of hydrogen sulfide (H_2S) gas. α-Fe_2O_3 (necked structures) showed good photocatalytic properties and production of H_2. Zhou et al. [174] synthesized nanorods of α-Fe_2O_3 by thermal dehydration and compared the photocatalytic activity with microrods. The authors reported a higher degradation rate for rhodamine B(RhB) for nanodimensional α-Fe_2O_3 than

that of the corresponding micron-sized rods. Higher Fe–O bond stretching frequencies were proposed as one of the key factors behind the enhanced photocatalytic activity. Particle size, composition, porosity, and the local structures are also the key factors that affect the photocatalytic properties of materials. Townsend et al. [159] compared the photocatalytic activity of three forms of Fe_2O_3 including bulk (crystallite size 120 nm), ultrasonicated bulk (crystallite size 40 nm), and nanopowders of α-Fe_2O_3 (crystallite size 5.4 nm). They found that the rate of oxygen evolution is higher when the crystallite size becomes smaller, and the highest rate was reported for α-Fe_2O_3 nanopowders (1072 µmol/h g). In the case of α-Fe_2O_3 nanopowders, the hole diffusion length is comparable to the crystallite size, which results in more availability of holes to react with water. Dang et al. [160] reported the effects of calcination temperature, reaction temperature, amount of catalyst, and duration of reaction on the catalytic properties. They reported an increase in photocatalytic activity with increasing calcination temperature, reaction temperature, and catalytic amount up to a certain extent, after which the activity decreases. Similar effects were also reported by Pawar et al. [175] for α-Fe_2O_3 nanoparticles synthesized by a sol-gel technique followed by the heat treatment at different calcination temperatures. The efficiency of the catalyst was analyzed with respect to various experimental variables such as calcination temperature, pH, light intensity, and concentration of dye and catalyst. Samples calcined at 600°C show the highest photocatalytic activity because of the formation of the more dominant α-Fe_2O_3 phase. The photocatalytic properties were analyzed for the 3–10 pH range, and the reactions at higher pH conditions showed better photocatalytic properties. In basic pH conditions, formation of OH· radical is more favored and electrostatic abstractive effects between cationic malachite green dye and negatively charged surface of α-Fe_2O_3 increases, which results in a higher probability of dye degradation. Light intensity shows a linear effect on the photocatalytic properties of α-Fe_2O_3 due to the increased availability of photons for the reaction. Similar effects were also reported by Liu et al. [176] for α-Fe_2O_3 nanorods. These authors examined the effect of the amount of catalyst and initial dye concentration on the photocatalytic properties. The optimum catalyst amount was reported to be 50 mg/L to achieve the highest photocatalytic activity. However, the photocatalytic activity degrades with increasing dye concentration. This effect was justified in terms of a decrease in transparency with an increase in dye and catalyst concentration after a particular value.

In a photoreaction, the porosity of the catalyst plays a major role in enhancing the photocatalytic properties. Sundarmurthy et al. [177] synthesized 1D α-Fe_2O_3 nanobraids and nanoporous structures by electrospinning to analyze the photocatalytic properties. The nanostructures show superior photocatalytic activity for the degradation of Congo red dye (CR) in a small fraction of time due to the porous surface and nanosized crystallites of α-Fe_2O_3, which provide more active catalytic centers and allow effective interaction between organic dye and α-Fe_2O_3, thereby enhancing photocatalytic degradation performance. α-Fe_2O_3 porous structures were prepared by Zhang et al. [162] and the photocatalytic activity was analyzed by the degradation of methylene blue(MB). They analyzed the effect of porosity and the amount of catalyst on photocatalytic activity. It has been reported that an optimized amount of catalyst (20 mg) is required for getting the highest rate of degradation of MB, less or more than this amount leads to lower photocatalytic activity. Large amounts of catalyst result in lesser illumination, and when the amount of catalyst is insufficient, the active sites are not sufficient to degrade the

organic dye. Geng et al. [178] followed a number of Ni^{2+}/surfactant system routes for synthesizing α-Fe_2O_3 with a porous structure and rough surface which shows better photocatalytic properties than that of the α-Fe_2O_3 nanoparticles in the degradation of MB as a result of higher surface area. Gang et al. [147] prepared α-Fe_2O_3 micro/nano spheres synthesized by hydrothermal synthesis followed by the thermal treatment. The micro/nano spheres show a better dye degradation efficiency than that of the nanopowders. The calculated reaction rate for spherical structures is more than twice than that of the reaction rate of nanopowders and 12 times the reaction rate of the micron-sized powders. The better photocatalytic activityis the result of the higher specific surface area and porous structures.
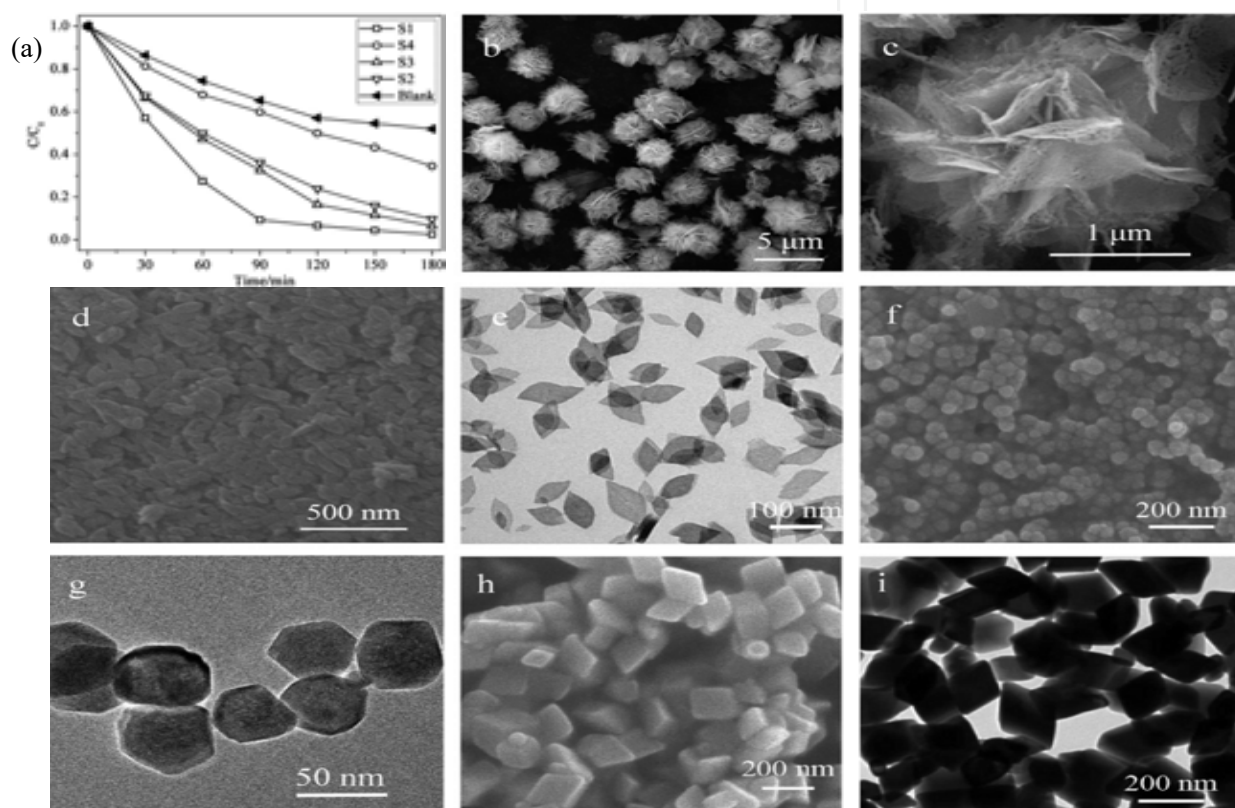

Figure 7. Photocatalytic degradation rate of RhB over the α-Fe_2O_3 nanostructures under visible light illumination in the presence of H_2O_2 additive (a),and SEM/TEM images of the α-Fe_2O_3 nanostructures: (b,c)S1;(d,e)S2;(f,g)S3;and(h,i)S4 [179].

Xu et al. [179], Zhou et al. [180] and Bharathi et al. [170] reported the effect of the surface morphology of α-Fe_2O_3 on its photocatalytic activity. α-Fe_2O_3 nanostructures with different morphologies such as microflowers, nanospindles, nanoparticles and nanorhombohedra were synthesized (Fig. 7) [179]. The photocatalytic activity was analyzed by monitoring the degradation of RhB in the presence of the catalyst. The best photocatalytic activity was observed for the samples with highest surface area and porosity. Similar surface area effects were also reported by Cheng et al. [181] for flower-like α-Fe_2O_3 nanostructures synthesized by a biphasic interfacial reaction route. The photocatalytic properties of α-Fe_2O_3 were evaluated by measuring the degradation of RhB. The results were compared with the commercial α-Fe_2O_3

powders and nanoflowers were found to have a better photocatalytic property than the commercial powders. The enhancement was related to the increase in crystallinity and increase in the surface area, which is also supported by results of other authors for TiO_2 [182] and Fe_2O_3 [183]. Similar surface area effects were also reported by Cao et al. [184], Xu et al. [166], and Li et al. [163] for α-Fe_2O_3 hollow microspheres prepared by solvothermal and hydrothermal methods. The photocatalytic activity was analyzed by the degradation of salicylic acid. The hollow spheres associated with nanosheets show better photocatalytic activity than that of then anoparticles of α-Fe_2O_3. Similar results were also reported by Majiet al. [168], where α-Fe_2O_3 powders prepared at 500°C show better photocatalytic activity for the degradation of rose Bengal dye than that of the powders prepared at 600°C and commercially available TiO_2(Degussa−25) as a result of higher surface area. α-Fe_2O_3 hollow spindles and spheres were prepared by Li et al. [164] and Xu et al. [167], respectively. These authors reported an enhancement in photocatalytic degradation efficiency as a result of the enhancement in specific surface area, which results in more unsaturated surface coordination sites exposed to the solution. The hollow microsphere facilitates more electron-hole transport and lowers the recombination rate. Hollow microspheres allow multiple reflections of visible light within the interior that encourage a more efficient use of the light source and enhance light−harvesting, leading to an increased quantity of ·OH available to participate in the photo-catalytic reaction. Along with this, the hollow spheres also provide ideal channels for the dye molecules and increase the probability of interaction.

Apart from crystallite size, the orientation of crystallites also plays a major role in enhancing the photocatalytic properties. This effect has been reported by Wu et al. [185], in which the authors prepared α-Fe_2O_3 nanocubes by a solvothermal method and reported a higher photocatalytic property for the {104} planes than that of the samples with {012} planes. The photocatalytic properties involve Fenton's reaction. The amount of Fe^{3+} on the surfaces of the catalyst play a very important role in the Fenton reaction in which the reduction of Fe^{3+} to Fe^{2+} generates hydroxyl radicals (·OH) [186]. It has been reported by Lv et al. [187] that {104} planes of α-Fe_2O_3 contain 10.3 atoms/nm^2 of exposed Fe^{3+} ions, whereas the {012} planes contain 7.33 atoms/nm^2 of exposed Fe^{3+} ions. This explains the higher reactivity of {104} planes than that of the {012} planes. Along with the surface morphology, oxygen pressure and amount of the catalyst also play a major role in enhancing the photocatalytic properties. Isaev et al. [188] reported an enhancement in the photocatalytic activity with an increase in the quantity of Fe_2O_3 up to a certain point, after that, the photocatalytic activity is decreased. Similarly, the authors reported an enhancement in dye degradation with increased oxygen content. The reason behind the enhancement in photocatalytic behavior is due to the formation of more oxygen-containing active species such as HO·, O_2·, and HO_2· oxidizing species. Zhou et al. [189] investigate visible−light−induced photodegradation of model dye rhodamine B (RhB) in the presence of hydrogen peroxide (H_2O_2) over hematite architectures, namely 1D nanorods, 2D nanoplates, and 3D nanocubes (Fig. 8), and the reactivity trend can be rationalized as exposed facets in the order {110} > {012} >> {001}. This photocatalytic activity order can be well explained by different facets of α-Fe_2O_3 surface atomic and electronic structures.
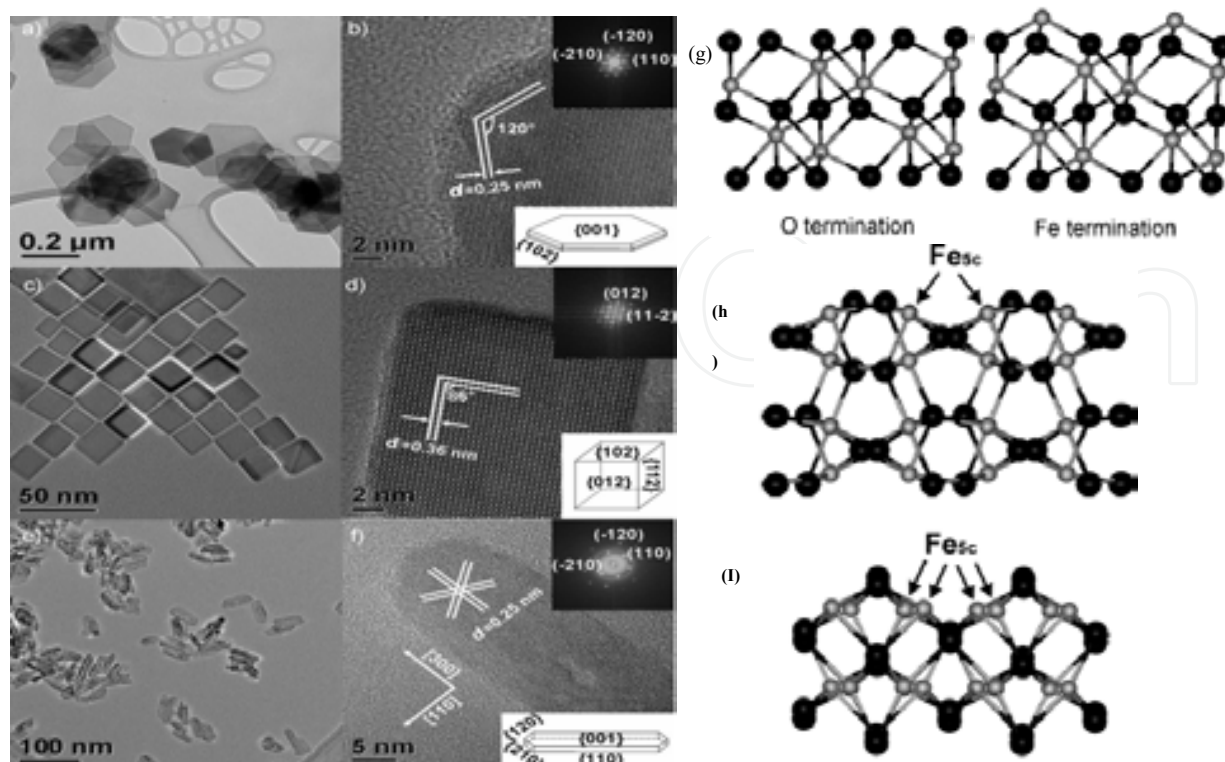
Figure 8. Representative morphologies and structures of α-Fe$_2$O$_3$ architectures.(a) TEM image and (b) HRTEM image of 2D α-Fe$_2$O$_3$ nanoplates. Insets: FFT pattern and drawing of a plate. (c) TEM image and (d) HRTEM image of 3D α-Fe$_2$O$_3$ nanocubes. Insets: FFT pattern and drawing of a cube. (e) TEM image and f) HRTEM image of 1D α-Fe$_2$O$_3$ nanorods. Insets: FFT pattern and drawing of a rod. Side views of surface terminations of α-Fe$_2$O$_3$. (g) {001}, (h) {012}, and (i) {110}. Large black spheres are oxygen and small gray spheres are iron. The coordinatively unsaturated iron atoms on the {012} and {110} surfaces are shown by arrows [189].

3. Ternary oxide system

3.1. BiVO$_4$

Bismuth vanadate (BiVO$_4$), which is an n−type semiconductor, has been identified as one of the most promising photocatalytic materials. As it is well known, BiVO$_4$ exists in three polymorphs of monoclinic scheelite, tetragonal scheelite, and tetragonal zircon structures, with bandgaps of 2.4, 2.34, and 2.9 eV, respectively. BiVO$_4$ exists naturally as the mineral pucherite with an orthorhombic crystal structure [190]. However, BiVO$_4$ prepared in the laboratory does not adopt the pucherite structure but crystallizes either in a scheelite or a zircon-type structure (Fig. 9) [191,192]. The scheelite structure can have a tetragonal crystal system (space group: $I4_1/a$ with $a = b = 5.1470$ Å, $c = 11.7216$ Å) or a monoclinic crystal system (space group: $I2/b$ with $a = 5.1935$ Å, $b = 5.0898$ Å, $c = 11.6972$ Å, and $b = 90.3871$) [192,193] while the zircon-type structure has a tetragonal crystal system (space group: I_41/a with $a = b = 7.303$ Å and $c = 6.584$ Å) [192,194].
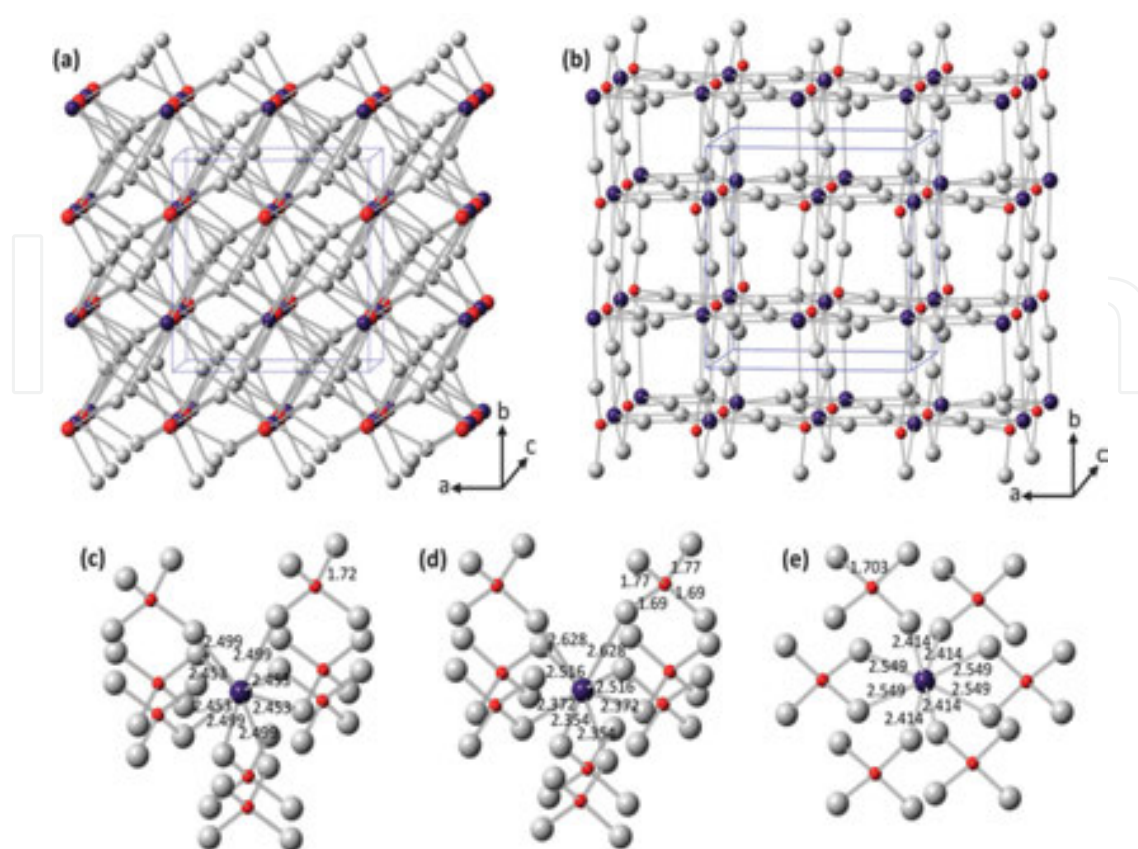
Figure 9. Crystal structures of (a) tetragonal scheelite and (b) zircon−type $BiVO_4$ (red: V, purple: Bi, and gray: O). The crystal structure of monoclinic scheelite is very similar to what is shown in (a) with the exception being the subtle changes in atomic positions of Bi, V, and O. Local coordination of V and Bi ions in (c) tetragonal scheelite, (d) monoclinic scheelite, (e) and zircon−type $BiVO_4$ structure with bond lengths shown in Å [192,194].

In the scheelite structure, four O atoms coordinate each V ion within a tetrahedral site and eight O atoms from eight different VO_4 tetrahedral units coordinate each Bi ion [192,193]. Fig. 9(a) shows the four−coordinated V center and the eight−coordinated Bi center alternating along the [001] direction. Two Bi centers and one V center coordinate each O atom in this structure, and a three−dimensional structure was formed by holding the Bi and V centers. The only difference between the tetragonal and monoclinic scheelite structure is that the local environments of V and Bi ions are more significantly distorted in the monoclinic structure, which removes the fourfold symmetry necessary for a tetragonal system. For example, in the tetragonal scheelite, all four V−O bond lengths were equal (1.72 Å), while in a monoclinic scheelite structure, there are two different V−O bond lengths(1.77 Å and 1.69 Å). In the same manner, in the tetragonal scheelite structure, only two very similar Bi−O distances exist (2.453 Å and 2.499 Å), while in the monoclinic scheelite structure, the Bi−O distances change significantly (2.354 Å, 2.372 Å, 2.516 Å and 2.628 Å) [192,193]. The significant distortion of the Bi−polyhedra indicates that the Bi 6s alone is more sterically expressed in the monoclinic scheelite structure.

It should be noted that the monoclinic scheelite structure of $BiVO_4$ was originally reported with the space group *I*2/b, which is a nonstandard space group [192,193]. Some recent studies

of BiVO$_4$ have used a standard space group $C2/c$, which is converted from $I2/b$. Changes in the crystallographic axes via the conversion of a monoclinic I−centered (body-centered) cell to a monoclinic C-centered cell are shown in Fig. 10 [195]. With this cell conversion, the new cell parameters for $C2/c$ are a' = 7.2472 Å, b' = 11.6972 Å, c' = 5.0898 Å, and β' = 134.225°. The choice of the I−centered monoclinic cell has the advantage of easily showing its structural relationship to the tetragonal scheelite structure that was reported in a body−centered space group, $I4_1/a$, using the identical unit cell choice and crystallographic axes. Since both $I2/b$ and $C2/c$ space groups, which have different unit cell choices and crystallographic axes, are commonly used to describe the monoclinic scheelite structure of BiVO$_4$, it is necessary to clarify the space group used when referring to specific atomic planes or crystal directions as well as the hkl indices of X-ray diffraction peaks in order to prevent any possible confusion [192].
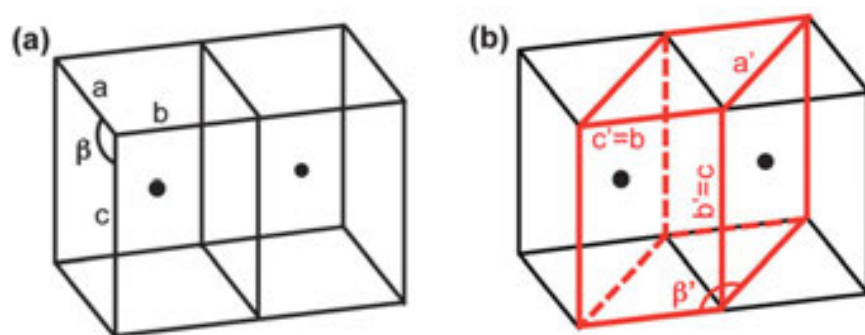

Figure 10. Cell conversion of (a) I−centered monoclinic to (b) C−centered monoclinic. a, b, c, and β represent the unit cell parameters for the I−centered cell and a, b0, c0, and b0 for the C−centered cell [195].

In the zircon−type structure, V is still stabilized by four O atoms and Bi is coordinated by eight O atoms. However, since two VO$_4$ units provide two O atoms to Bi, each Bi is surrounded by only six VO$_4$ units, as shown in Fig. 9 (e). To form a 3D structure, two Bi centers and one V center are connected by all oxygen atoms, which holds the V and Bi centers together [192].

It was reported that the low temperature synthesis (e.g., precipitation at room temperature) can form a zircon−type structure [192,196,197]. However, in this process, kinetics plays a critical role in the determination of final products, so the structure type obtained at low temperatures may change with different synthesis methods used and detailed conditions. A phase transition from tetragonal zircon to monoclinic scheelite was reported to occur irreversibly at 670−770 K [192,196]. Among scheelite structures, the tetragonal phase is a high temperature phase and the phase transition between monoclinic scheelite BiVO$_4$ and tetragonal scheelite BiVO$_4$ was observed to occur reversibly at 528 K [192,196].

In the zircon−type BiVO$_4$, the charge-transfer transition from O 2p orbitals to empty V 3d is mainly responsible for the bandgap transition. In the scheelite structure, the bandgap is reduced because the 6s state of Bi^{3+} appears above the O 2p and the transition from Bi 6s^2 (or hybrid Bi 6s^2−O 2p orbitals) to the V 3d becomes possible. Among scheelite BiVO$_4$ structures, Tokunaga et al. reported that monoclinic scheelite structure shows much higher photocatalysis activity for the photocatalytic water oxidation compared with tetragonal scheelite structure

[192,198]. The bandgap energies of the tetragonal and monoclinic scheelite $BiVO_4$ shows little difference and the more severe distortion of the metal polyhedra present in the monoclinic scheelite $BiVO_4$is the reason why the photocatalytic performance is different [192,198]. As discussed earlier, the local environment of Bi in the monoclinic scheelite structure is much more distorted than that in the tetragonal scheelite structure (Fig. 9 (c) and (d)).
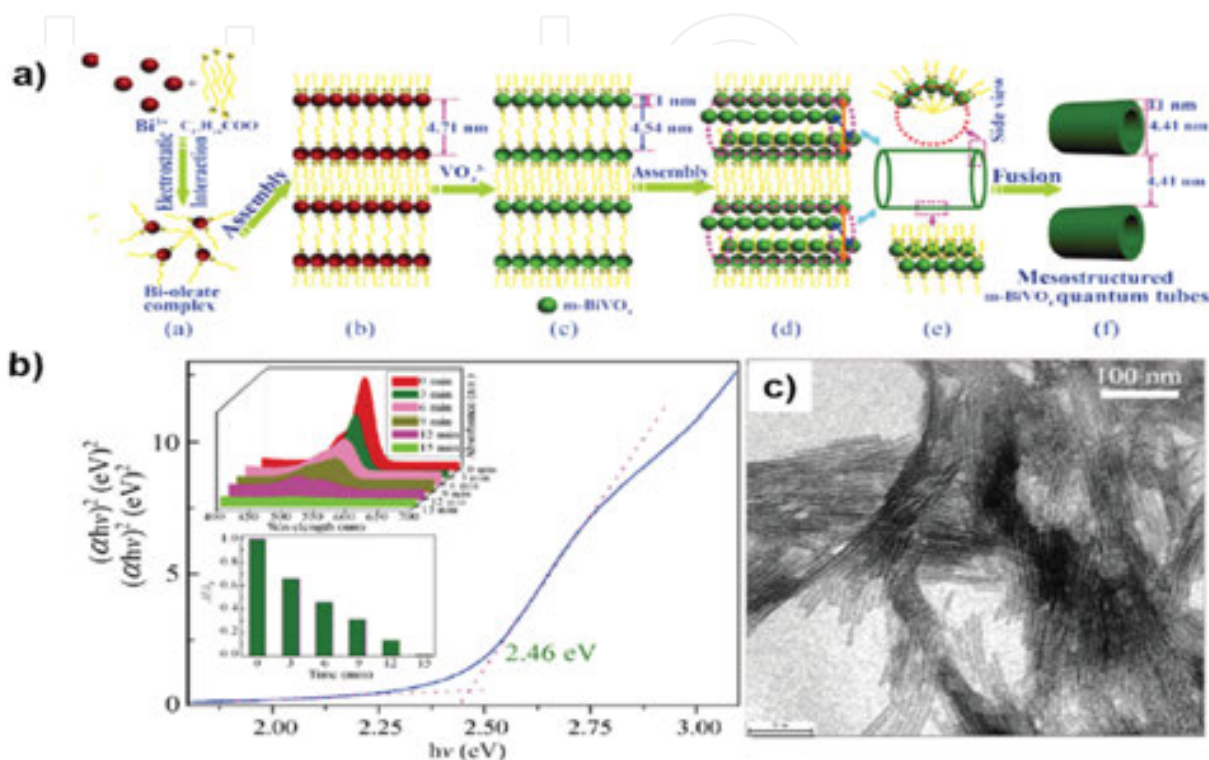

Figure 11. (a) Mechanism for the formation of $BiVO_4$ quantum tubes. (b) Optical absorption edge of $BiVO_4$ quantum tubes (top and bottom insets:photodegradation of RhB vs. irradiation time under visible light). (c) TEM image of $BiVO_4$ quantum tubes after the photodegradation [205]

Morphology control is an efficient method to facilitate carrier transportation and light harvesting, accelerate charge movement within the material structure and assist the collection and separation of electron-hole pairs at the interface of the materials [199-202]. Controllable synthesis of $BiVO_4$ with controlled morphologies has been notable developed (such as nanorods, nanowires, nanotubes (NTs), nanobelts, nanoellipsoids, hollow spheres, and even some hierarchical architectures) and corresponding morphology-dependent photocatalytic properties have also been extensively studied [203-211]. For example, Tada et al. first fabricated $BiVO_4$ nanorods (NRs) using polyethylene glycol (PEG) as a shape−directing agent [203]. Yu et al. developed a template−free solvothermal method to synthesize $BiVO_4$ nanotubes (NTs) [203]. Xie et al. reported a novel assembly−fusion strategy for the synthesis of $BiVO_4$ quantum tubes with an ultra-narrow diameter of 5 nm, ultrathin wall thickness down to 1 nm, and exposed {010} facets (Fig. 11 (a), (c)) [206]. As the increase of the reaction time, optical absorption edge and band energy of the $BiVO_4$ quantum tubes are significantly blue−shifted compared with bulk $BiVO_4$, which is due to the well-known quantum size confinement effect (Fig. 11 (b)).

Nanosized building blocks, such as nanowires, nanobelts, nanosheets, and nanotubes possess interesting properties, and the self-assembling of them into hierarchical architectures is much more interesting and has attracted great attention [199]. Liu et al. and Chen et al. synthesized $BiVO_4$ porous hollow microspheres composed of single−crystalline nanosheets using a solvothermal−induced self-assembling method (Fig. 12 (a), (b)) [207,209]. These hollow microspheres exhibited excellent photocatalytic activity due to the increased specific surface area and light harvesting ability. Xie et al. also reported the multi-responsive function of ellipsoidal $BiVO_4$ assembled from many small nanoparticles with major exposed {101} facets [210]. Similarly, Zhao et al. synthesized uniform hyperbranched $BiVO_4$ via a surfactant−free hydrothermal route (Fig. 12 (c)) [211]. The crystal consists of four trunks with branches distributed on opposite sides, this unique structure is beneficial from the different growth rates along a, b, and c axes: preferentially along the [100] direction at the beginning and subsequently along the [010] and [001] directions. The loosely packed building units of the hyperbranched structure exhibits excellent photocatalytic activity, because (i) the small crystal size allows the inside generated electron-hole pairs efficiently transporting from inside out to the surface and (ii) the large surface area provides abundant active sites for the photocatalytic reaction and promotes light harvesting as well as reactant adsorption.

One of the main reasons for the charge recombination in $BiVO_4$ is the long diffusion length of the photo−induced electrons [212-214]. Tailoring porous $BiVO_4$, especially ordered porous structures, can shorten the diffusion length and thus facilitate charge migration, providing a readily accessible channel and increasing the adsorption of reactants and the supply of more surface active sites [214,210]. Yu et al. reported that ordered mesoporous $BiVO_4$ shows a higher photoactivity than conventional $BiVO_4$, and this mesoporous $BiVO_4$ was fabricated by nanocasting using mesoporous silica KIT−6 as the replica parent template (Fig. 13 (a)) [210]. Ordered macroporous $BiVO_4$ with controllable dual porosity was synthesized by Xie et al. for efficient solar water splitting and the relationship between the geometrical characteristics and the charge migration was also demonstrated (Fig. 13 (b)) [215]. There are mainly two factors that determined by the geometrical characteristics of periodically ordered macroporous structures (Fig. 13 (b), (i)): the diameter of the macropores surrounded by the final skeletal walls (denoted as D1) and the diameter of the pores between neighboring macropores (denoted as D2). Previously, Lee et al. observed an efficient photo-induced charge drift mobility within the proper D1 size [216]. Based on this, Xie et al. further synthesized ordered macroporous $BiVO_4$ architectures with controllable dual porosity (aforementioned as D1 and D2) via a modified colloidal crystal templating method (Fig. 13 (b), (i) and (ii)), and verified that charge migration in periodically ordered macroporous architectures has a strong dependence on D1 and D2 (Fig. 13 (b), (iii)) [215]. On the one hand, no matter in the bulk and on the surface, it is believed that a smaller D2 is favorable for charge migration. On the other hand, a smaller D1 blocks bulk charge migration but facilitates surface charge migration.

The specific crystal facet determines the surface active sites and even the electronic structure, as a result crystal facets play a critical role in photocatalysis. [198,217], and consequently, it is of great importance to develop the crystals exposed with highly reactive facets [217-223]. Xi et al. synthesized well-defined $BiVO_4$ nanosheets exposed with {001} facets using a straightfor-
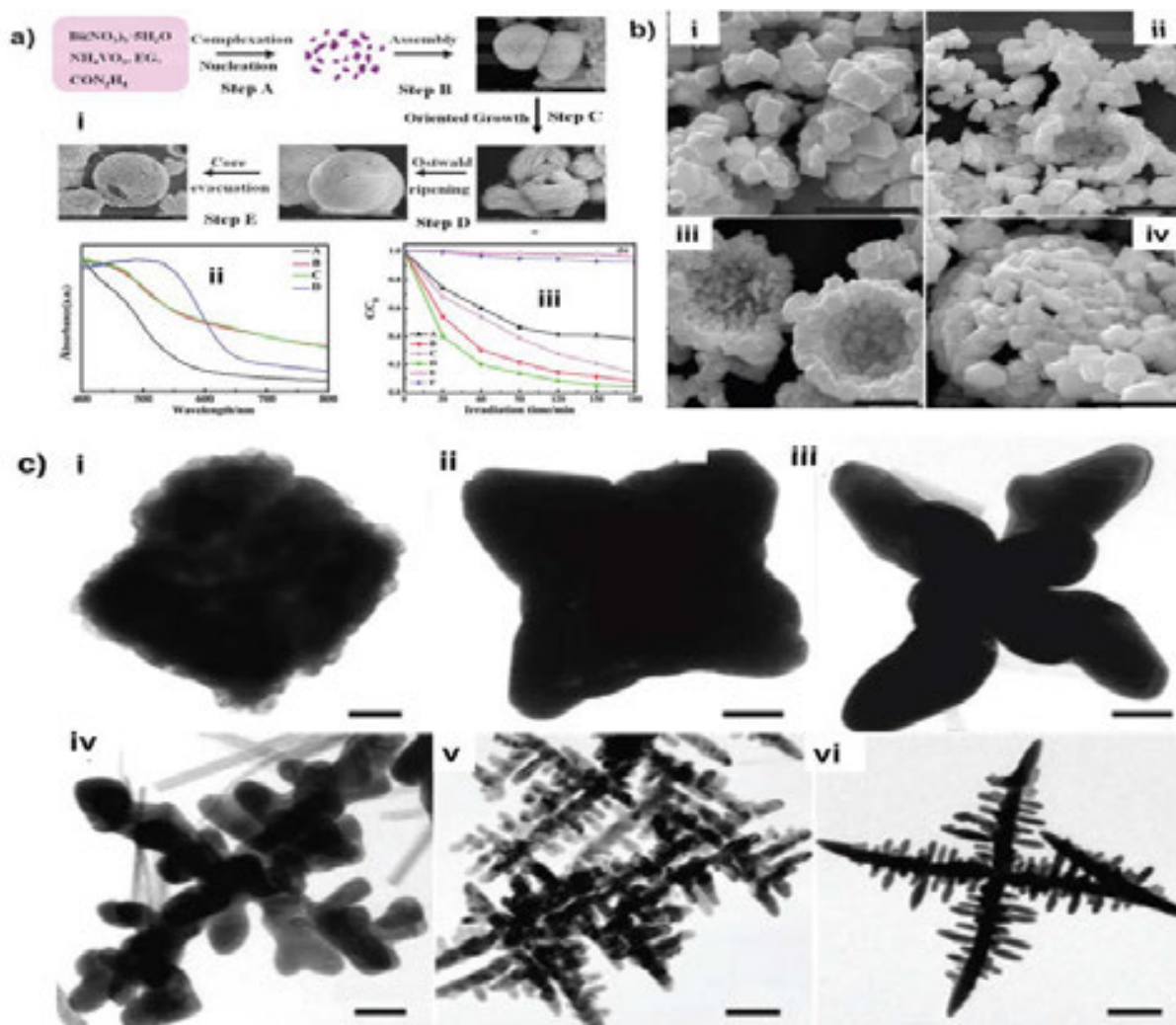
Figure 12. (a) Formation mechanism, UV−Vis absorption, and RhB photodegradation of hollow BiVO$_4$ microspheres [207]. (b) Morphology evolution of BiVO$_4$ hollow spheres via a hydrothermal method using urea as the guiding surfactant (I: 2 h; II: 4 h; III: 8 h; IV: 12 h; V: 24 h; scale bar is 2 μm) [208]. (c) Morphology evolution of hyperbranched BiVO$_4$ at intervals of 10 min (I), 20 min (II), 30 min (III), 45 min (IV), 1 h (V), and 3 h (VI), respectively (the scale bars are 100, 200, 200, 200, 400 and 500 nm, respectively) [210].

ward hydrothermal route without any template or organic surfactant (Fig. 15 (a)) [218]. Typically, BiVO$_4$ crystals show a regular decahedron shape with controllable exposed facets of {010}, {011}, {110} and {111}, as shown in Fig. 14. Li et al. Synthesized BiVO$_4$ with a highly exposed (010) facet using TiCl$_3$ as a directing agent, and correlated this to the high activity in O$_2$ evolution on BiVO$_4$ (Fig. 15 (b)) [219]. Inspired by this work, facet-dependent photocatalytic activity for water oxidization on BiVO$_4$ was investigated by density functional theory (DFT) calculations, particularly between the (010) and (011) facets (Fig. 14 (c)) [220]. The (010) facet has a higher activity compared with the (011) facet due to its higher charge carriers mobility, easier adsorption of water, and lower overall potential energy of O$_2$ evolution.

Recently, many studies have reported that photo−induced electrons and holes may be drifted to different crystal facets [217,221-223], which means photo-reduction and oxidation may
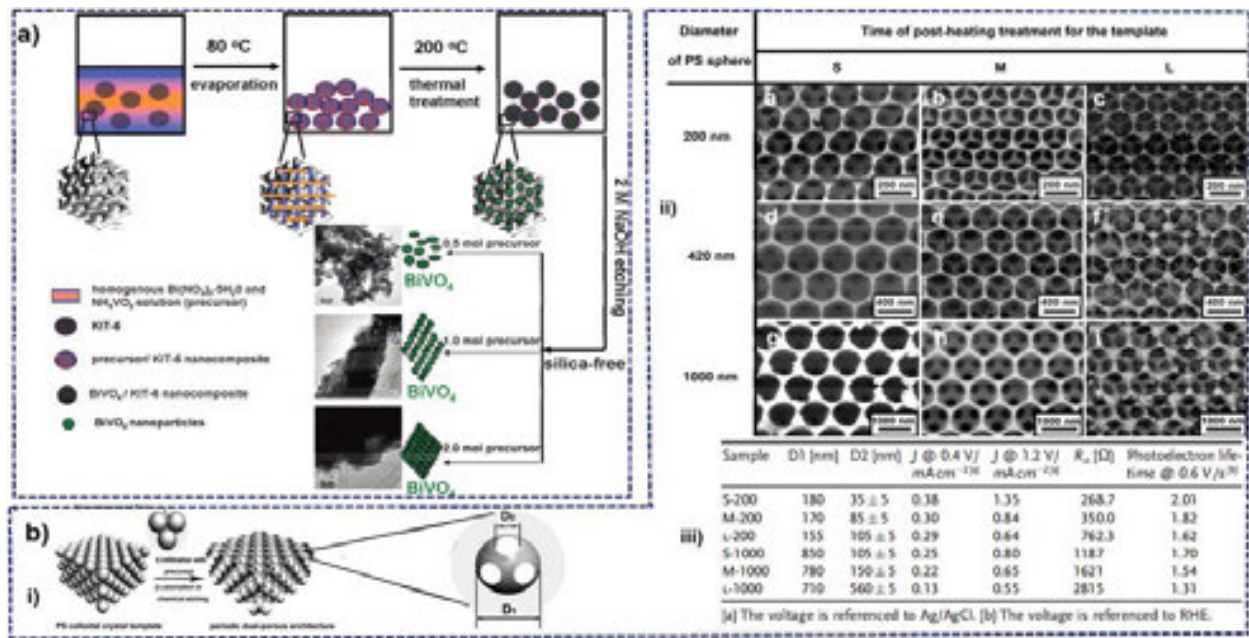
Figure 13. (a) Proposed process for the fabrication of ordered mesoporous BiVO$_4$ [211]. (b) (i)Schematic representation of dual porosity in periodically ordered porous BiVO$_4$; (ii) typical SEM images of corresponding BiVO$_4$; (iii) relationship between PEC performance and dual porosity [216].
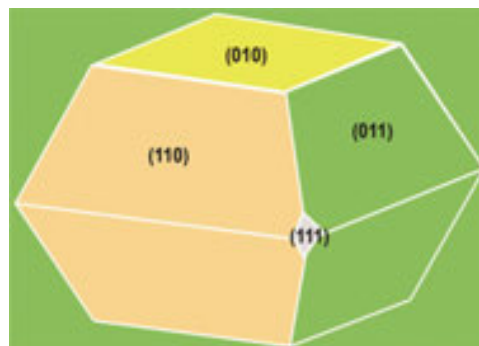

Figure 14. Typical crystal of BiVO$_4$ exposed with the {010}, {011}, {110} and {111} facets.

happen preferentially on different facets. Therefore, the cooperation of different facets is very important to obtain high quantum efficiency. Using photochemical labeling, Li et al. discovered that photo-excited electrons-driven reduction reaction (Pt–photodeposition) and photo-excited holes-driven oxidation reaction (MnO$_x$-photodeposition) take place on the {010} and {110} facets, respectively (Fig 16a) [222], which implies that the photo-induced electrons and holes move to the {010} and {110} facets, respectively. Notably, it provides a very useful inspiration to selectively deposited co-catalyst on specific facets via photodeposition (Fig. 16 (b)) [223]. Using this concept, the photocatalyst with Pt on the {010} facets and MnO$_x$ on the {110} facets exhibits a much higher activity in both photocatalytic and PEC water oxidation, compared with the counterparts with randomly distributed Pt and PbO$_2$ co–catalysts (Fig. 16 (c), (d)). The coupling of co–catalysts on selected semiconductor facets may open up a new strategy for developing highly efficient photocatalysts.
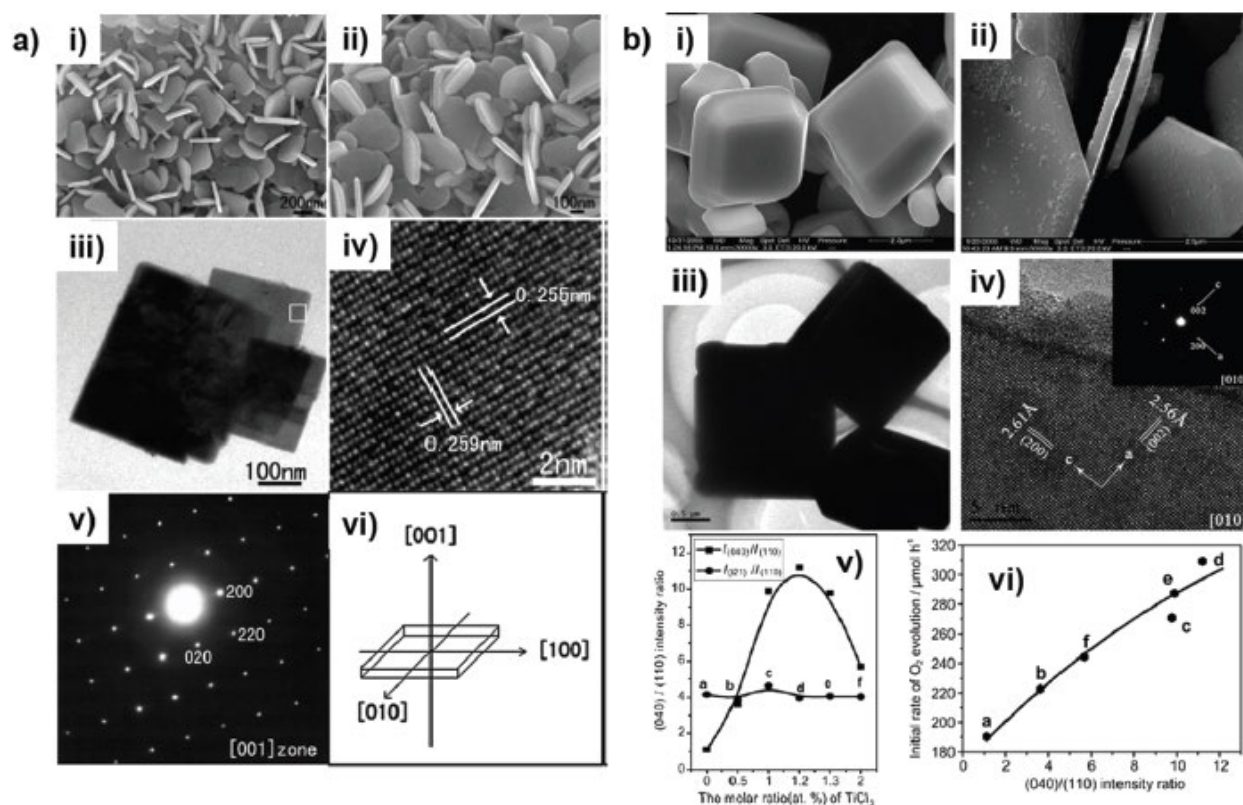
Figure 15. (a) SEM and HRTEM images of BiVO$_4$ nanoplates exposed with the {001} facets [213]. (b) Facet(010/110)-dependent photoactivity of oxygen evolution on BiVO$_4$ [214].

3.2. Bi$_2$WO$_6$

The Aurivillius family have a general formula of Bi$_2$A$_{n-1}$B$_n$O$_{3n+3}$ (A = Ca, Sr, Ba, Pb, Bi, Na, K and B = Ti, Nb, Ta, Mo, W, Fe), and Bi$_2$WO$_6$ is the simplest member of this family (where n = 1) and usually have the layer structures and unique properties [224]. Fig. 17 shows a schematic structure of the Bi$_2$WO$_6$ crystalline with orthorhombic structures constructed by alternating (Bi$_2$O$_2$)$_n^{2n+}$ layers and perovskite−like(WO$_4$)$_n^{2n-}$ layers [225]. More recently, many Aurivillius-based compounds have been reported which exhibit interesting properties suitable for photocatalytic applications. Of these, Bi$_2$WO$_6$ is the simplest and probably the most studied example within this family. In this bismuth tungstate, the perovskite−like structure is defined by WO$_6$ units which form a layer perpendicular to the (100) direction and sandwiched between the (Bi$_2$O$_2$)$^{2+}$ units. Layers sandwiched structure favors the efficient separation of photogener-ated electron-hole pairs and then improves the photocatalytic activity, which can be ascribed to the formed internal electric fields between the slabs [226,227]. Due to its preferable band composition and unique layered structure, Bi$_2$WO$_6$ possesses several advantages as photoca-talysts over the competing materials, especially in the view of practical applications, including its desirable visible− light absorption, relatively high photocatalytic activity and good stability.

Bi$_2$WO$_6$ consists of accumulated layers of corner-sharing WO$_6$ octahedral sheets and bismuth oxide sheets [228,229]. The conduction band of Bi$_2$WO$_6$ is composed of the W5d orbital; its valence band is formed by the hybridization of the O2p and Bi6s orbitals, which not only makes
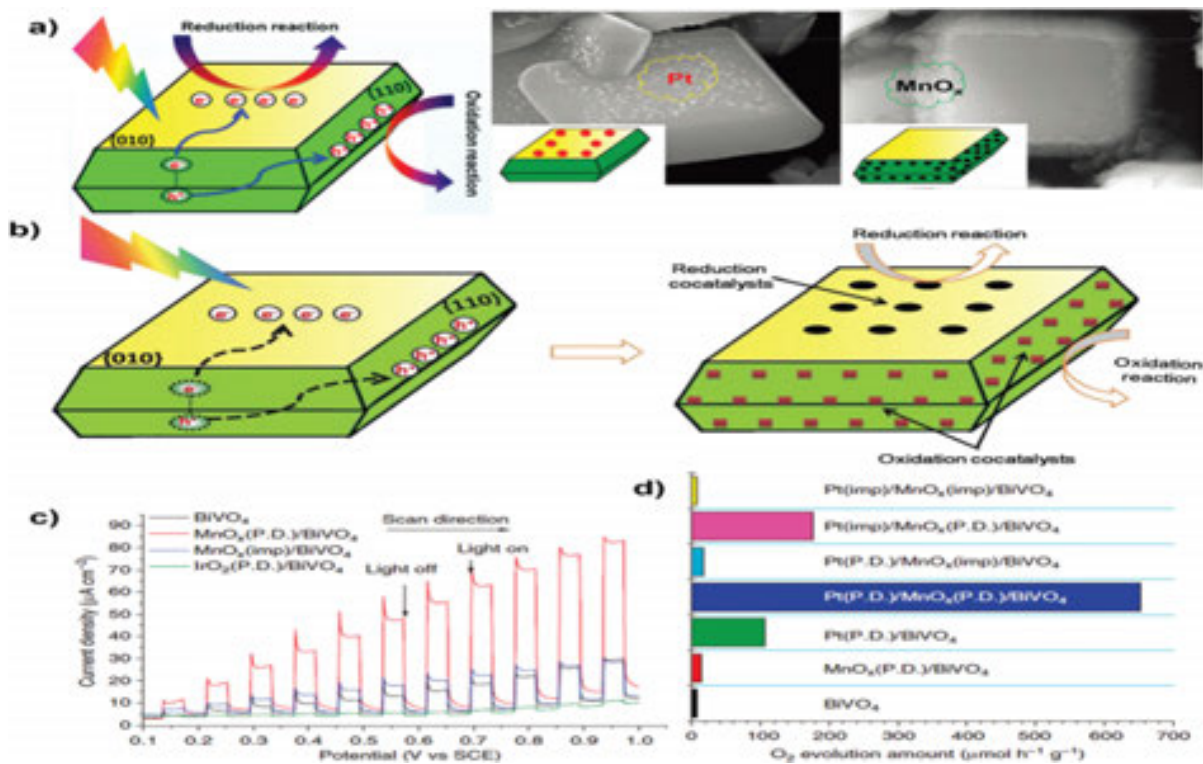
Figure 16. (a) Charge separation between the {010} and {110} facets confirmed by Pt and PbO$_2$ photodeposition on Bi-VO$_4$ [218]. (b) Selective deposition of dual redox co-catalysts on specific facets of BiVO$_4$ [219]. (c, d) Photoelectrocatalytic and photocatalytic water oxidation activity of BiVO$_4$ with selectively deposited co-catalysts on specific facets and randomly distributed co-catalysts [220].

the VB largely dispersed and thus results in a narrowed band gap of Bi$_2$WO$_6$ (2.8 eV) capable of absorbing visible light ($\lambda > 400$ nm), but also favors the mobility of photogenerated holes for specific oxidation reactions [230]. Such a band structure indicates that charge transfer in Bi$_2$WO$_6$ upon photoexcitation occurs from the O2p + Bi6s hybrid orbitals to the empty W5d orbitals, as illustrated in Fig. 18 [231].

As early as in 1999, the solid−state method was first used by Kudo et al. to synthesize Bi$_2$WO$_6$ photocatalyst [232], but the particle sizes of the product are in micrometers and the specific surface area is very small, which greatly limit its application in the photocatalysis. In the aim of obtaining micro or nanosized Bi$_2$WO$_6$ structures with enhanced photocatalytic activity, several groups have developed many advanced synthetic methods including sol−gel method [233], combustion synthesis method [234], ultrasonic method [235], co-precipitation method [236], sol-gel method/calcining method [237], and hydro/solvothermal method [238-245].

Bi$_2$WO$_6$ micro/nano−structures with diverse shapes exhibit different photocatalytic activities, and currently some of them have been used not only for the photodegradation of other organic pollutants but also for the photocatalytic disinfection. In 2005, Zhu's group have developed a Bi$_2$WO$_6$ nanoplates [246,247] applied in the photodegradation of rhodamine B (RhB) under visible−light irradiation. Notably, the photocatalytic reaction constant (k) of the best quality Bi$_2$WO$_6$ nanoplates is three times higher than that of the sample prepared by solid−state reaction [246]. In addition, they found a significantly pH-dependence of the photo-assisted
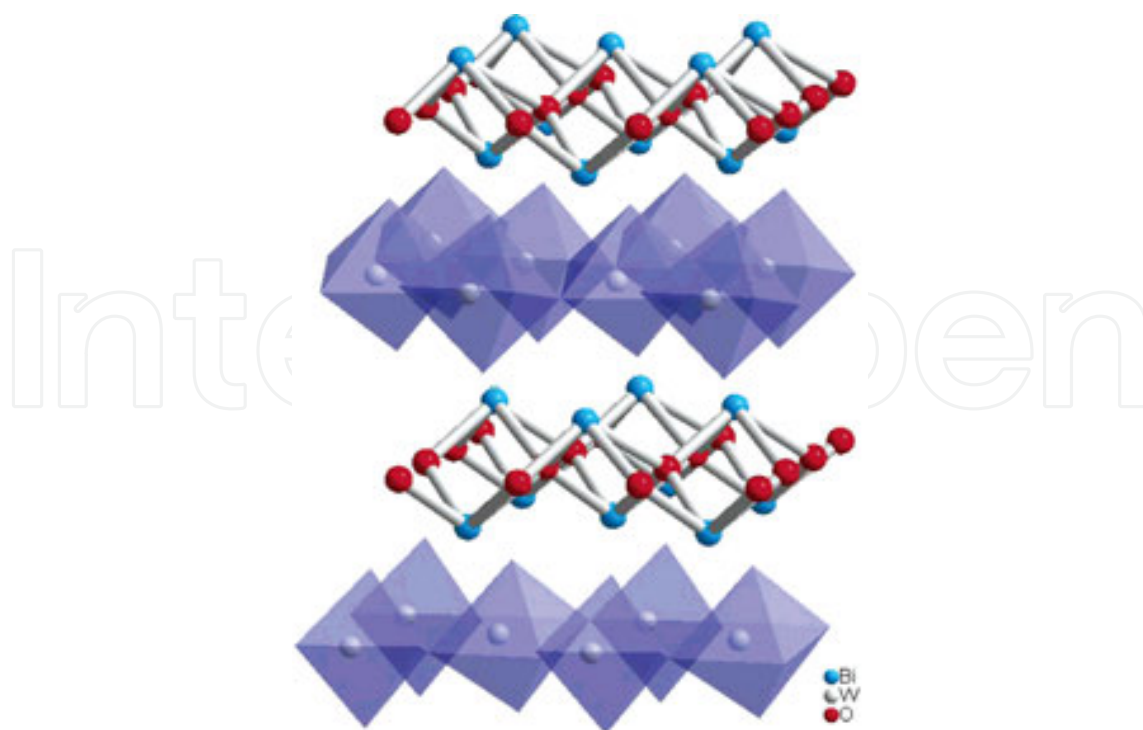
Figure 17. Structure of Bi_2WO_6 showing the WO_4^{2-} and $Bi_2O_2^{2+}$ layers [225].
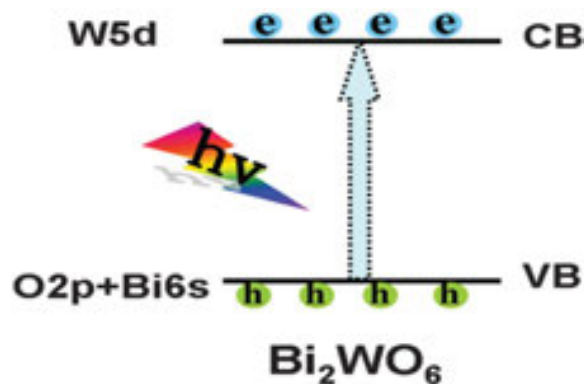

Figure 18. Band structure of the Bi_2WO_6 photocatalyst. [231]

degradation of RhB in aqueous Bi_2WO_6 as the pH varies from 5.03 to 9.89, where the highest degradation rate was achieved at pH 6.53. It is proposed that the pH of the solutions can affect the mode and extent of adsorption of RhB on the Bi_2WO_6 surface and further the transformation rate of RhB indirectly. They further used the total organic carbon measurement to determine the high mineralized degree of RhB [247]. Further studies on the mechanism shows that a photocatalytic process and a photosensitized process is involved in the the Bi_2WO_6–assisted photodegradation of RhB [247]. However, the contribution of RhB photodegradation driven by the light–excited RhB was much slower than by the light–excited Bi_2WO_6. The experimental results show that only 19% of RhB was degraded by photosensitized action, while 81% of RhB was degraded by a photocatalytic process [247].

In order to further improve the photocatalytic activity of Bi_2WO_6, some groups have developed Bi_2WO_6 nanoplates superstructures [248,249-253]. Zhang group also prepared Bi_2WO_6 micro/nanostructures, including nanoplates, tyre/helixlike, disintegrated−flower−like and flower −like superstructures [238,239]. The photodegradation results of RhB show that these Bi_2WO_6 micro/nanostructures exhibit different photocatalytic activities under visible-light ($\lambda > 400$ nm) irradiation, as shown in Fig. 19 (a). Among these photocatalysts, the uncalcined flower-like Bi_2WO_6 superstructure prepared with pH = 1 processes an improved photocatalytic perform-ance, which can degrade 84% of RhB in 60 min [238]. Besides, the photocatalytic performance can be further improved by the calcination process, and the result calcined flower−like Bi_2WO_6 superstructure has a higher photocatalytic activity, which can degrade 97% of RhB in 60 min (Fig. 19 (b)). This performance is also superior to other traditional photocatalysts such as TiO_2 (P25) and bulk SSR-Bi_2WO_6 powder prepared by solid−state reaction [239].
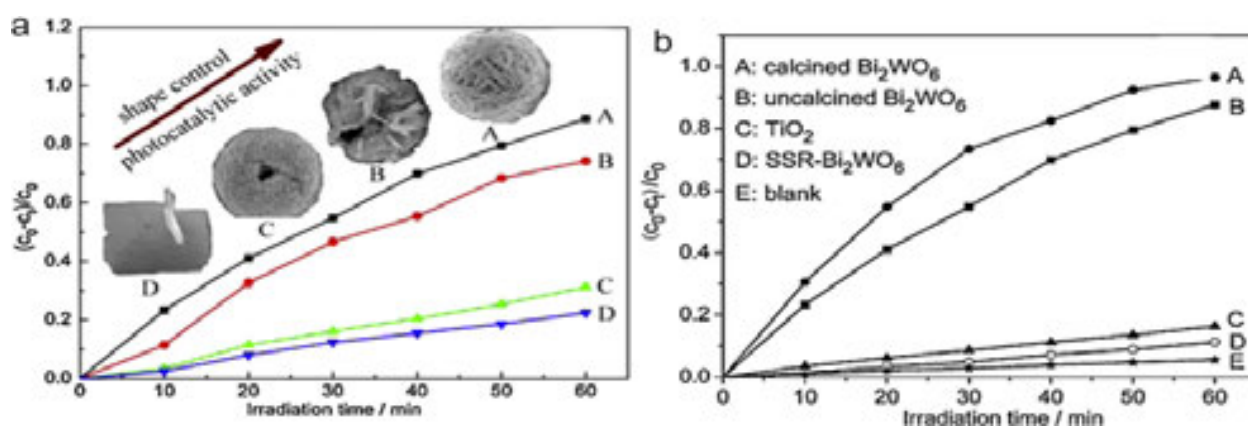

Figure 19. (a) The photodegradation efficiencies of RhB as a function of irradiation time by different Bi_2WO_6 nano/micro−structures: (A) the uncalcined flower−like Bi_2WO_6 superstructure prepared with pH = 1, (B) the uncalcined dis-integrated flower-like Bi_2WO_6 superstructure prepared with pH = 2.5, (C) the calcined tyre/helix−like Bi_2WO_6 super-structures prepared with pH = 1 and P123, (D) the uncalcined Bi_2WO_6 nanoplates prepared with pH = 7.5; [239] (b) the photodegradation efficiencies of RhB as a function of irradiation time by photocatalyst samples: (A) the calcined flow-er-like Bi_2WO_6 superstructure, (B) the uncalcined flower-like Bi_2WO_6 superstructure, (C) TiO_2 (P25), (D)bulk SSR-Bi_2WO_6 powder, and (E) blank [238].

The novel flower-like superstructures of the uncalcined or calcined Bi_2WO_6 is mainly respon-sible for the highly improved photocatalytic activity. At the same time, as shown in SEM images (Fig. 20), there are plenty of meso− or macro−diameter sized pores in the flower-like superstructures, which can be considered as electron transport paths that also contributes to the photocatalysis process. [254]. It is generally believed that it is an integral part of the architectural design if the reactant molecules can easily move in or out of the nanostructured materials, the efficiency of the photocatalysis can be improved, and here, meso− or macro −diameter sized pores provides the important transport paths [254,255]. They also believe that the introduction of textural transport paths in the uncalcined or calcined Bi_2WO_6 superstruc-tures facilitate the reactant molecules to easily incorporate with the reactive sites on the framework walls of photocatalysts, which leads to excellent photocatalytic performance for the degradation of RhB [239]. On the other hand, fewer defects, which acting as electron-hole

recombination centers, can be significantly reduced by improved crystallinity of Bi_2WO_6 through the calcination process of Bi_2WO_6 [238]. This has been proved by Amano et al. [256] who experimentally investigated the influence of crystallization on the lifetime of photoexcited electrons from Bi_2WO_6. The recombination rate of electrons decay with holes can be characterized by the intensity of transient IR absorption after a 355 nm laser pulse [256]. If an appreciable absorbance at 100 μs in Bi_2WO_6 crystalline can be observed, it means a slow recombination rate and a long lifetime of photogenerated carriers, which is beneficial for driving appreciable photocatalytic reactions. However, no transient absorption for amorphous Bi_2WO_6 samples was observed implying a fast recombination of electron-hole pairs, leading to negligible photocatalytic activity. Therefore, the higher photocatalytic activity of the calcined Bi_2WO_6 is explicable in several cases [238,251,256].
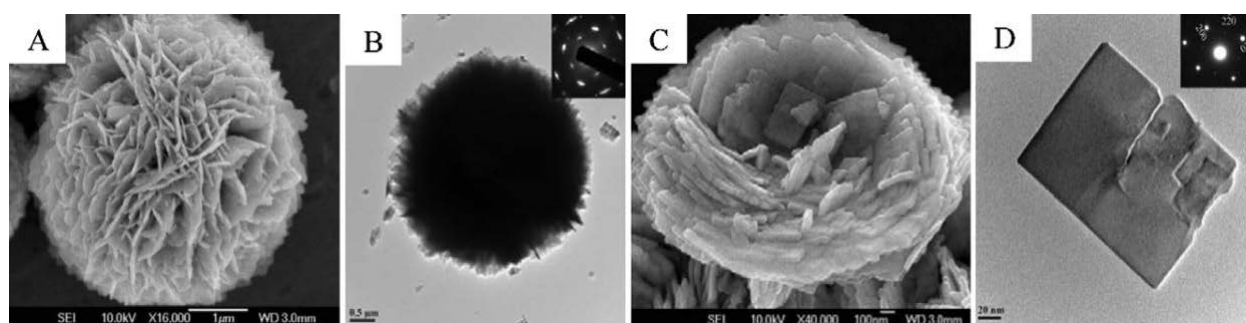

Figure 20. SEM (A) and TEM (B) images of an individual flower–like Bi_2WO_6 superstructure (inset: SEAD pattern recorded at the corner of this individual sphere); (C) SEM image of a broken Bi_2WO_6 sample; (D) TEM image of a peeled fragment (inset: SEAD pattern recorded at this individual nanoplate) (conditions: pH = 1, hydrothermally treated at 160 °C for 20 h, no surfactant, uncalcined) [238].

It is worth noting that Amano et al. [256] have demonstrated a high photocatalytic activity of crystalline Bi_2WO_6 under visible-light (λ > 400 nm) irradiation for oxidative decomposition of gaseous acetaldehyde (AcH) to produce CO_2, however, amorphous Bi_2WO_6 sample exhibits negligible photocatalytic activity under same condition. Because the mineralization of colorless AcH does not involve a dye–sensitized process, this result provides an solid conclusion that crystalline Bi_2WO_6 has excellent visible–light–driven photocatalytic activity. Furthermore, the photocatalytic activity of crystalline Bi_2WO_6 has been finely evidenced by its diffuse reflectance photoabsorption spectrum and action spectrum, that is, 8% apparent quantum efficiency at wavelength of 400 nm [256]. In the future, much more clear evidence needs to be provided to explore the mechanism of visible–light–driven photocatalytic activity of Bi_2WO_6. [256].

Recently, Amano et al. [252] reported the preparation of Bi_2WO_6 superstructures with similar hierarchical architecture, secondary particle size, crystalline shape, exposed crystalline lattice planes, and crystalline content. The only difference is that as the increasing hydrothermal reaction temperature, their specific surface areas of the products were different due to the increase thickness of crystalline rectangular platelets. The specific surface area of the product is very important, because when levels of crystalline content of Bi_2WO_6 flake-ball particles is similar, the higher the specific surface area is, the better the photocatalysis ability it shows.

This proportional relation could be explained by the fact that the initial rate of AcH decomposition was expressed by first-order kinetics with respect to the amount of surface-adsorbed AcH, which is proportional to the specific surface area of Bi_2WO_6 samples.
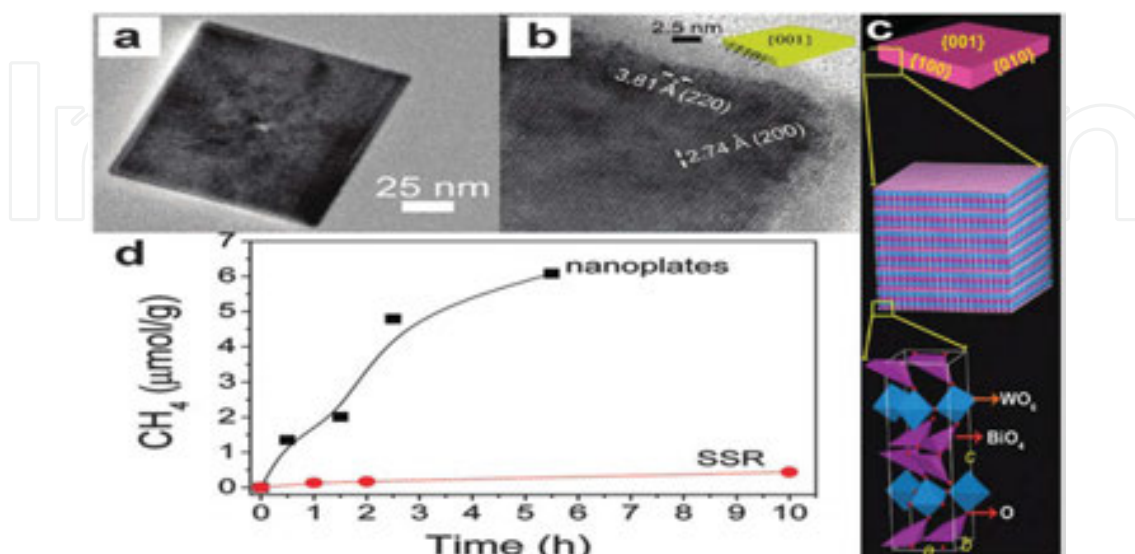

Figure 21. (a) TEM, (b) HRTEM, and (c) structural model of Bi_2WO_6 square nanoplates. (d) CH_4 generation over nanoplates and the SSR sample under visible–light irradiation ($\lambda > 420$ nm) [257].

In 2011, Zou and coworkers reported a remarkable increase in the CO_2 reduction with water to yield CH_4 over Bi_2WO_6 square nanoplates (Fig. 21 (a)–(c)) under visible-light irradiation as compared with yield over Bi_2WO_6 made by solid-state reaction (SSR) [257]. In detail, the CH_4 production rate increases from 0.045 mmol g^{-1} h^{-1} for the SSR sample to 1.1 mmol g^{-1} h^{-1} for the nanoplate catalyst (Fig. 21 (d)) [257]. Considering that the band gap of B_2WO_6 nanoplates and SSR sample is very close, geometrical factors of the photocatalyst is mainly responsible for the photoactivity enhancement. Firstly, reducing lateral dimension of the nanoplate to the nanometer scale offers a higher specific surface area. Secondly, the ultrathin geometry of the nanoplate facilitates the transfer of the charge carriers from the bulk onto the surface, where they participate in the photoreduction reaction. Thirdly, the preferentially exposed (001) crystal plane of the nanoplates is more effective than other crystal planes [257].

3.3. BiOX (X = Cl, Br, and I)

Another new class of interesting layered materials, Bismuth oxyhalides (BiOX; X = Cl, Br, and I), shows promising photocatalytic energy conversion and environment remediation ability, because of their unique layered–structure–mediated fascinating physicochemical properties and suitable band structures, along with their high chemical and optical stability, nontoxicity, low cost, and corrosion resistance [258-260]. The layered BiOX (X = Cl, Br and I) semiconductor materials, as members of the Sillen–Aurivillius family, have a tetragonal PbFCl–type structure (space group *P*4/*nmm*), which consists of [X–Bi–O–Bi–X] slices stacked together by the nonbonding (van der Waals) interactions through halogen atoms along the *c*-axis [261]. In each

[X−Bi−O−Bi−X] layer, a bismuth center is surrounded by four oxygen and four halogen atoms, creating an asymmetric decahedral geometry. The covalent bonds is the interaction bond within the [Bi_2O_2] layers, whereas the [X] layers are stacked together by van der Waals, forces (nonbonding interactions) between the X atoms along the c-axis. The strong intralayer covalent bonding and the weak interlayer van der Waals interaction can induce the formation of layered structures. For BiOX crystals, the valance band maximum mainly comprises of O2p and X np states (n = 3, 4, and 5 for X = Cl, Br and I, respectively) and the Bi 6p states dominate the conduction band minimum [262-266]. As the atomic numbers of X increases, the contribution of X ns states increases remarkably, and the dispersive characteristic of band energy level becomes more and more striking, thereby narrowing the band gap. Taking BiOCl, for example, as illustrated in Fig. 22, BiOX (X = Cl, Br, I) are characterized by the layered structure that are composed of [Bi_2O_2] slabs interleaved with double halogen atom slabs along the [001] direction. A highly anisotropic structural, electrical, optical, and mechanical properties of this material origin from the nature of its strong intralayer covalent bonding and the weak interlayer van der Waals, interaction, this unique structure allows BiOX to apply in many promising potential applications including photocatalytic wastewater and indoor-gas purification, water splitting, organic synthesis, and selective oxidation of alcohol [267-277].
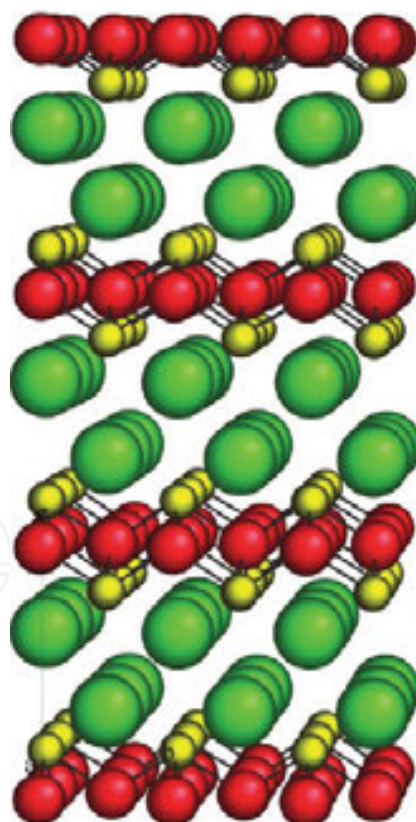

Figure 22. The schematic diagram of crystal structure of BiOCl (green, Cl atoms;yellow, Bi atoms; red, O atoms) [278].

One−dimensional nanostructures (1D), which refers to the materials with nanoscaled thickness and width, while the length can be several micrometers or longer, is considered to be promising

in photocatalysis application. The prolonged length scale may allow the 1D nanomaterials to contact the macroscopic world for various measurements [279,280]. Besides, the high aspect ratio of 1D nanostructured semiconductors also facilitates the fast photoexcited electron-hole separation, which is favorable for highly efficient photocatalytic reactions.
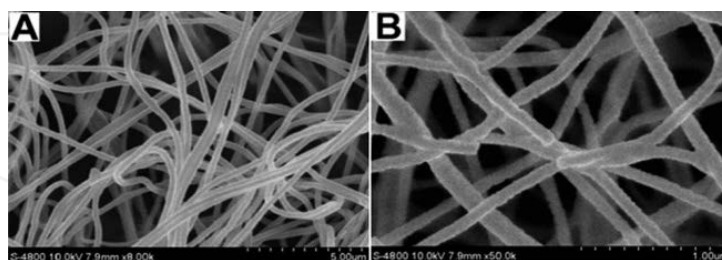

Figure 23. SEM images of the prepared (A) PAN/BiCl$_3$ nanofibers and (B) BiOCl nanofibers [281].

BiOX (X = Cl, Br and I) material is naturally preferentially grow into nanoplates/sheets with 2D features due to its highly anisotropic layered structures. As a result, hard templates for the synthesis of the 1D bismuth oxyhalide nanostructures is commonly used, becaused the template can be easily removed by subsequent thermal or chemical treatments [281-283]. For example, Liu et al. [281] developed the electrospinning method to synthesize BiOCl nanofibers, as shown in Fig. 23. After thermal removal of the polyacrylonitrile (PAN) template at 500°C for 10 h, they can obtain the BiOCl nanofibers with diameters ranging from 80 to 140 nm. Interestingly, the as-prepared BiOCl nanofibers showed high activity towards rhodamine B (RhB) degradation under the UV irradiation, and the photodegradation rate was found to be about three times faster than that of Bi$_2$O$_3$ nanofibers obtained in the same way. In addition to PAN, some other templates involving activated carbon fibers (ACFs) [282] and anodic aluminium oxide (AAO) [283] have also been used to prepare BiOCl nanofibers/nanowire arrays, which displayed efficient photocatalytic performance in the degradation of organic dyes.

In the past few years, 2D nanomaterials, such as graphene, transition metal dichalcogenides and layered double hydroxides (LDHs), have gained great attention for their extraordinary physical/chemical features and promising applications in a great deal of applications [284-287]. Intrinsically, van der Waals bonds or electrostatic forces between the layer structure in such 2D nanostructures is the origin of its lamellar structure. Similarly, the layered structure makes BiOX (X = Cl, Br and I) tend to the intrinsic 2D nanostructures, such as nanoplates, nanosheets and nanoflakes. The formed intra-electric field between [Bi$_2$O$_2$] layers and halogen atom layers could accelerate the transfer of the photo-induced carriers and enhance the photocatalytic activity of BiOX (X = Cl, Br and I) [288].

To date, numerous synthetic methodologies have been exploited for the preparation of 2D BiOX nanomaterials, such as hydrolysis, [288-292] hydrothermal/solvothermal synthesis, [293-295] and thermal annealing [296]. For instance, recently, Zhang's group [293] has synthesized 2D BiOCl nanosheets with predominantly exposed {001} and {010} facets by selective addition of the mineralizing agent NaOH. Interestingly, BiOCl nanosheets with exposed {001}

facets displayed higher UV–induced photocatalytic degradation of MO dye, while the counterpart with exposed {010} facets exhibited higher degradation activity under visible light. On the one hand, the generated internal electric field along the [001] direction is more favorable for direct semiconductor photoexcitation under UV irradiation as shown in Fig. 24, which was also confirmed by the higher photocurrent of {001} facets than that of {010} facets from the transient photocurrent responses. On the other hand, compared with {001} facets, the larger surface area and open channel feature of {010} facets facilitate the adsorption of dye molecules, which further results in its better indirect dye photosensitization performance under visible light irradiation.
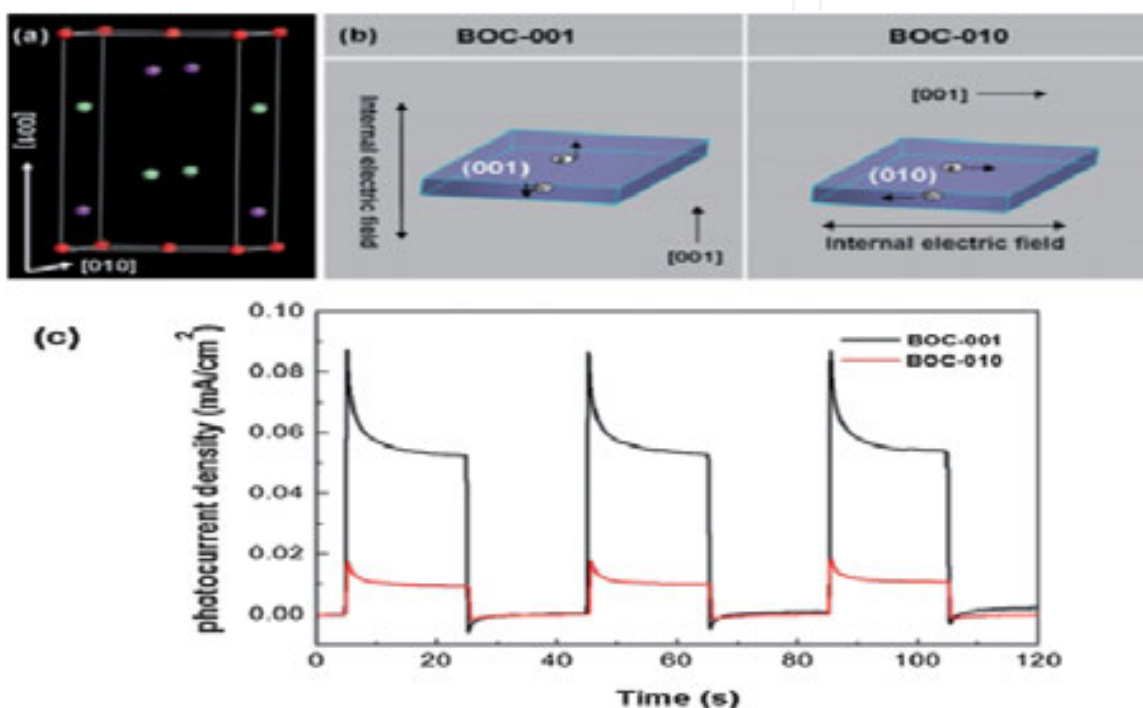

Figure 24. (a) Crystal structure of BiOCl. (b) Model showing the direction of the internal electric field in each of the BiOCl nanosheets. (c) Photocurrent responses of the BiOCl nanosheets in 0.5 M Na₂SO₄ aqueous solutions under UV-vis irradiation [293].

Researches have also using density functional theory (DFT) computations to reveal the nature of such a facet-dependent photocatalytic property in BiOX (X = Cl, Br and I) [297]. The halogen X−terminated {001} facets shows great thermodynamic stability and could efficiently separate photo-generated electron−hole pairs, whereas the formation of deep defect levels in the band gap of BiX−terminated {110} and other facets with surface O vacancies are bad for the carrier separation. This finding reveals the insight into the fundamental facet determined photocatalysis of BiOX (X = Cl, Br and I), which explains the superior photocatalytic performance of BiOX (X = Cl, Br and I) nanosheets with higher percentage of {001} facets than those with lower ones [289,290,296].

Self-assembly is a strong tool in nanotechnology fabrication of making low dimensional (e.g., 1D nanorods, 2D nanosheets, etc.) materials into their higher−dimension (3D) multifunctional

superstructures, which plays a major role in material synthesis and device engineering and has been paid much attention recently [298-302]. Comparison with 1D and 2D nanostructures, 3D hierarchical nano/microstructures, which integrate the features of the nanoscale building units and their assembled architectures, are more attractive for solar energy storage and conversion [300-302]. Furthermore, 3D architectures could endow the BiOX (X = Cl, Br, I) semiconductors with improved light harvesting, shortened diffusion pathways, faster interfacial charge separation and more reactive sites, thus enhancing their photocatalytic efficiencies.

Hydro/solvothermal routes are definitely the most robust method among the methodological synthesis of the 3D BiOX (X = Cl, Br and I) hierarchical assemblies, [303-322] which are usually carried out at critical conditions of water or other organic solvents. In 2008, a generalized solvothermal process has been developed by Zhang et al. [303], who use ethylene glycol (EG) to prepare BiOX (X = Cl, Br, and I) hierarchical microspheres from 2D nanoplates. The band gaps of the resulting BiOX (X = Cl, Br and I) samples are calculated to be 3.22, 2.64, and 1.77 eV for BiOCl, BiOBr, and BiOI, respectively. Under visible-light irradiation, the BiOI sample exhibited the best photocatalytic performance with the order of BiOI > BiOBr > BiOCl evaluated by MO dye solution degradation. Almost at the same time, Tang et al. [304] also prepared 3D microspherical BiOBr architectures assembled by nanosheets through EG–assisted solvo-thermal synthesis. The band gap of the BiOBr architectures is 2.54 eV, so it shows higher photocatalytic activity for MO decomposition under visible–light irradiation than the BiOBr bulk plates.

How to realize the hierarchical architectures in the microstructure modulation of BiOX (X = Cl, Br and I) nano/microstructures with hollow voids draws much attention due to their better penetrability and higher light utilization. Recently, Huang group [313] has developed a method to synthesize uniform BiOBr hollow microspheres in the presence of 2-methoxyethanol solvent a mini-emulsion-mediated solvothermal route. The size of the BiOBr hollow microspheres is in the in the range of 1-2 mm and shell thickness of about 100 nm, which are composed of numerous interlaced 2D nanosheets. As demonstrated in Fig 25, by observing a Tyndall effect of the precursor suspension, the author confirmed that the 1–hexadecyl–3–methylimidazolium bromide ionic liquid ([C16Mim]BrIL) can not only serve as a Br source but also create a colloidal mini-emulsions. The diameter of the BiOBr hollow microsphere is determined by the size of the of the emulsion because the reaction takes place at the phase interface edge of the mini–emulsion rather than in the itself. Under visible-light irradiation, such BiOBr hollow microspheres displayed superior photocatalytic activity in degradation of RhB dye and reduction of Cr^{VI} ions to the samples with micro-flower shape. Xia and co-workers [319] prepared BiOI hollow microspheres by the EG–assisted solvothermal method using 1-butyl-3-methylimidazoliumio-dine ([Bmim]I) IL as the reactive templates and I source. Under visible-light irradiation, such 3D BiOI hollow microspheres exhibited higher photocatalytic activity toward MO degrada-tion than that of 2D BiOI nanoplates. Besides the halide ion-containing ILs [304,304,312,314,317,322], surfactants such as poly(vinylpyrrolidone) (PVP) [308] and hexadecyl-trimethylammonium bromide (CTAB) [311,312,314,316,318,319] have been used to tailor the self-assembly process of the BiOX (X = Cl, Br, I) hierarchical architectures, and in particular CTAB could act as reactive template to provide Br - ions for BiOBr.
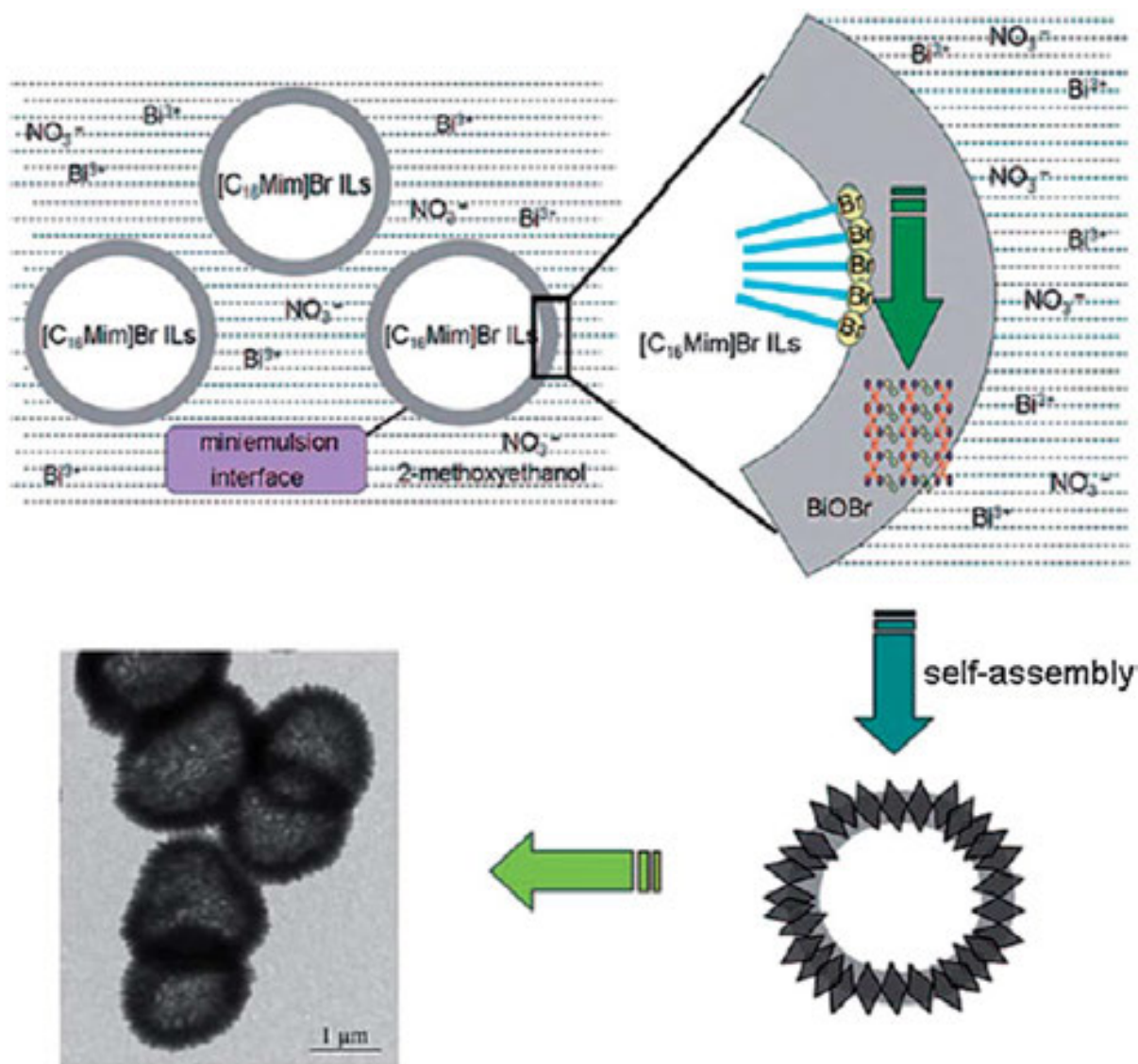
Figure 25. The schematic formation process of the BiOBr hollow microspheres by the mini-emulsionmediated solvo-thermal route [313].

Apart from the hydro/solvothermal syntheses, other synthetic procedures are also used to synthesize the ordered superstructures of BiOX (X = Cl, Br and I) semiconductors, such as hydrolysis [323,324], direct precipitation [325,326], sonochemical route [327,328], refluxing method [329], chemical bath [330] and solution oxidation process [331]. For example, Xiong and co-workers [331] reported a rapid in situ oxidation process to fabricate 3D flower-like BiOCl hierarchical nanostructures by reacting metallic Bi nanospheres and $FeCl_3$ aqueous solution at room temperature. As illustrated in Fig. 26, in the presence of Cl- ions, the redox potential of Bi species could be reduced from +0.308 V (Bi^{3+}/Bi vs. SHE) to +0.16 V (BiOCl/Bi). Therefore, the high redox potential of Fe^{3+} ($E(Fe^{3+}/Fe^{2+}) = +0.771$ V) could oxidize the surface of Bi nanospheres into the final 3D BiOCl hierarchical nanostructures. Compared with the commercial BiOCl sample, such flower-like BiOCl nanostructures obtained displayed much better RhB photodegradation activity and higher photoelectric conversion performances.
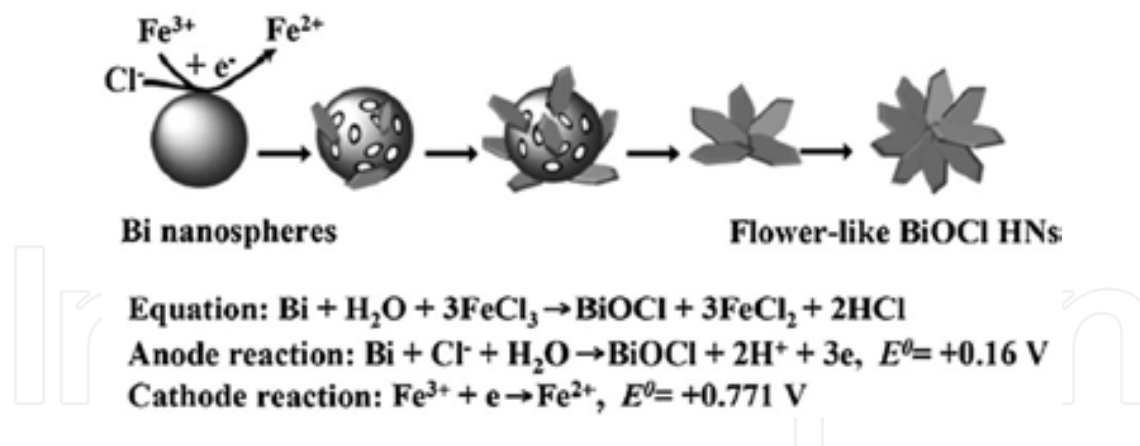
Figure 26. Schematic illustration of the fabrication of flower−like BiOCl hierarchical nanostructures by an in situ oxidation process [331].

Interestingly, Zhang [332] found that the photoactivity of BiOCl nanosheets shows a highly exposed facet-dependent effcet. The BiOCl nanosheets with exposed {001} facets showed higher direct semiconductor photoexcitation activity towards pollutant degradation due to both the surface atomic structure and suitable internal electric fields under UV light irradiation. Under visible light, highly exposed {010} facet BiOCl nanosheets shows superior indirect dye photosensitization activity for methyl orange degradation, which is due to the larger surface area and open channel characteristic of BiOCl nanosheets. It is belived that the enlarged surface area and open channel could enhance the adsorption capacity of methyl orange molecules as well as provide more contact sites between the photocatalyst and dye molecules, thereby facilitating the indirect dye photosensitization process because more efficient electron injection from the photoexcited dye into the conduction band of the catalyst happened (Fig. 27). These findings not only clarified the origin of facet-dependent photoreactivity of BiOCl nanosheets but also provided effective guidance for the design and fabrication of highly efficient bismuth oxyhalide photocatalyst.
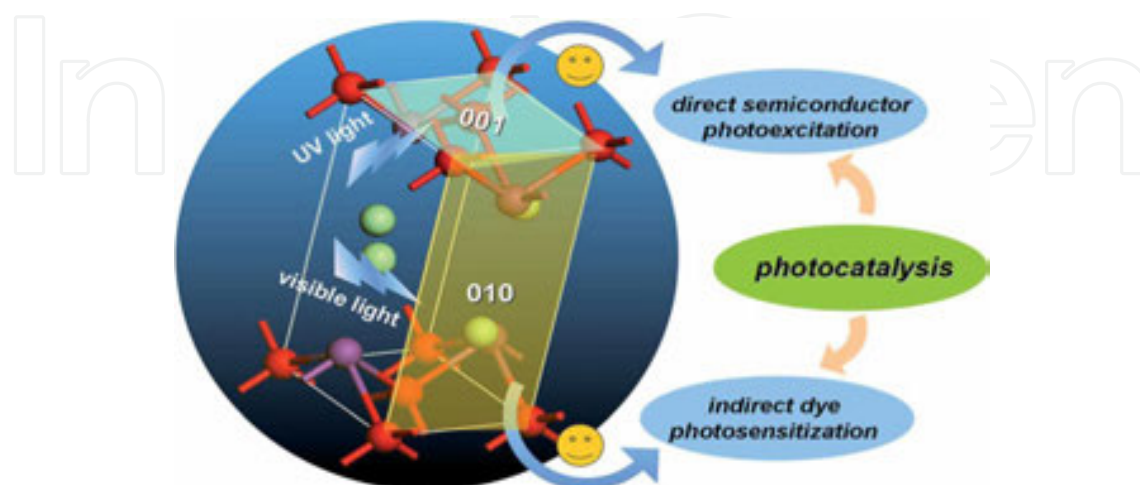

Figure 27. Schematic illustration of facet-dependent photoreactivity of BiOCl single-crystalline nanosheets [332].
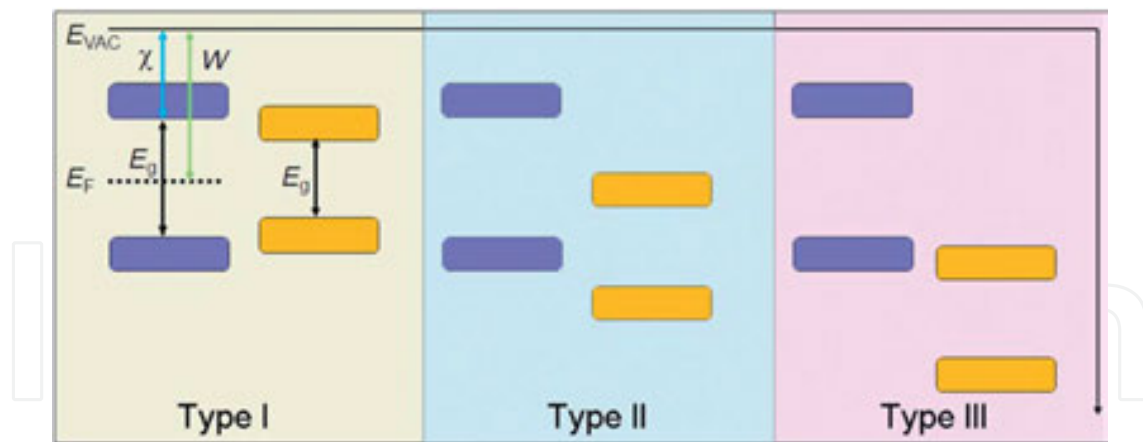
Figure 28. Schematic diagram of three types of semiconductor heterostructures [338].

It is speculated by Ye et al. that oxygen vacancy induced by UV light could yield an intermediate state between the valence and conduction bands to narrow the band gap, which may make oxygen−deficient BiOCl a promising alternative for the visible−light−driven photocatalytic reaction [333,334]. Zhang group recently found that oxygen vacancies of BiOCl can be created by the reductive ethylene glycol because it could easily react with the oxygen −terminated (001) surface at 160°C, which is evidenced by the electron spin resonance (ESR) spectra [335]. The resulting oxygen vacancies not only extended the light-response edge up to 650 nm but also enabled the effective capture of photoinduced electrons and molecular oxygen to generate superoxide anion radicals, both of which are of great important for realizing high photocatalysis efficiency of the photocatalyst. Recently, Xie et al. demonstrated that with the reduced thickness of the {001} facet−dominant BiOCl nanosheets to the atomic scale, the defects mainly change from isolated defects to triple vacancy, which could significantly promote the sunlight−driven photocatalytic activity of BiOCl nanosheets. The enhanced adsorption capability, the separation of electron-hole pairs and the generated reductive photoexcited electrons is mainly responsible for this improvement [261].

4. Composites systems

In contrast to one individual semiconductor photocatalyst, semiconductor composites are more intriguing for their interfacial heterostructures, which are formed at their junctures and have an important effect on their photocatalytic performances. There are usually three types of band positions in semiconductor heterojunctions: straddling gap (type I), staggered gap (type II) and broken gap (type III), as presented in Fig. 28. Among them, semiconductor composites with the staggered gap (type II) have drown much attention in the field of heterogeneous photocatalysis [336,337]. In this system, the photoinduced electrons and holes can be easily separated at the interface of the two semiconductors via effective interfacial charge transfer, thereby enhances the photocatalytic performance of the semiconductor composites.

4.1. Binary composite

In recent years, tremendous efforts have been made in surface modification of TiO_2 nanomaterials with other semiconductors. Most of these systems possess a high dye adsorption capacity, an extended light absorption range, enhanced charge separation, promoted mass-transfer and thus improved photocatalytic efficiency. This semiconductor provides the best compromise between catalytic performance and stability in aqueous media. Therefore, the magnetic iron oxide/TiO_2 composite photocatalysts have become the research focus in recent years. Using the magnetic properties of iron oxide itself for obtaining the magnetic recoverable photocatalyst has become an important issue in the magnetic iron oxide/TiO_2 composite photocatalyst system [339-342]. For instance, Wang and coworkers have reported the fabrication of core–shell $Fe_3O_4@SiO_2@TiO_2$ microspheres through a wet–chemical approach. The microspheres possess both ferromagnetic and photocatalytic properties. The TiO_2 nanoparticles on the surfaces of the microspheres degraded organic dyes under the illumination of UV light. Furthermore, the microspheres were easily separated from the solution after the photocatalytic process due to the ferromagnetic Fe_3O_4 core. The photocatalysts were recycled for further use and the degradation rate of methyl orange still reached 91% after six cycles of reuse [343]. As shown in Fig. 29, Chalasani and Vasudevan have demonstrated water-dispersible photocatalytic $Fe_3O_4@TiO_2$ core–shell magnetic nanoparticles by anchoring carboxy–methyl beta–cyclodextrin (CMCD) cavities to the TiO_2 shell, and photocatalytically destroyed endocrine-disrupting chemicals, bisphenol A (BPA) and dibutyl phthalate, present in water. The particles, which were typically 12 nm in diameter, were magnetic and removed from the dispersion by magnetic separation and then reused. The concentration of BPA solution was determined by liquid chromatography, and then irradiated under UV light for 60 min. After photodegradation of BPA, the CMCD−$Fe_3O_4@TiO_2$ nanoparticles that were separated from the mixtures by a magnet, and can be reused for the photodegradation of newly prepared BPA solutions. The recycle photocatalytic performance of CMCD−$Fe_3O_4@TiO_2$ for the photodegradation of BPA was excellent and stable, retaining 90% efficiency after 10 cycles [345]. For obtaining the magnetically recovered photocatalysts, Fe_3O_4 and γ-Fe_2O_3 were often employed due to their higher saturation magnetization and good magnetic separation ability.

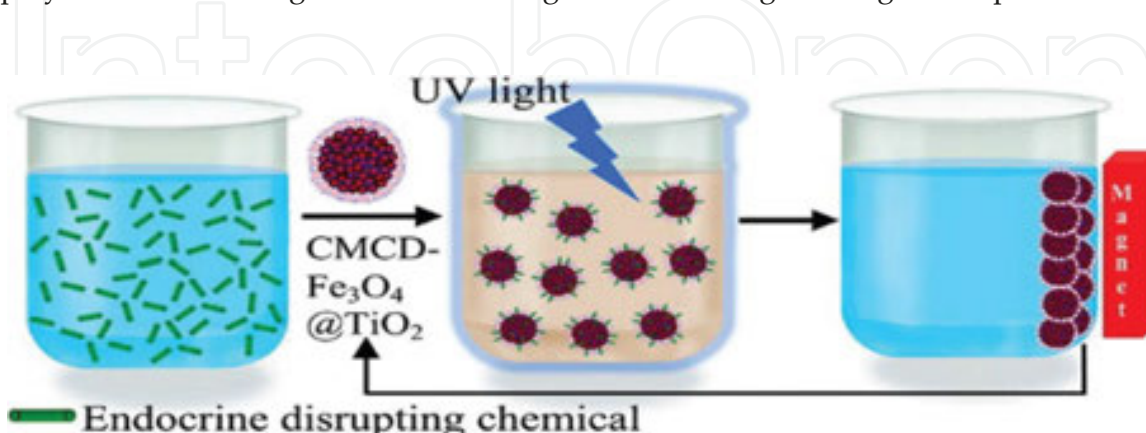**Figure 29.** Scheme for the reuse of cyclodextrin-functionalized $Fe_3O_4@TiO_2$ for photocatalytic degradation of endocrine-disrupting chemicals in water supplies [344].

On the other hand, α-Fe_2O_3 has often been introduced into the magnetic iron oxide/TiO_2 composite photocatalyst in order to use its narrow band gap properties and to obtain magnetic iron oxide/TiO_2 composite heterostructures [344-348]. For example, Peng and coworkers have synthesized Fe_2O_3/TiO_2 heterostructural photocatalysts by impregnation of Fe^{3+} on the surface of TiO_2 and annealing at 300°C, the composites possess different mass ratios of Fe_2O_3 vs. TiO_2. The photocatalytic activities of Fe_2O_3/TiO_2 heterocomposites, pure Fe_2O_3 and TiO_2 were studied by the photocatalytic degradation of Orange II dye in aqueous solution under visible-light ($\lambda > 420$ nm) irradiation. The Fe_2O_3/TiO_2 heterogeneous photocatalysts exhibited an enhanced photocatalytic ability for Orange II, higher than either pure Fe_2O_3 or TiO_2. The best photocatalytic performance for Orange II could be obtained when the mass ratio in Fe_2O_3/TiO_2 is 7 : 3. The results illustrate that the generation of heterojunctions between Fe_2O_3 and TiO_2 is key for improving movement and restraining the recombination of photoinduced charge carriers, and finally improving the photocatalytic performance of Fe_2O_3/TiO_2 composites [348]. Recently, Palanisamy and coworkers have prepared Fe_2O_3/TiO_2 (10, 30, 50, 70 and 90 wt% Fe_2O_3) photocatalysts by a sol-gel process. Mesoporous Fe_2O_3/TiO_2 composites exhibited excellent photocatalytic degradation ability for 4−chlorophenol in aqueous solution under sunlight irradiation. The author claimed that the photogenerated electrons in the VB of TiO_2 are transferred to Fe(III) ions resulting in the reduction of Fe(III) ions to Fe(II) ions. Thus, the photoinduced holes in the VB of Fe_2O_3/TiO_2 cause an oxidation reaction and decompose the 4-chlorophenol to CO_2 and H_2O. Meanwhile the transferred electrons in Fe(III) ions could trigger the reduction reaction [349].

Wang's group successfully synthesized Bi_2WO_6-TiO_2 hierarchical heterostructure through a simple and practical electrospinning-assisted route (Fig. 30 (A) and (B)) [350]. As shown in Fig. 30 (A), Bi_2WO_6 nanoplates grew aslant on the primary TiO_2 nanofibers. These three dimensional (3D) Bi_2WO_6−TiO_2 hierarchical heterostructures exhibited enhanced visible−light −driven photocatalytic activity for the decomposition of CH_3CHO, which was almost eight times higher than that of the Bi_2WO_6 sample, and the decomposition rate by the bare TiO_2 could be neglected under visible light irradiation. This high photocatalytic activity was ascribed to the reduced probability of electron−hole recombination and the promoted migration of photogenerated carriers. Similarly, Wang et al. [352] fabricated SnO_2−TiO_2 heterostructured photocatalysts based on TiO_2 nanofibers by combining the electrospinning technique with the hydrothermal method (Fig 30C and D). This SnO_2−TiO_2 composite possessed a high photocatalytic activity for the degradation of rhodamine B (RhB) dye under UV light irradiation, which was almost 2.5 times higher than that of the bare TiO_2. The enhanced photocatalytic efficiency was attributed to the improvement of the separation of photogenerated electrons and holes. Wang's group [352] prepared a graphene−Bi_2WO_6 composite via an in situ hydrothermal reaction (Fig. 31(A) and (B)). This graphene−Bi_2WO_6 photocatalyst showed significantly enhanced photocatalytic activity for the degradation of RhB under visible light ($\lambda > 420$ nm), which was three times greater than that of the pure Bi_2WO_6. The enhanced photocatalytic activity could be attributed to the negative shift in the Fermi level of graphene−Bi_2WO_6 and the high migration efficiency of photoinduced electrons; these electrons may not only be effectively involved in the oxygen reduction reaction but also suppress the charge recombination. Kudo et al. [353] reported the composite of reduced graphene oxide (RGO) with

BiVO$_4$, where an significantly improved PCE activity of a near 10–fold enhancement was observe compared with pure BiVO$_4$ under visible-light irradiation. The longer photoexcited electron lifetime of BiVO$_4$ is mainly responsible for this improvement as the electrons are injected to RGO instantly at the site of generation, leading to a significant reduction in charge recombination.
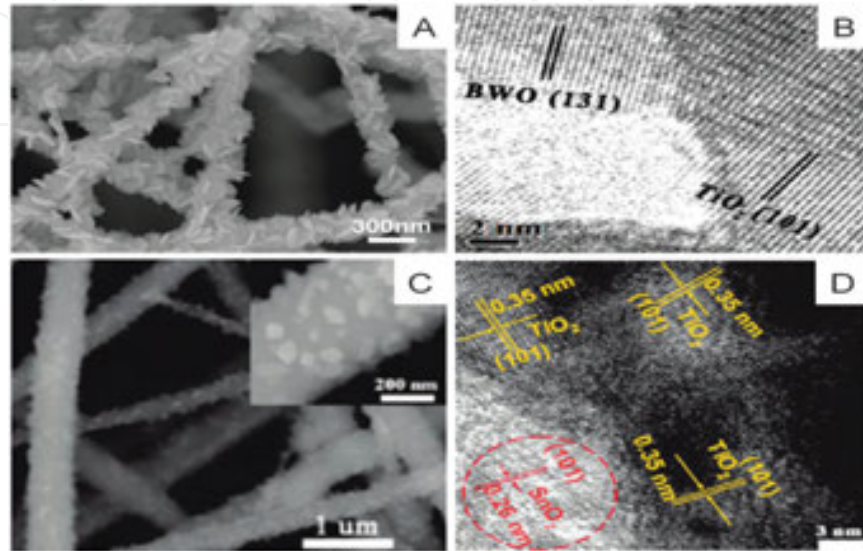

Figure 30. SEM (A) and HRTEM (B) images of Bi$_2$WO$_6$/TiO$_2$ [343]; SEM (C) and HRTEM (D) images of SnO$_2$/TiO$_2$ heterostructures [351].
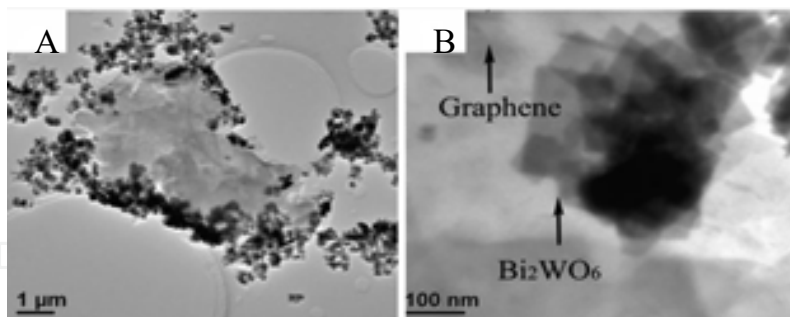

Figure 31. (A and B) TEM images of graphene decorated with Bi$_2$WO$_6$ composite [352].

A simple soft-chemical method was used to synthesize the BiOI/TiO$_2$ heterostructures with different Bi to Ti molar ratios at low temperature of 80°C. The degradation of methyl orange under visible-light irradiation (λ > 420 nm) of the material revealed that the BiOI/TiO$_2$ heterostructures exhibited much higher photocatalytic activities than pure BiOI or TiO$_2$, where 50%BiOI/TiO$_2$ showed the best activity among all these heterostructured photocatalysts [348]. BiOBr–Bi$_2$WO$_6$ mesoporous nanosheet composite enhanced photocatalytic activity is attributed to well-matched band edge positions of BiOBr and Bi$_2$WO$_6$ and the large specific surface area of the mesoporous nanosheet composites in view of the incorporation of mesopores and

the highly exposed BiOBr (001) facet, compared with pure BiOBr and Bi_2WO_6 under exposure to a 3–W LED light [354].

During the past few years, another promising carbon material, graphene, which possess many unique properties, has been used for corporation with BiOX (X = Cl, Br and I) and significantly improved photocatalytic efficiencies was achieved [356-360]. Ai and coworkers [357] have developed a facile solvothermal route tosynthesize BiOBr/graphene hybrids using graphene oxide (GO), bismuth nitrite, and CTAB as the precursors. As shown in Fig. 32, BiOBr nanoplates with hundreds nanometers in size are dispersed randomly on the 2D graphene sheet surface. Evaluated by the removal of gaseous NO under visible-light irradiation, the as-prepared BiOBr/graphene hybrid displays a two times higher removal rate than that of pure BiOBr. It is evidenced that the strong chemical bonding between BiOBr and graphene is mainly responsible for the fast photogenerated electrons transfer from BiOBr to graphene, which further inhibits the unwanted recombination and leading to its enhanced photocatalytic activity.
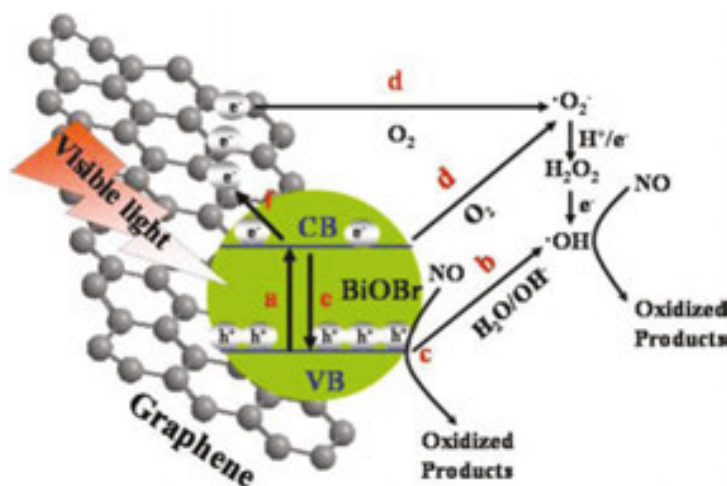

Figure 32. Schematic illustration of the visible–light photocatalytic enhancement of BiOBr/graphene nanocomposites [357].

4.2. Ternary composite

To date, although a variety of approaches have been developed to prepare many kinds of visible–light–driven semiconductor heterojunction photocatalysts, many shortage is still needed to be overcomed, for example, the limited region of visible-light photo–response. To solve these problems, multi–component heterojunction systems have been developed [361,362], in which two or more visible-light active components and an electron-transfer system are spatially integrated as shown in Fig. 33 [363].

As demonstrated in Figure 33, since both semiconductor A (S-A) and semiconductor B (S-B) can be excited by UV/visible light and have different photoabsorption ranges, the conjunction of the two materials can overlap and broaden the range of UV/visible–light photoresponse. At the same time, it is well-known that the photocatalytic reaction is initiated by the incident UV/
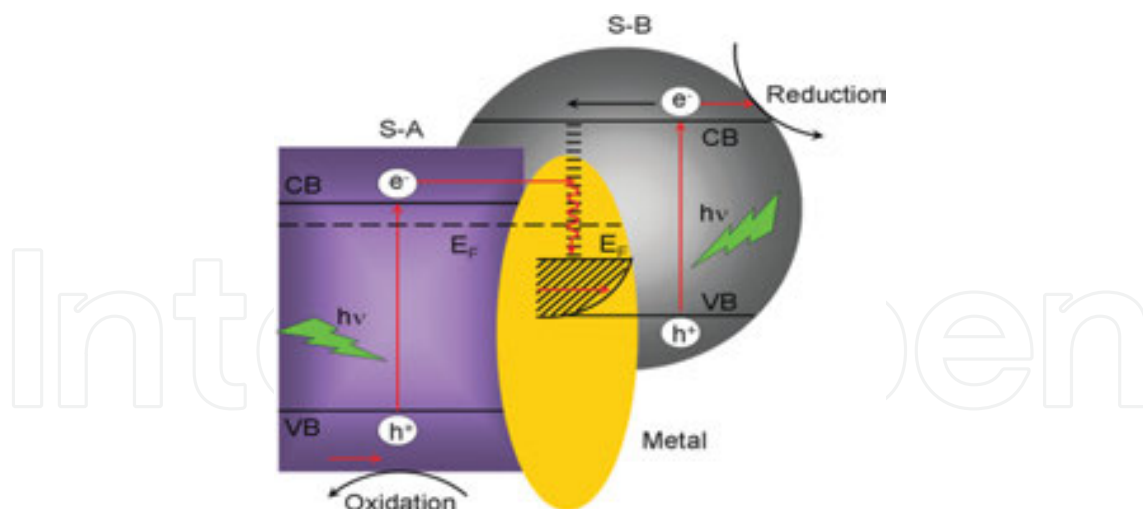
Figure 33. Schematic structure of multicomponent heterojunction systems [363].

visible photons with energy equal or higher than the band-gap in both S−A and S-B, which lead to the creation of photogenerated holes in their VB and electrons in their CB. On the one hand, the electrons in the CB of S−A easily flow into metal (electron transfer I: S−A metal) through the Schottky barrier because the CB (or the Fermi level) of S−A is higher than that of the loaded metal, which is consistent with the previous study on electron transfer from the semiconductor (such as TiO_2) to metal (such as Ag and Au) [361,364]. This process of electron transfer I is faster than the electron-hole recombination between the VB and the CB of S−A. Thus, plenty of electrons in the CB of S−A can be stored in the metal component. As a result, more holes with a strong oxidation power in the VB of S−A escape from the pair recombination and are available to oxidize the pollutants or OH-. On the other hand, since the energy level of metal is above the VB of S−B, holes in the VB of S−B also easily flow into metal (electron transfer II: metal S−B, see Fig. 33), which is faster than the electron-hole recombination between the VB and CB of S−B. More electrons with a strong reduction power in the CB of S−B can escape from the pair recombination and are available to reduce some absorbed compounds (such as O_2 and H^+). Therefore, simultaneous electron transfer I and II (i.e., vectorial electron transfer of S−A metal to S−B in Fig. 33) can occur as a result of UV/visible-light excitation of both S−A and S−B. In these vectorial electron−transfer processes, metal in multicomponent heterojunction systems acts as a storage and/or a recombination center for electrons in the CB of S−A and holes in the VB of S−B, and contributes to enhancing interfacial charge transfer and realizing the complete separation of holes in the VB of S−A and electrons in the CB of S−B. Therefore, the multi-component heterojunction systems can simultaneously and efficiently generate holes with a strong oxidation power in the VB of S−A and electrons with a strong reduction power in the CB of S−B, resulting in greatly enhanced photocatalytic activity, compared with the single semiconductor or semiconductor heterojunctions mentioned above.

In 2006, by using a facile photo−chemical technique, Tada et al. [361] developed a CdS−Au −TiO_2 ternary component nanojunction system (Fig. 34 (A) and (B)). This CdS−Au−TiO_2 triple nanojunction shows significantly improved photocatalytic activity, which was far higher than that of either the single-component or two−components systems. For this photocatalytic CdS

−Au−TiO$_2$ nanojunction system, 52.2% of methylviologen (MV^{2+}) have been reduced in 100 min, which are 1.6, 1.8 and 2.3 times higher than that of Au/TiO$_2$, CdS/TiO$_2$ and TiO$_2$ [361].
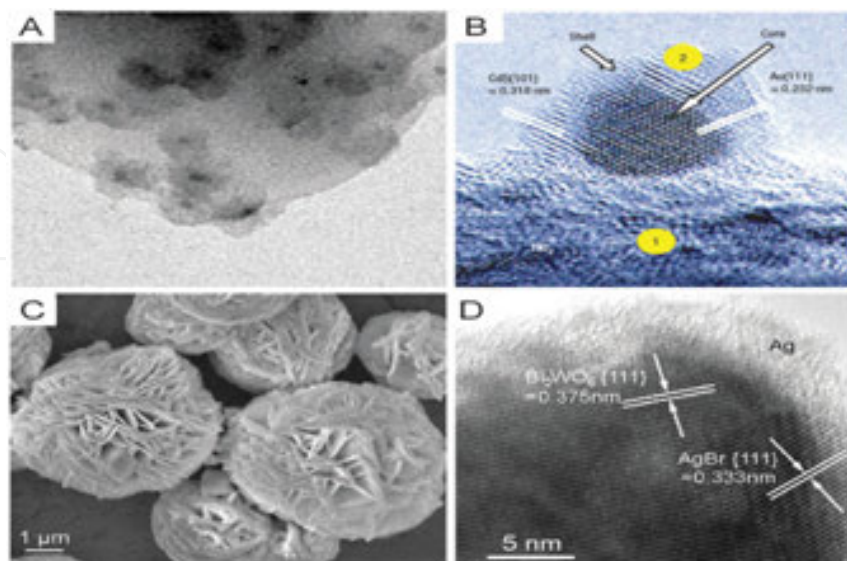

Figure 34. TEM (A) and HRTEM (B) images of Au@CdS−TiO$_2$ [361]; SEM(C) and HRTEM (D) images of the AgBr−Ag −Bi$_2$WO$_6$ nanojunction system [364].

Subsequently, an AgBr−Ag−Bi$_2$WO$_6$ nanojunction system was developed by a facile deposition −precipitation method (Fig. 34 (C) and (D)) [364]. This AgBr−Ag−Bi$_2$WO$_6$ nanojunction system shows much higher visible−light−driven photocatalytic activity than a photocatalyst with single visible-light response components, such as Bi$_2$WO$_6$ nanostructures, Ag−Bi$_2$WO$_6$ and AgBr−Ag−TiO$_2$. For example, with the AgBr−Ag−Bi$_2$WO$_6$ nanojunction system as the photo-catalyst, the MX−5B could be photocatalytically degraded (42.8 mg L^{-1}) within 60 min under visible-light irradiation, which is higher than that of Bi$_2$WO$_6$ nanostructures (2.0 mg L^{-1}), Ag-Bi$_2$WO$_6$ (2.9 mg L^{-1}) and AgBr−Ag−TiO$_2$ (34.1 mg L^{-1}). Furthermore, 65% of pentachlorophenol could be mineralized within 4 h by AgBr−Ag−Bi$_2$WO$_6$, which is much higher than that (34.5%) of the AgBr−Ag−TiO$_2$ composite. This excellent visible−light−driven photocatalytic perform-ance was mainly attributed to the vectorial interparticle electron transfer driven by the two-step excitation of both visible-light-driven components (AgBr and Bi$_2$WO$_6$).

A one-step low−temperature chemical bath method was developed to synthesize the flower −like Ag/AgCl/BiOCl composite [365]. The as−prepared Ag/AgCl/BiOCl composite exhibited enhanced visible−light photocatalytic activity on photodegradation of rhodamine B, which was greatly improved in comparison with either pure Ag/AgCl or BiOCl. It is evidenced that the superoxide radical, chlorine radical and the hole play a critical role in the photocatalytic degradation of RhB over the Ag/AgCl/BiOCl. Next, Ag/AgX/BiOX (X = Cl, Br) three-compo-nent visible-light-driven photocatalysts were synthesized by a low−temperature chemical bath method (Fig. 35) [366]. The Ag/AgX/BiOX composites showed enhanced visible−light−driven photocatalytic activity for the degradation of rhodamine B, which was much higher than Ag/AgX and BiOX. The photocatalytic mechanisms were analyzed by active species trapping and

superoxide radical quantification experiments. The role of metallic Ag in Ag/AgCl/BiOCl and Ag/AgBr/BiOBr were analyzed, and we found that the role of metallic Ag was a surface plasmon resonance and the Z−scheme bridge for Ag/AgCl/BiOCl and Ag/AgBr/BiOBr, respectively. This results suggests that no matter in narrow band gap photocatalysts (Eg < 3.1 eV) or wide band gap photocatalysts (Eg > 3.1 eV), metallic Ag can enhance visible-light-driven photocatalytic activity though the different roles.
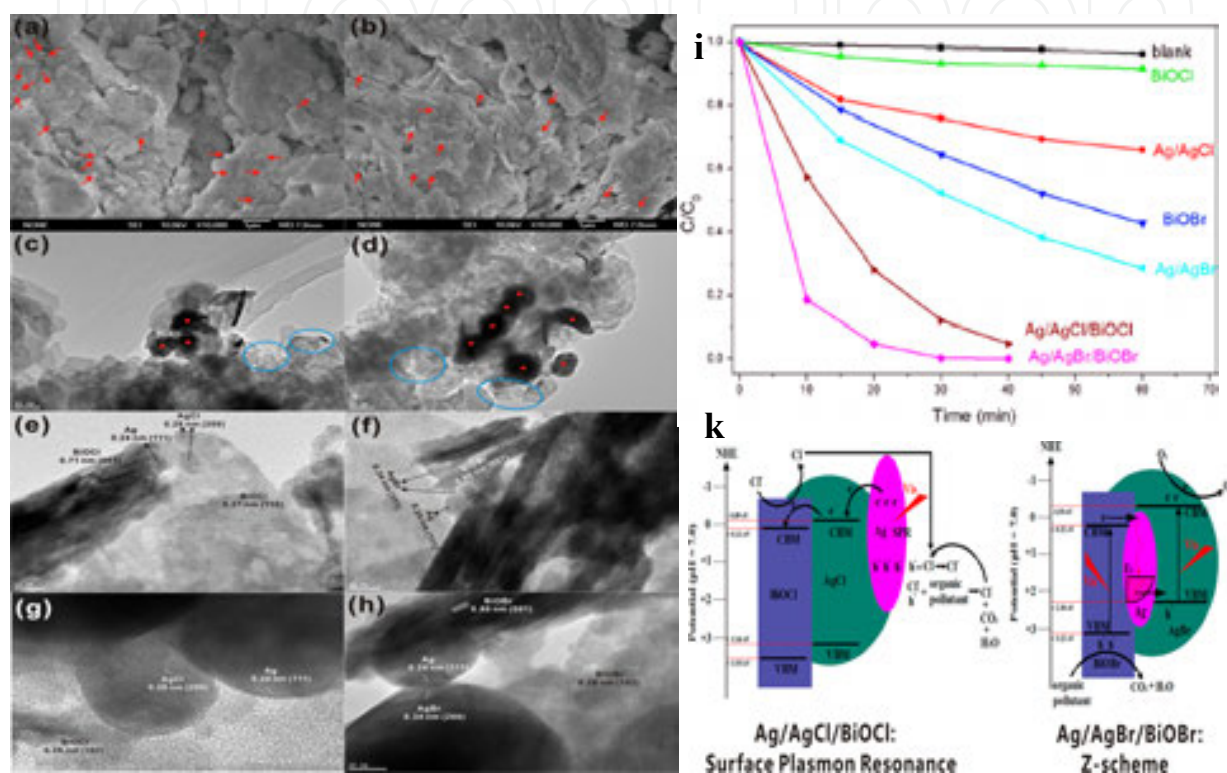

Figure 35. FESEM images of Ag/AgCl/BiOCl (a) and Ag/AgBr/BiOBr (b): the red arrows pointing out the Ag/AgX. TEM images of Ag/AgCl/BiOCl (c) and Ag/AgBr/BiOBr (d): blue rings show the small Ag/AgX, and the red dots point out the large Ag/AgX. HRTEM images of Ag/AgCl/BiOCl (e) and Ag/AgBr/BiOBr (f) with small Ag/AgX and HRTEM images of Ag/AgCl/BiOCl (g) and Ag/AgBr/BiOBr (h) with large Ag/AgX (i)the photocatalytic degradation percentage of RhB under visible-light irradiation ($\lambda \geq 400$ nm) and (k) schematic structure of multicomponent heterojunction systems [366].

Recently, our group has demonstrated a simple and efficient one-pot approach to prepare Ag/ r−GO/TiO$_2$ composites using solvothermal method under atmospheric pressures (Fig. 36) [367], where N,N−dimethylacetamide serves as the reducing agent for Ag and GO reduction. On account of the experimental result, we concluded that the introduction of Ag into classical graphene/TiO$_2$ system (i) availably expands the absorption range, (ii) improves the photogenerated electron separation and (iii)increases the photocatalysis reaction active sites. The optimized composite sample exhibits outstanding photocatalysis activity compared with pure TiO$_2$ under simulated sunlight. We further proposed that besides the above three advantages of Ag, different sizes of Ag nanoparticles are also responsible for the improved photocatalysis ability, where small−sized Ag nanoparticles (2~5 nm) could store photoexcited electrons that

generated from TiO_2, while large−sized Ag nanoparticles could utilize visible light due to their localized surface plasmon resonance (LSPR) absorption. Our work gives a new insight into the photocatalysis mechanism of noble metal/r−GO/TiO_2 composites and provides a new pathway into the design of TiO_2−based photocatalysts and promote their practical application in various environmental and energy issues.
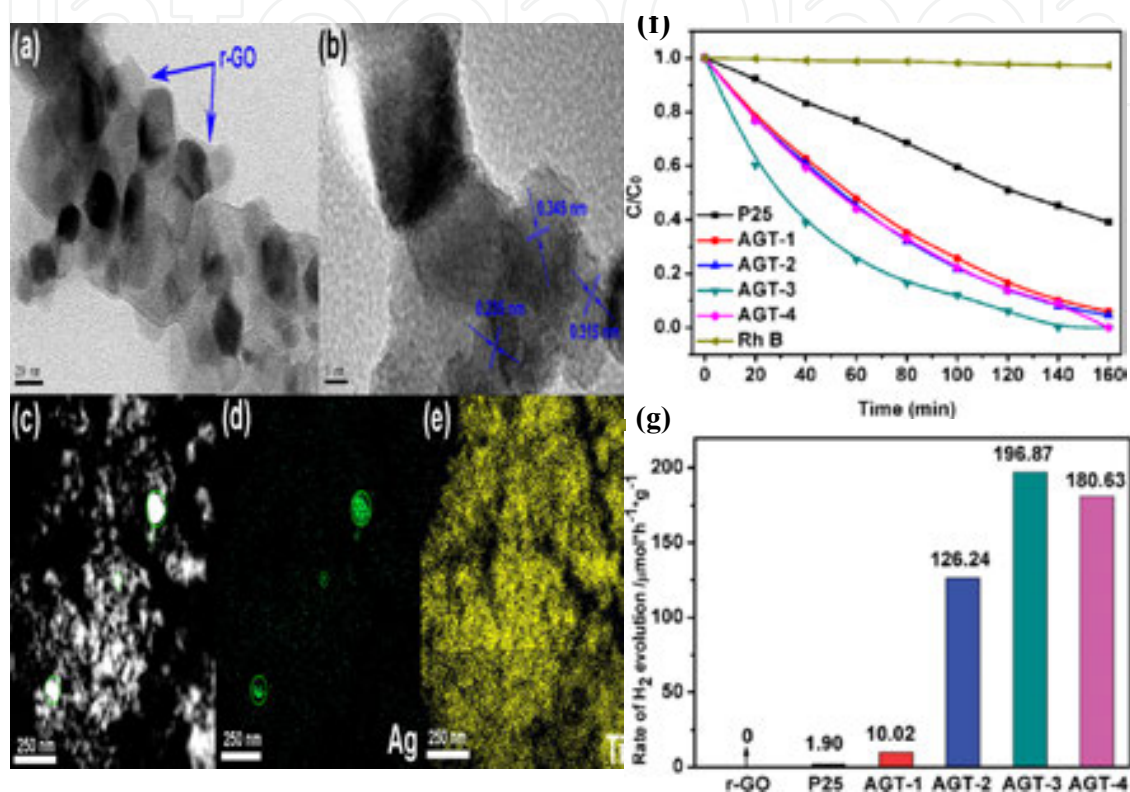

Figure 36. (a) TEM and (b) HRTEM images of sample AGT. (c) STEM model of Ag/r−GO/TiO_2. Elemental mapping of (d) Ag and (e) Ti in the same area in (c). (f)Photocatalytic degradation of Rh B under simulated sunlight irradiation over P25, Ag/r−GO/TiO_2 composites with different $AgNO_3$ contents. (g) Comparison of the photocatalytic activity of r −GO, P25 and Ag/r−GO/TiO_2 composites with different $AgNO_3$ contents for the photocatalytic H_2 production under simulated sunlight irradiation [367].

Next, we have replaced the Ag with MoS_2 quantum dots (QDs) and demonstrated a simple and an efficient one−pot approach to prepare MoS_2 quantum dots−graphene−TiO_2 (MGT) composites using a solvothermal method under obtained atmospheric pressures and at low temperatures (Fig. 37) [368]. The shape of MoS_2 obtained using this method is quantum dot instead of a layered sheet because of the interaction between functional groups on GO sheets and Mo precursors in a suitable solvent environment. In addition, it shows significantly increased photodegradation performance even without a noble-metal cocatalyst, which is due to the increased charge separation, visible-light absorbance, specific surface area and reaction sites upon the introduction of MoS_2 QDs. Besides, the enhancement mainly came from holes left in the TiO_2 crystals rather than electrons transferring to reduced graphene oxide (RGO).
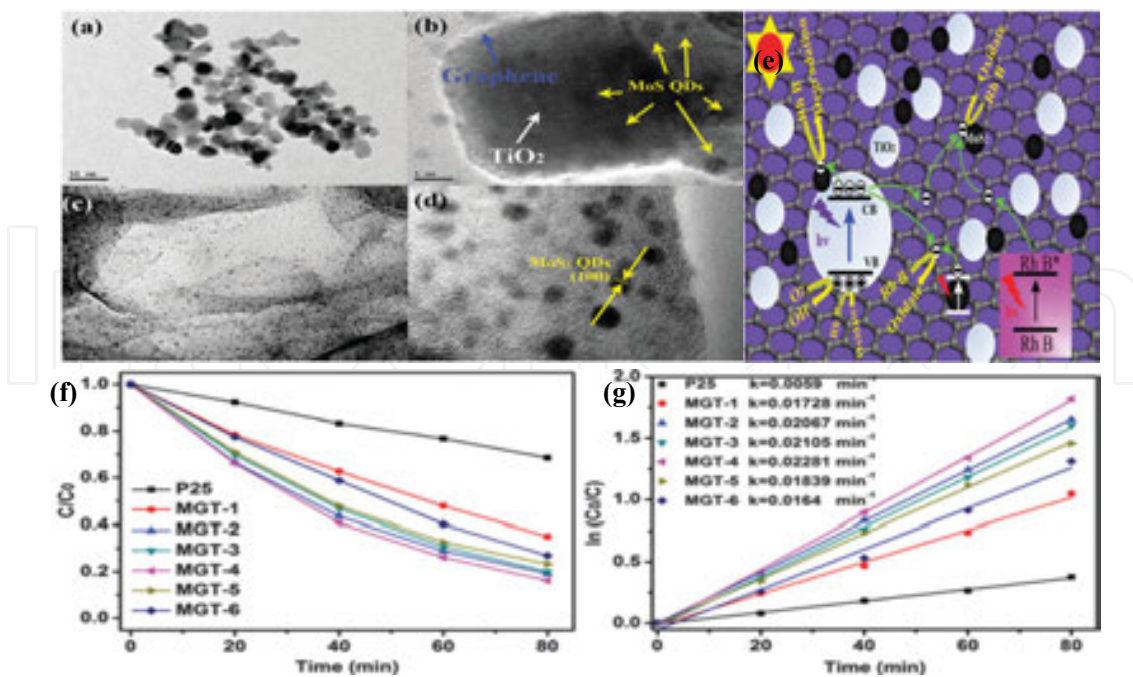
Figure 37. TEM and HRTEM images of the sample (a), (b) MGT−4 and (c), (d)MoS$_2$–graphene. (e) Proposed mechanism for the photodegradation of RhB by MGT under simulated sunlight irradiation (f) Photocatalytic degradation and (g) photocatalytic degradation reaction of RhB under simulated sunlight irradiation over P25, MGT composites with different MoS$_2$ contents [368].

5. Summary and outlook

Photocatalysis appears to be a promising avenue to solve environmental and energy issues in the future. Although the photocatalytic processes involve a complicated sequence of multiple synergistic or competing steps, the efficient utilization of solar energy (especial visible-light energy) and improvement in separation and transportation of charge carriers are the main challenges and current trend to design highly effective photocatalysts. Finally, we conclude that this chapter, after discussing with various materials and its composites for photocatalytic process, may be useful for further applications in the area of energy and environment. In summary, we have discussed the general strategies and recent progress in photocatalysis for developing highly efficient and stable photocatalysts, including: (1) Titania (TiO$_2$), iron oxides (α-Fe$_2$O$_3$); (2) ternary oxide photocatalytic matericals, such as Bi systems photocatalytic materials and (3) semiconducting materials and its composites. The achieved progress in photocatalysis indicates a promising route to enhance the photocatalytic efficiencies of photocatalytic semiconductors.

To date, in addition to different kinds of semiconductor materials and its composites significant advances have been reported to improve the photocatalytic efficiencies that range from environmental remediation to clean−energy harvesting by enhancing the utilization of sunlight or improving the separation/transportation of the electron−hole pairs some examples

are highlighted in this chapter. Extending light-response to the visible− or even infrared regions, decreasing the amount of recombination of electrons and holes, and increasing the light−harvesting efficiency have been the major tools that have led to such advances. Although great advancements have been made in investigation of heterostructured photocatalytsts, it is still challenging to design more challenges in high efficiency of photocatalytic systems. First, there is no detailed understanding of the charge generation, separation and transportation across nanoscale interfaces of heterostructured photocatalysts, which are critical for the design and optimization of highly more-efficient and more-reliable photocatalysts. Second, while most available photocatalysts so far can only function in the UV or near−UV regime, the highly effective utilization of visible light is another challenge of heterostructured photocatalysts. Third, photostability of heterostructured photocatalyst is and will still be a major challenge for practical applications. Finally, elucidating and understanding the mechanisms that are involved in various photocatalytic reactions. Therefore, the deepening knowledge of the photocatalytic mechanism and exploration of new materials are indispensible to make substantial breakthroughs for practical application of photocatalysts.

Author details

Le Li and Minqiang Wang[*]

*Address all correspondence to: mqwang@mail.xjtu.edu.cn

Electronic Materials Research Laboratory (EMRL), Key Laboratory of Education Ministry, International Center for Dielectric Research, Xi'an Jiaotong University, Xi'an, China

References

[1] M. R. Hoffmann, S. T. Martin, W. Y. Choi, D. W. Bahnemann, Chem Rev. 1995, 95, 69−96.

[2] A. Kudo, Y. Miseki, Chem. Soc. Rev. 2009, 38, 253−278.

[3] X. Li, J. Q. Wen, J. X. Low, Y. P. Fang, J. G. Yu, Sci. China Mater. 2014, 57,70−100.

[4] Y. Q. Qu, X. F. Duan, Chem. Soc. Rev. 2013, 42, 2568−2580.

[5] H. Tong, S. Ouyang, Y. Bi, N. Umezawa, M. Oshikiri, J. Ye, Adv. Mater. 2012, 24, 229−251.

[6] M. G. Kibria, H. P. T. Nguyen, K. Cui, S. Zhao, D. Liu, H. Guo, M. L.Trudeau, S. Paradis, A. R. Hakima, Z. Mi, ACS Nano. 2013, 7,7886−7893.

[7] Q. J. Xiang, J. G. Yu, M. Jaroniec, J. Am. Chem. Soc. 2012, 134, 6575−6578.

[8] J. A. Christians, R. C. M. Fung, P. V. Kamat, J. Am. Chem. Soc. 2014,136, 758–764.

[9] Q. Zhang, E. Uchaker, S. L. Candelaria, G. Cao, Chem. Soc. Rev. 2013, 42, 3127–3171.

[10] J. G. Yu, X. X. Yu, Environ. Sci. Technol. 2008, 42, 4902–4907.

[11] J. Kim, J. Lee, W. Choi, Chem. Commun. 2008, 756–761.

[12] Y. Bi, S. Ouyang, N. Umezawa, J. Cao, J. Ye, J. Am. Chem. Soc. 2011,133, 6490–6492.

[13] E. V. Kondratenko, G. Mul, J. Baltrusaitis, G. O. Larrazábal, J. Pérez-Ramírez, Energy Environ. Sci. 2013, 6, 3112–3135.

[14] S. C. Roy, O. K. Varghese, M. Paulose, C. A. Grimes, ACS Nano 2010, 4, 1259–1278.

[15] A. Dhakshinamoorthy, S. Navalon, A. Corma, H. Garcia, Energy Environ. Sci. 2012, 5, 9217–9233.

[16] P Zhou, J G Yu, M Jaroniec, Adv. Mater. 2014, 26, 4920–4935.

[17] E. Fujita, J. T. Muckerman, K. Domen, ChemSusChem. 2011, 4, 155–157.

[18] S. Linic, P. Christopher, D. B. Ingram, Nat. Mater. 2011, 10, 911–921.

[19] C. Li, F. Wang, J. C. Yu, Energy Environ. Sci. 2011, 4, 100–113.

[20] H. Zhou, Y. Qu, T. Zeid, X. Duan, Energy Environ. Sci. 2012, 5, 6732–6743.

[21] Q. Li, X. Li, S. Wageh, A. Al-Ghamdi, J. G. Yu, Adv. Energy. Mater. 2015, 17, 10010–10039.

[22] J. M. Elward, A. Chakraborty, J. Chem. Theory Comput. 2013, 9, 4351–4357.

[23] F. L. Formal, S. R. Pendlebury, M. Cornuz, S. D. Tilley, M. Grä tzel, J. R. Durrant, J. Am. Chem. Soc. 2014, 136, 2564–2574.

[24] P. Zhou, J. G. Yu, M. Jaroniec, Adv. Mater. 2014, 26, 4920–4935.

[25] L. L. Tan, S. P. Chai, A. R. Mohamed, Chemsuschem. 2012, 5,1868–1882.

[26] L. Sun, Z. L. Zhao, Y. C. Zhou, L. Liu, Nanoscale. 2012, 4, 613–620.

[27] Q. J. Xiang, J. G. Yu, M. Jaroniec, Chem. Soc. Rev. 2012, 41, 782–796.

[28] M. R. Hoffmann, S. T. Martin, W. Y. Choi, D. W. Bahnemann, Chem. Rev. 1995, 95, 69–96.

[29] O. Carp, C. L. Huisman, A. Reller, Prog. Solid State Chem. 2004, 32, 33–177.

[30] D. Dambournet, I. Belharouak, K. Amine, Chem. Mater. 2010, 22, 1173–1179.

[31] U. Diebold, Surf. Sci. Rep. 2003, 48, 53–229.

[32] O. Carp, C. L. Huisman, A. Reller, Prog. Solid State Chem. 2004, 32, 33–177.

[33] M. A. Fox, M. T. Dulay, Chem. Rev. 1993, 93, 341–357.

[34] A. Fujishima, T. N. Rao, D. A. Tryk, J. Photochem. Photobiol. C. 2000, 1, 1–21.

[35] U. Diebold, N. Ruzycki, G. S. Herman, A. Selloni, Catal.Today. 2003, 85, 93–100.

[36] A. S. Barnard, H. Xu, ACS Nano. 2008, 2, 2237–2242.

[37] J. K. Burdett, T. Hughbands, J. M. Gordon, J. W. Richarson, J. Smith, J. Am. Chem. Soc. 1987, 109, 3639–3646.

[38] R. Asahi, Y. Taga, Y. Mannstadt, A. Freeman, J. Phys. Rev. B. 2000, 61, 7459–7467.

[39] C. Sousa, F. Illas, J. Chem. Phys. 1994, 50, 13974–13983.

[40] A. Kubacka, M. Fernández-García, G Colón, Chem. Rev. 2012, 112, 1555–1614.

[41] A. Fujishima, K. Honda, Nature. 1972, 238, 37–41.

[42] A. L. Linsebigler, G. Lu, J. T. Yates, Chem. Rev. 1995, 95, 735–758.

[43] A. Fujishima, T. N. Rao, D. A. Tryk, J. Photochem. Photobiol. C: Photochem. Rev. 2000, 1, 1–21.

[44] K. Hashimoto, H. Irie, A. Fujishima, Jpn. J. Appl. Phys. 2005, 44, 8269–8285.

[45] U. I. Gaya, A. H. Abdullah, J. Photochem. Photobiol. C: Photochem. Rev. 2008, 9, 1–12.

[46] D. P. Macwan, P. N. Dave, S. Chaturvedi, J. Mater. Sci. 2011, 46, 3669–3686.

[47] X. Guan, J. Du, X. Meng, Y. Sun, B. Sun, Q. Hu, J. Hazard. Mater. 2012, 1, 215–216.

[48] M. D. Hernández-Alonso, F. Fresno, S. Suárez, J. M. Coronado, Energy Environ. Sci. 2009, 2, 1231–1257.

[49] W. Zhou, H. Liu, R. I. Boughton, G. Du, J. Lin, J. Wang, D. Liu, J. Mater. Chem. 2010, 20, 5993–6008.

[50] G. Liu, L. Wang, H. G. Yang, H. M. Cheng, G. Q. Lu, J. Mater. Chem. 2010, 20, 831–843.

[51] S. G. Kumar, L. G. Devi, J. Phys. Chem. A. 2011, 115, 13211–13241.

[52] A. A. Ismail, D. W. Bahnemann, J. Mater. Chem. 2011, 21, 11686–11707.

[53] R. Leary, A. Westwood, Carbon. 2011, 49, 741–772.

[54] A. Primo, A. Corma, H. García, Phys. Chem. Chem. Phys. 2011, 13, 886–910.

[55] A. S. Weber, A. M. Grady, R. T. Koodali, Catal. Sci. Technol. 2012, 2, 683–693.

[56] R. Asahi, T. Morikawa, T. Ohwaki, K. Aoki, Y. Taga, Science. 2001, 293, 269–271.

[57] C. Burda, Y. B. Lou, X. B. Chen, A. C. S. Samia, J. Stout, J. L. Gole, Nano Lett. 2003, 3,1049–1051.

[58] S. U. M. Khan, M. Al. Shahry, W. B. Ingler, Science, 2002, 297, 2243–2245.

[59] C. Di Valentin, G. Pacchioni, A. Selloni, Chem. Mater. 2005,17, 6656–6665.

[60] S. Sakthivel, H. Kisch, Angew. Chem. Int. Ed. 2003, 42, 4908–4911.

[61] T. Umebayashi, T. Yamaki, H. Itoh, K. Asai, Appl. Phys. Lett. 2002, 81, 454–456.

[62] W. K. Ho, J. C. Yu, S. C. Lee, J. Solid State Chem. 2006,179, 1171–1176.

[63] W. Zhao, W. H. Ma, C. C. Chen, J. C. Zhao, Z. G. Shuai, J. Am.Chem. Soc. 2004, 126, 4782–4783.

[64] G. Liu, Y. N. Zhao, C. H. Sun, F. Li, G. Q. Lu, H. M. Cheng, Angew. Chem. Int. Ed. 2008, 47, 4516–4520.

[65] S. In, A. Orlov, R. Berg, F. Garcia, S. Pedrosa-Jimenez, M. S. Tikhov, D. S. Wright, R. M. Lambert, J. Am. Chem. Soc. 2007, 129, 13790–13791.

[66] J. G. Yu, W. K. Ho, Z. T. Jiang, L. Z. Zhang, Chem. Mater. 2002, 14, 3808–3816.

[67] D. Li, H. Haneda, N. K. Labhsetwar, S. Hishita, N. Ohashi, Chem. Phys. Lett. 2005, 401, 579–584.

[68] C. Di Valentin, E. Finazzi, G. Pacchioni, A. Selloni, S. Livraghi, A. M. Czoska, M. C. Paganini, E. Giamello, Chem. Mater. 2008, 20, 3706–3714.

[69] H. M. Luo, T. Takata, Y. G. Lee, J. F. Zhao, K. Domen, Y. S. Yan, Chem. Mater. 2004, 16, 846–849.

[70] X. T. Hong, Z. P. Wang, W. M. Cai, F. Lu, J. Zhang, Y. Z. Yang, N. Ma, Y. J. Liu, Chem. Mater. 2005, 17, 1548–1552.

[71] G. Liu, Z. G. Chen, C. L. Dong, Y. N. Zhao, F. Li, G. Q. Lu, H. M. Cheng, J. Phys. Chem. B. 2006, 110, 20823–20828.

[72] W. Y. Su, Y. F. Zhang, Z. H. Li, L. Wu, X. X. Wang, J. Q. Li, X. Z. Fu, Langmuir. 2008, 24, 3422–3428.

[73] S. Tojo, T. Tachikawa, M. Fujitsuka, T. Majima, J. Phys. Chem. C. 2008, 112, 14948–14954.

[74] L. Lin, W. Lin, Y. X. Zhu, B. Y. Zhao, Y. C. Xie, Chem. Lett. 2005, 34, 284–285.

[75] G. Liu, L. Z. Wang, H. G. Yang, H. M. Cheng, G. Q. Lu, J. Mater. Chem. 2010, 20, 831–843.

[76] M. Lazzeri, A. Vittadini, A. Selloni, Phys. Rev. B: Condens. Matter. 2001, 63, 155409–155412.

[77] M. Lazzeri, A. Vittadini, A. Selloni, Phys. Rev. B: Condens. Matter. 2002, 65, 119901–119908.

[78] M. Ramamoorthy, D. Vanderbilt, R. D. Kingsmith, Phys. Rev. B. 1994, 49, 1672−1679.

[79] X. Q. Gong, A. Selloni, Phys. Rev. B: Condens. Matter Mater. Phys. 2007, 76, 235307−235313.

[80] G. Liu, J. C. Yu, G. Q. Lu, H. M. Cheng, Chem. Commun. 2011, 47, 6763−6783.

[81] J. Jiang, K. Zhao, X. Xiao, L. Zhang, J. Am. Chem. Soc. 2012, 134, 4473−4476.

[82] H. G. Yang, C. H. Sun, S. Z. Qiao, J. Zou, G. Liu, S. C. Smith, H. M. Cheng, G. Q. Lu, Nature, 2008, 453, 638−641.

[83] M. D'Arienzo, J. Carbajo, A. Bahamonde, M. Crippa, S. Polizzi, R. Scotti, L. Wahba, F. Morazzoni, J. Am. Chem. Soc. 2011, 133, 17652−17661.

[84] X. G. Han, Q. Kuang, M. S. Jin, Z. X. Xie, L. S. Zheng, J. Am. Chem. Soc. 2009, 131, 3152−3153.

[85] H. G. Yang, G. Liu, S. Z. Qiao, C. H. Sun, Y. G. Jin, S. C. Smith, J. Zou, H. M. Cheng, G. Q. Lu, J. Am. Chem. Soc. 2009, 131, 4078−4083.

[86] D. Zhang, G. Li, X. Yang, J. C. Yu, Chem. Commun. 2009, 27, 4381−4383.

[87] J. Zhu, S. H. Wang, Z. F. Bian, S. H. Xie, C. L. Cai, J. G. Wang, H. G. Yang, H. X. Li, CrystEngComm. 2010, 12, 2219−2224.

[88] D. Q. Zhang, G. S. Li, H. B. Wang, K. M. Chan, J. C. Yu, Cryst. Growth Des. 2010, 10, 1130−1137.

[89] F. Amano, O. O. Prieto-Mahaney, Y. Terada, T. Yasumoto, T. Shibayama, B. Ohtani, Chem. Mater. 2009, 21, 2601−2603.

[90] J. S. Chen, Y. L. Tan, C. M. Li, Y. L. Cheah, D. Y. Luan, S. Madhavi, F. Y. C. Boey, L. A. Archer, X. W. Lou, J. Am. Chem. Soc. 2010, 132, 6124−6130.

[91] M. Liu, L. Y. Piao, W. M. Lu, S. T. Ju, L. Zhao, C. L. Zhou, H. L. Li, W. J. Wang, Nanoscale. 2010, 2, 1115−1117.

[92] X. H. Yang, Z. Li, G. Liu, J. Xing, C. H. Sun, H. G. Yang, C. Z. Li, CrystEngComm. 2011, 13, 1378−1383.

[93] X. N. Wang, B. B. Huang, Z. Y. Wang, X. Y. Qin, X. Y. Zhang, Y. Dai, M. H. Whangbo, Chem. Eur. J. 2010, 16, 7106−7109.

[94] X. Y. Ma, Z. G. Chen, S. B. Hartono, H. B. Jiang, J. Zou, S. Z. Qiao, H. G. Yang, Chem. Commun. 2010, 46, 6608−6610.

[95] S. W. Liu, J. G. Yu, M. Jaroniec, J. Am. Chem. Soc. 2010, 132,11914−11916.

[96] M. Liu, L. Piao, L. Zhao, S. Ju, Z. Yan, T. He, C. Zhou, W. Wang, Chem. Commun. 2010, 46, 1664−1666.

[97]   G. Liu, C. H. Sun, H. G. Yang, S. C. Smith, L. Z. Wang, G. Q. Lu, H. M. Cheng, Chem. Commun. 2010, 46, 755–757.

[98]   Z. K. Zheng, B. B. Huang, X. Y. Qin, X. Y. Zhang, Y. Dai, M. H. Jiang, P. Wang, M. H. Whangbo, Chem. Eur. J. 2009, 15, 12576–12579.

[99]   Y. Q. Dai, C. M. Cobley, J. Zeng, Y. M. Sun, Y. N. Xia, Nano Lett. 2009, 9, 2455–2459.

[100] J. M. Li, D. S. Xu, Chem. Commun. 2010, 46, 2301–2303.

[101] M. D'Arienzo, J. Carbajo, A. Bahamonde, M. Crippa, S. Polizzi, R. Scotti, L. Wahba, F. Morazzoni, J. Am. Chem. Soc. 2011, 133, 17652–17661.

[102] T. Tachikawa, S. Yamashita, T. Majima, J. Am. Chem. Soc. 2011, 133, 7197–7204.

[103] J. Pan, G. Liu, G. Q. Lu, H. M. Cheng, Angew. Chem. Int. Ed. 2011, 50, 2133–2137.

[104] T. R. Gordon, M. Cargnello, T. Paik, F. Mangolini, R. T. Weber, P. Fornasiero, C. B. Murray, J. Am. Chem.Soc. 2012, 134, 6751–6761.

[105] H. Xu, P. Reunchan, S. Ouyang, H. Tong, N. Umezawa, T. Kako, J. Ye, Chem. Mater. 2013, 25, 405–411.

[106] J. Yu, J. Low, W. Xiao, P. Zhou, M. Jaroniec, J. Am. Chem. Soc. 2014, 136, 8839–8842.

[107] S. Liu, J. Yu, M. Jaroniec, Chem. Mater. 2011, 23, 4085–4093.

[108] T. Tachikawa, S. Yamashita, T. Majima, J. Am. Chem. Soc. 2011,133, 7197–7204.

[109] H. B. Jiang, Q. A. Cuan, C. Z. Wen, J. Xing, D. Wu, X. Q. Gong, C. Z. Li, H. G. Yang, Angew. Chem. 2011, 123, 3848–3852.

[110] J. Zhang, Q. Xu, M. J. Li, Z. C. Feng, C. Li, J. Phys. Chem. C. 2009, 113, 1698–1704.

[111] G. Liu, F. Li, Z. G. Chen, G. Q. Lu, H. M. Cheng, J. Solid State Chem. 2006, 179, 331–335.

[112] X. Chen, S. S. Mao, Chem. Rev. 2007, 107, 2891–2959.

[113] J. M. Wu, H. C. Shih, W. T. W, Nanotechnology, 2006, 17,105–113.

[114] C. R. Xiong, X. Y. Deng, J. B. Li, Appl. Catal. B. 2010, 94,234–240.

[115] D. Q. Zhang, G. S. Li, F. Wang, J. C. Yu, CrystEngComm, 2010, 12, 1759-1763.

[116] K. Kakiuchi, E. Hosono, H. Imai, T. Kimura, S. Fujihara, J. Cryst. Growth, 2006, 293, 541–545.

[117] X. F. Yang, J. Chen, L. Gong, M. M. Wu, J. C. Yu, J. Am. Chem. Soc. 2009, 131, 12048–12049.

[118] Y. W. Wang, L. Z. Zhang, K. J. Deng, X. Y. Chen, Z. G. Zou, J. Phys. Chem. C, 2007, 111, 2709–2714.

[119] H. M. Cheng, J. M. Ma, Z. G. Zhao, L. M. Qi, Chem. Mater. 1995, 7, 663–671.

[120] Y. Sang, B. Y. Geng, J. Yang, Nanoscale. 2010, 2, 2109–2113.

[121] B. Liu, E. S. Aydil, J. Am. Chem. Soc. 2009, 131, 3985–3390.

[122] T. Y. Ke, C. W. Peng, C. Y. Lee, H. T. Chiu, H. S. Sheu, CrystEngComm, 2009, 11, 1691–1695.

[123] E. Bae, T. Ohno, Appl. Catal. B: Environ. 2009, 91, 634–639.

[124] J. Yu, Y. Chen, A. M. Glushenkov, Cryst. Growth Des. 2009, 9, 1240–1244.

[125] F. Y. Wei, H. L. Zeng, P. Cui, S. C. Peng, T. H. Cheng, Chem. Eng. J. 2008, 144, 119–123.

[126] H. Kaper, F. Endres, I. Djerdj, M. Antonietti, B. M. Smarsly, J. Maier, Y. S. Hu, Small. 2007, 3, 1753–1763.

[127] H. Xu, F. L. Jia, Z. H. Ai, L. Z. Zhang, Cryst. Growth Des. 2007, 7, 1216–1219.

[128] A. Dessombz, D. Chiche, P. Davidson, P. Panine, C. Chaneac, J. P. Jolivet, J. Am. Chem. Soc. 2007, 129, 5904–5909.

[129] M. N. Tahir, P. Theato, P. Oberle, G. Melnyk, S. Faiss, U. Kolb, A. Janshoff, M. Stepputat, W. Tremel, Langmuir. 2006, 22, 5209–5912.

[130] B. Zhao, F. Chen, Q. W. Huang, J. L. Zhang, Chem. Commun. 2009, 34, 5115–5117.

[131] M. Addamo, V. Augugliaro, M. Bellardita, A. Di Paola, V. Loddo, G. Palmisano, L. Palmisano, S. Yurdakal, Catal. Lett. 2008, 126, 58–62.

[132] F. Iskandar, A. B. D. Nandiyanto, K. M. Yun, C. J. Hogan, K. Okuyama, P. Biswas, Adv. Mater. 2007, 19, 1408–1412.

[133] J. G. Li, C. C. Tang, D. Li, H. Haneda, T. Ishigaki, J. Am. Ceram. Soc. 2004, 87, 1358–1361.

[134] R. Buonsanti, V. Grillo, E. Carlino, C. Giannini, T. Kipp, R. Cingolani, P. D. Cozzoli, J. Am. Chem. Soc. 2008, 130, 11223–11233.

[135] R. M. Cornell, U. Schwertmann, The Iron Oxides: Structure, Properties, Reactions, Occurrences, and Uses, 2nd Ed. Wiley-VCH, Weinheim, 2003.

[136] K Sivula, F Le Formal, M Grätzel, ChemSusChem 2011, 4, 432–449.

[137] K. Sivula, R. Zboril, F. Le Formal, R. Robert, A. Weidenkaff, J. Tucek, J. Frydrych, M. Gra°tzel, J. Am. Chem. Soc. 2010, 132, 7436–7444.

[138] A.I. Galuza, A.B. Beznosov, V.V. Eremenko, Low Temp. Phys. 1998, 24, 726–729.

[139] J.H. Kennedy, K.W. Frese, J. Electrochem. Soc. 1978, 125, 709–714.

[140] L.A. Marusak, R. Messier, W.B. White, J. Phys. Chem. Solids. 1980, 41, 981–984.

[141] N.C. Debnath, A.B. Anderson, J. Electrochem. Soc. 1982, 129, 2169–2174.

[142] B. Wang, J.S. Chen, H.B. Wu, Z.Y. Wang, X.W. Liu, J. Am. Chem. Soc. 2011, 133, 17146–17148.

[143] J. Chen, L. Xu, W. Li, X. Gou, Adv. Mater. 2005, 17, 582–586.

[144] Z. Sun, H. Yuan, Z. Liu, B. Han, X. Zhang, Adv. Mater. 2005, 17, 2993–2997.

[145] X. Hu, J.C. Yu, J. Gong, Q. Li, G. Li, Adv. Mater. 2007, 19, 2324–2329.

[146] J. Yu, X. Yu, B. Huang, X. Zhang, Y. Dai, Cryst. Growth Res. 2009, 9, 1474–1480.

[147] G. Liu, Q. Deng, H. Wang, D.H.L. Ng, M. Kong, W. Cai, G. Wang, J. Mater. Chem. 2012, 22, 9704–9713.

[148] C.Y. Cao, J. Qu, W.S. Yan, J.F. Zhu, Z.Y. Wu, W.G. Song, Langmuir 2012, 28, 4573–4579.

[149] K. Sivula, F. Le Formal, M. Gratzel, Chem. Sus. Chem. 2011, 4, 432–449.

[150] Z. Chen, T.F. Jaramillo, T.G. Deutsch, A. Kleiman-Shwarsctein, A.J. Forman, N.Gaillard, R. Garland, K. Takanabe, C. Heske, M. Sunkara, E.W. McFarland, K.Domen, E.L. Miller, J.A. Turner, H.N. Dinh, J. Mater. Res. 2010, 25, 3–16.

[151] J. Brillet, M. Cornuz, F. Le Formal, J.-H. Yum, M. Grätzel, K. Sivula, J. Mater. Res. 2010, 25, 17–24.

[152] C.J. Sartoretti, M. Ulmann, B.D. Alexander, J. Augustynski, A. Weidenkaff, Chem. Phys. Lett. 2003, 376, 194–200.

[153] J.H. Kennedy, J.K.W. Frese, J. Electrochem. Soc. 1978, 125, 709–714.

[154] F.J. Morin, Phys. Rev. 1951, 83, 1005–1010.

[155] F.J. Morin, Phys. Rev. 1954, 93, 1195–1199.

[156] M.P. Dare-Edwards, J.B. Goodenough, A. Hamnett, P.R. Trevellick, J. Chem. Soc.Faraday Trans. 1983, 79, 2027–2041.

[157] K. Sivula, F.L. Formal, M. Grätzel, Chem. Sus. Chem. 2011, 4, 432–449.

[158] M.J. Katz, S.C. Riha, N.C. Jeong, A.B.F. Martinson, O.K. Farha, J.T. Hupp, Coord.Chem. Rev. 2012, 256, 2521–2529.

[159] T.K. Townsend, E.M. Sabio, N.D. Browning, F.E. Osterloh, Energy Environ. Sci. 2011, 4, 4270–4275.

[160] S.N. Dang, S.X. Lu, W.G. Xu, J. Sa, J. Non-Cryst. Solids 2008, 354, 5018–5021.

[161] M.A. Valenzuela, P. Bosch, J. Jiménez-Becerrill, O. Quiroz, A.I. Páez, J. Pho-tochem. Photobiol. A 2002, 148, 177–182.

[162] G. Zhang, Y. Feng, Y. Xu, D. Gao, Y. Sun, Mater. Res. Bull. 2012, 47, 625–630.

[163]   L. Li, Y. Chu, Y. Liu, L. Dong, J. Phys. Chem. C. 2007, 111, 2123–2127.

[164]   X. Li, X. Yu, J. He, Z. Xu, J. Phys. Chem. C. 2009, 113, 2837–2845.

[165]   S. Cao, Y. Zhu, Nanoscale Res. Lett. 2011, 6, 27–36.

[166]   J. Xu, Y. Zhu, Cryst. Eng. Comm. 2011, 13, 5162–5169.

[167]   L. Xu, J. Xia, K. Wang, L. Wang, H. Li, H. Xu, L. Huang, M. He, Dalton Trans. 2013, 42, 6468–6477.

[168]   S.K. Maji, N. Mukherjee, A. Mondal, B. Adhikary, Polyhedron 2012, 33,145–149.

[169]   S.K. Apte, S.D. Naik, R.S. Sonawane, B.B. Kale, J. Am. Ceram. Soc. 2007, 90, 412–414.

[170]   S. Bharathi, D. Nataraj, K. Senthil, Y. Masuda, J. Nanopart. Res. 2013, 15, 1346–1352.

[171]   A. Hosseinian, H. Rezaei, A.R. Mahjoub, World Acad. Sci. Eng. Technol. 2011, 52, 4–21.

[172]   C.T. Seip, C. Connor, Nanostruct. Mater. 1999, 12, 183–188.

[173]   S. Yang, Y. Xu, Y. Sun, G. Zhang, D. Gao, Cryst. Eng. Comm. 2012, 14, 7915–7921.

[174]   X. Zhou, H. Yang, C. Wang, X. Mao, Y. Wang, Y. Yang, G. Liu, J. Phys. Chem. C. 2010, 114, 17051–17061.

[175]   M.J. Pawar, A.D. Khajone, M.D. Gaoner, P.S. Chandel, Int. J. Adv. Sci. Res. Tech-nol. 2012, 2, 471–476.

[176]   Y. Liu, H. Yu, S. Zhan, Y. Li, Z. Lv, X. Yang, Y. Yu, J. Sol-Gel Sci. Technol. 2011, 58, 716–723.

[177]   J. Sundaramurthy, P.S. Kumar, M. Kalaivani, V. Thavasi, S.G. Mhaisalkar, RSC Adv. 2012, 2, 8201–8208.

[178]   B. Geng, B. Tao, X. Li, W. Wei, Nanoscale 2012, 4, 1671–1676.

[179]   Y. Xu, G. Zhang, G. Du, Y. Sun, D. Gao, Mater. Lett. 2013, 92, 321–324.

[180]   H. Zhou, S.S. Wong, ACS Nano 2008, 2, 944–958.

[181]   X. Cheng, J. Jiang, M. Hu, G. Mao, F. Bu, C. Lin, Y. Zeng, Q. Zhang, Cryst. Eng.Comm. 2012, 14, 7701–7708.

[182]   Y. Mao, S.S. Wong, J. Am. Chem. Soc. 2006, 128, 8217–8226.

[183]   J. Bandara, U. Klehm, J. Kiwi, Appl. Catal. B. 2007, 76, 73–81.

[184]   S. Cao, Y. Zh, G. Cheng, Y. Huang, J. Phys. Chem. Solids. 2010, 71, 1680–1683.

[185]   W. Wu, R. Hao, F. Liu, X. Su, Y. Hou, J. Mater. Chem. A. 2013, 1, 6888–6894.

[186]   W. Du, Q. Sun, X. Lv, Y. Xu, Catal. Commun. 2009, 10, 1854–1858.

[187] B. Lv, Z. Liu, H. Tian, Y. Xu, D. Wu, Y. Sun, Adv. Funct. Mater. 2010, 20, 3987–3996.

[188] A.B. Isaev, Z.M. Aliev, N.K. Adamadzieva, N.A. Alieva, G.A. Magomedova, Nanotechnol. Russia. 2009, 4, 475–479.

[189] Zhou X, Lan J, Liu G, Deng K, Yang Y, Nie G, Yu J, Zhi L, Angew Chem Int Ed. 2012, 51, 178–182.

[190] J. D. Bierlein, A. W. Sleight, Solid State Commun. 1975,16, 69–76.

[191] R. S. Roth, J. L. Waring, Am. Mineral. 1963, 48, 1348–1356.

[192] Y Park, KJ McDonald, KS Choi, Chem. Soc. Rev. 2013, 42, 2321–2337.

[193] A. W. Sleight, H.-y. Chen, A. Ferretti, D. E. Cox, Mater. Res. Bull. 1979, 14, 1571–1577.

[194] G. Dreyer, E. Tillmanns, Neues Jahrb. Mineral. Monatsh.e, 1981, 81, 151–156.

[195] Y Park, K J. McDonald, Kyoung-Shin Choi, Chem. Soc. Rev. 2013, 42, 2321–2337.

[196] A. K. Bhattacharya, K. K. Mallick, A. Hartridge, Mater. Lett. 1997, 30, 7-10.

[197] A. Kudo, K. Omori, H. Kato, J. Am. Chem. Soc. 1999, 121, 11459–11461.

[198] S. Tokunaga, H. Kato, A. Kudo, Chem. Mater. 2001, 13, 4624–4628.

[199] H. Tong, S. Ouyang, Y. Bi, N. Umezawa, M. Oshikiri, J. Ye, Adv. Mater. 2012, 24, 229–251.

[200] H. L. Zhou, Y. Q. Qu, T. Zeid, X. F. Duan, Energy Environ. Sci. 2012, 5, 6732–6743.

[201] Y. Ma, X. Wang, Y. Jia, X. Chen, H. Han, C. Li, Chem. Rev. 2014, 114, 9987–10043.

[202] A. Kubacka, M. Fernandez-Garcia, G. Colon, Chem. Rev. 2011, 112, 1555–1614.

[203] S.-i. Eda, M. Fujishima, H. Tada, Appl. Catal. B. 2012, 125, 288–293.

[204] H. He, S. P. Berglund, A. J. E. Rettie, W. D. Chemelewski, P. Xiao, Y. Zhang, C. B. Mullins, J. Mater. Chem. A, 2014, 2, 9371–9379.

[205] W. Wang, Y. Yu, T. An, G. Li, H. Y. Yip, J. C. Yu, P. K. Wong, Environ. Sci. Technol. 2012, 46, 4599–4606.

[206] Y. Sun, Y. Xie, C. Wu, S. Zhang, S. Jiang, Nano Res. 2010, 3, 620–631.

[207] X. Chen, J. Liu, H. Wang, Y. Ding, Y. Sun, H. Yan, J. Mater. Chem. A. 2013, 1, 877–887.

[208] J. Sun, G. Chen, J. Wu, H. Dong, G. Xiong, Appl. Catal. B. 2013, 132, 304–314.

[209] Y. Sun, C. Wu, R. Long, Y. Cui, S. Zhang, Y. Xie, Chem. Commun. 2009, 30, 4542–4544.

[210] Y. Zhao, Y. Xie, X. Zhu, S. Yan, S. Wang, Chem. Eur. J. 2008, 14, 1601–1606.

[211] G. Li, D. Zhang, J. C. Yu, Chem. Mater. 2008, 20, 3983–3992.

[212] Y. Park, K. J. McDonald, K.-S. Choi, Chem. Soc. Rev. 2013, 42, 2321–2337.

[213] F. F. Abdi, N. Firet, R. van de Krol, ChemCatChem, 2013, 5, 490–496.

[214] K. J. McDonald, K.-S. Choi, Energy Environ. Sci. 2012, 5, 8553–8557.

[215] M. Zhou, H. B. Wu, J. Bao, L. Liang, X. W. Lou, Y. Xie, Angew. Chem. Int. Ed. 2013, 52, 8579–8583.

[216] E. S. Kwak, W. Lee, N.-G. Park, J. Kim, H. Lee, Adv. Funct. Mater. 2009, 19, 1093–1100.

[217] G. Liu, J. C. Yu, G. Q. Lu, H. M. Cheng, Chem. Commun. 2011, 47, 6763–6783.

[218] G. Xi, J. Ye, Chem. Commun. 2010, 46, 1893–1895.

[219] D. Wang, H. Jiang, X. Zong, Q. Xu, Y. Ma, G. Li, C. Li, Chem. Eur. J. 2011, 17, 1275–1282.

[220] J. Yang, D. Wang, X. Zhou, C. Li, Chem. Eur. J. 2013, 19, 1320–1326.

[221] J. Pan, G. Liu, G. Q. Lu, H. M. Cheng, Angew. Chem. Int. Ed. 2011, 50, 2133–2137.

[222] R. Li, F. Zhang, D. Wang, J. Yang, M. Li, J. Zhu, X. Zhou, H. Han, C. Li, Nat. Commun. 2013, 4, 1432–1437.

[223] R. Li, H. Han, F. Zhang, D. Wang, C. Li, Energy Environ. Sci. 2014, 7, 1369–1376.

[224] Y.Y. Li, J.P. Liu, X.T. Huang, Nanoscale Res. Lett. 2007, 3, 365–371.

[225] N. Kim, R.N. Vannier, C.P. Grey, Chem. Mater. 2005, 17, 1952–1958.

[226] L. Zhang, H. Wang, Z. Chen, P. K. Wong, J. Liu, Appl. Catal. B. 2011, 106, 1–13.

[227] S. H. Chen, Z. Yin, S. L. Luo, X. J. Li, L. X. Yang, F. Deng, Appl. Surf. Sci. 2012, 259, 7–12.

[228] A. Kudo, S. Hijii, Chem. Lett. 1999, 10, 1103–1104.

[229] J. Tang, Z. Zou, J. Ye, Catal. Lett. 2004, 92, 53–56.

[230] C. Zhang, Y. Zhu, Chem. Mater. 2005, 17, 3537–3545.

[231] N. Zhang, R. Ciriminna, M. Pagliaro, Y. J. Xu, Chem Soc Rev. 2014, 43, 5276–5287.

[232] A. Kudo, S. Hijii, Chem. Lett. 1999, 10, 1103–1104.

[233] G. K. Zhang, F. Lü, M. Li, J. L. Yang, X. Y. Zhang, B. B. Huang, J. Phys. Chem. Solids. 2010, 71, 579–582.

[234] Z. J. Zhang, W. Z. Wang, M. Shang, W. Z. Yin, J. Hazard. Mater. 2010, 177, 1013–1018.

[235] L. Zhou, W. Z. Wang, L. S. Zhang, J. Mol. Catal. 2007, 268, 195–200.

[236]   S. O. Alfaro, A. Martínez-de la Cruz, Appl. Catal. A. 2010, 383, 128−133.

[237]   S. C. Zhang, C. Zhang, Y. Man, Y. F. Zhu, J. Solid State Chem. 2005, 178, 3823−3830.

[238]   L. S. Zhang, W. Z. Wang, Z. G. Chen, L. Zhou, H. L. Xu, W. Zhu, J. Mater. Chem. 2007, 17, 2526−2532.

[239]   L. S. Zhang, W. Z. Wang, L. Zhou, H. L. Xu, Small. 2007, 3, 1618−1625.

[240]   M. Shang, W. Z. Wang, S. M. Sun, L. Zhou, L. Zhang, J. Phys. Chem. C. 2008, 112, 10407−10411.

[241]   J. X. Xia, H. M. Li, Z. J. Luo, H. Xu, K. Wang, S. Yin, Y. S. Yan, Mater. Chem. Phys. 2010, 121, 6−9.

[242]   C. X. Xu, X. Wei, Y. M. Guo, H. Q. Wu, Z. H. Ren, G. Xu, G. Shen, G. R. Han, Mater. Res. Bull. 2009, 44, 1635−1641.

[243]   C. Y. Wang, H. Zhang, F. Li, L. Y. Zhu, Environ. Sci. Technol. 2010, 44, 6843−6848.

[244]   H. B. Fu, W. Q. Yao, L. W. Zhang, Y. F. Zhu, Mater. Res. Bull. 2008, 43, 2617−2625.

[245]   H. B. Fu, L. W. Zhang, W. Q. Yao, Y. F. Zhu, Appl. Catal. B. 2006, 66, 100−110.

[246]   C. Zhang, Y. F. Zhu, Chem. Mater. 2005, 17, 3537−3545.

[247]   H. B. Fu, C. S. Pan, W. Q. Yao, Y. F. Zhu, J. Phys. Chem. B. 2005, 109, 22432−22439.

[248]   Y. Tian, G. M. Hua, W. Xu, N. Li, M. Fang, L. D. Zhang, J. Alloys Compd. 2011, 509, 724−730.

[249]   F. Amano, K. Nogami, R. Abe, B. Ohtani, Chem. Lett. 2007, 36, 1314−1315.

[250]   F. Amano, K. Nogami, R. Abe, B. Ohtani, J. Phys. Chem. C. 2008, 112, 9320−9326.

[251]   F. Amano, K. Nogami, R. Abe, B. Ohtani, J. Phys. Chem. C. 2009, 113, 1536−1542.

[252]   F. Amano, K. Nogami, R. Abe, M. Tanaka, B. Ohtani, Langmuir 2010, 26, 7174−7180.

[253]   S. W. Liu, J. G. Yu, J. Solid State Chem. 2008, 181,1048−1055.

[254]   L. Z. Zhang, J. C. Yu, Chem. Commun. 2003, 16, 2078−2079.

[255]   D. R. Rolison, Science. 2003, 299, 1698−1701.

[256]   F. Amano, A. Yamakata, K. Nogami, M. Osawa, B. Ohtani, J. Am. Chem. Soc. 2008, 130, 17650−17651.

[257]   Y. Zhou, Z. Tian, Z. Zhao, Q. Liu, J. Kou, X. Chen, J. Gao, S. Yan, Z. Zou, ACS Appl. Mater. Interfaces. 2011, 3, 3594−3601.

[258]   J. Rotmensch, J. L. Whitlock, M. L. Dietz, J. J. Hines, R. C. Reba, E. P. Horwitz, P. V. Harper, Abstr. Pap. Am. Chem. Soc. 1998, 216, U926.

[259]   G. G. Briand, N. Burford, Chem. Rev. 1999, 99, 2601−2657.

[260] S. K. Poznyak, A. I. Kulak, Electrochim. Acta. 1990, 35, 1941-1948.

[261] K. L. Zhang, C. M. Liu, F. Q. Huang, C. Zheng, W. D. Wang, Appl. Catal. B. 2006, 68, 125–129.

[262] L. J. Zhao, X. C. Zhang, C. M. Fan, Z. H. Liang, P. D. Han, Phys. B. 2012, 407, 3364–3370.

[263] X. C. Zhang, L. J. Zhao, C. M. Fan, Z. H. Liang, P. D. Han, Comput. Mater. Sci. 2012, 61, 180–184.

[264] H. J. Zhang, L. Liu, Z. Zhou, RSC Adv. 2012, 2, 9224–9229.

[265] W. C. Wang, W. J. Yang, R. Chen, X. B. Duan, Y. L. Tian, D. W. Zeng, B. Shan, Phys. Chem. Chem. Phys. 2012, 14, 2450–2454.

[266] H. J. Zhang, L. Liu, Z. Zhou, Phys. Chem. Chem. Phys. 2012, 14, 1286–1292.

[267] M. L. Guan, C. Xiao, J. Zhang, S. J. Fan, R. An, Q. M. Cheng, J. F. Xie, M. Zhou, B. J. Ye, Y. Xie, J. Am. Chem. Soc. 2013, 135, 10411–10417.

[268] Z. H. Ai, W. K. Ho, S. C. Lee, L. Z. Zhang, Environ. Sci. Technol. 2009, 43, 4143–4150.

[269] K. Li, Y. L. Xu, Y. He, C. Yang, Y. L. Wang, J. P. Jia, Environ. Sci. Technol. 2013, 47, 3490–3497.

[270] Y. F. Fang, Y. P. Huang, J. Yang, P. Wang, G. W. Cheng, Environ. Sci. Technol. 2011, 45, 1593–1600.

[271] H. T. Tian, J. W. Li, M. Ge, Y. P Zhao, L. Liu, Catal. Sci. Technol. 2012, 2, 2351–2355.

[272] F. Chen, H. Q. Liu, S. Bagwasi, X. X. Shen, J. L. Zhang, J. Photochem. Photobiol. A. 2010, 215, 76–80.

[273] J. Xu, W. Meng, Y. Zhang, L. Li, C. S. Guo, Appl. Catal. B. 2011, 107, 355–362.

[274] Z. Y. Yu, B. Detlef, D. Ralf, L. Song, L. Q. Lu, J. Mol. Catal. A: Chem. 2012, 365, 1–7.

[275] L. Zhang, W. Z. Wang, S. M. Sun, Y. Y. Sun, E. P. Gao, J. Xu, Appl. Catal. B. 2013, 132, 315–320.

[276] R. S. Yuan, S. L. Fan, H. X. Zhou, Z. X. Ding, S. Lin, Z. H. Li, Z. Z. Zhang, C. Xu, L. Wu, X. X. Wang, X. Z. Fu, Angew. Chem. Int. Ed. 2013, 52, 1035–1039.

[277] N. Kijima, K. Matano, M. Saito, T. Oikawa, T. Konishi, H. Yasuda, T. Sato, Y. Yoshi-mura, Appl. Catal. A. 2001, 206, 237–244.

[278] Kubacka A, Fernández-García M, Colón G. Chem. Rev. 2012, 112, 1555–1614.

[279] Y. Xia, P. Yang, Y. Sun, Y. Wu, B. Mayers, B. Gates, Y. Yin, F. Kim, H. Yan, Adv. Mater. 2003, 15, 353–389.

[280] R. S. Devan, R. A. Patil, J. H. Lin, Y. R. Ma, Adv. Funct. Mater. 2012, 22, 3326–3370.

[281] C. H. Wang, C. L. Shao, Y. C. Liu, L. N. Zhang, Scr. Mater. 2008, 59, 332–335.

[282] R. S. Yuan, C. Lin, B. C. Wu, X. Z. Fu, Eur. J. Inorg. Chem. 2009, 24, 3537–3540.

[283] S. J. Wu, C. Wang, Y. F. Cui, T. M. Wang, B. B. Huang, X. Y. Zhang, X. Y. Qin, P. Brault, Mater. Lett. 2010, 64, 115–118.

[284] Q. H. Wang, K. Kalantar-Zadeh, A. Kis, J. N. Coleman, M. S. Strano, Nat. Nanotechnol. 2012, 7, 699–712.

[285] M. Chhowalla, H. S. Shin, G. Eda, L. Li, K. P. Loh, H. Zhang, Nat. Chem. 2013, 5, 263–275.

[286] M. Q. Zhao, Q. Zhang, J. Q. Huang, F. Wei, Adv. Funct. Mater. 2012, 22, 675–694.

[287] J. H. Han, S. Lee, J. Cheon, Chem. Soc. Rev. 2013, 42, 2581–2591.

[288] K. L. Zhang, C. M. Liu, F. Q. Huang, C. Zheng, W. D. Wang, Appl. Catal. B. 2006, 68, 125–129.

[289] L. Q. Ye, L. Zan, L. Tian, T. Peng, J. Zhang, Chem. Commun. 2011, 47, 6951-6953.

[290] D. Zhang, J. Li, Q. G. Wang, Q. S. Wu, J. Mater. Chem. A. 2013, 1, 8622–8629.

[291] X. F. Chang, J. Huang, C. Cheng, Q. Sui, W. Sha, G. B. Ji, S. B. Deng, G. Yu, Catal. Commun. 2010, 11, 460–464.

[292] X. Chang, M. A. Gondal, A. A. Al-Saadi, M. A. Ali, H. Shen, Q. Zhou, J. Zhang, M. Du, Y. Liu, G. Ji, J. Colloid Interface Sci. 2012, 377, 291–298.

[293] J. Jiang, K. Zhao, X. Y. Xiao, L. Z. Zhang, J. Am. Chem. Soc. 2012, 134, 4473–4476.

[294] J. Y. Xiong, G. Cheng, G. F. Li, F. Qin, R. Chen, RSC Adv. 2011, 1, 1542–1553.

[295] M. Shang, W. Z. Wang, L. Zhang, J. Hazard. Mater. 2009, 167, 803–809.

[296] L. Q. Ye, L. H. Tian, T. Y. Peng, L. Zan, J. Mater. Chem. 2011, 21, 12479–12484.

[297] H. J. Zhang, L. Liu, Z. Zhou, RSC Adv. 2012, 2, 9224–9229.

[298] G. M. Whitesides, B. Grzybowski, Science, 2002, 295, 2418–2421.

[299] M. A. Snyder, M. Tsapatsis, Angew. Chem. Int. Ed. 2007, 46, 7560–7573.

[300] D. R. Rolison, J. W. Long, J. C. Lythe, A. F. Fischer, C. P. Rhodes, T. M. McEvoy, M. E. Bourg, A. M. Lubers, Chem. Soc. Rev. 2009, 38, 226–252.

[301] Y. Li, Z. Y. Fu, B. L. Su, Adv. Funct. Mater. 2012, 22, 4634–4667.

[302] Q. F. Zhang, E. Uchaker, S. L. Candelaria, G. Z. Cao, Chem. Soc. Rev. 2013, 42, 3127–3171.

[303] X. Zhang, Z. H. Ai, F. L. Jia, L. Z. Zhang, J. Phys. Chem. C. 2008, 112, 747–753.

[304] X. Y. Qin, H. F. Cheng, W. J. Wang, B. B. Huang, X. Y. Zhang, Y. Dai, Mater. Lett. 2013, 100, 285–288.

[305] J. X. Xia, J. Zhang, S. Yin, H. M. Li, H. Xu, L. Xu, Q. Zhang, J. Phys. Chem. Solids. 2013, 74, 298–304.

[306] J. M. Song, C. J. Mao, H. L. Niu, Y. H. Shen, S. Y. Zhang, CrystEngComm, 2010, 12, 3875–3881.

[307] L. P. Zhu, G. H. Liao, N. C. Bing, L. L. Wang, Y. Yang, H. Y. Xie, CrystEngComm, 2010, 12, 3791–3796.

[308] S. J. Peng, L. L. Li, P. N. Zhu, Y. Z. Wu, M. Srinivasan, S. G. Mhaisalkar, S. Ramakrishna, Q. Y. Yan, Chem. Asian J. 2013, 8, 258–268.

[309] D. H. Wang, G. Q. Gao, Y. W. Zhang, L. S. Zhou, A. W. Xu, W. Chen, Nanoscale. 2012, 4, 7780–7785.

[310] J. Zhang, F. Shi, J. Lin, D. Chen, J. Gao, Z. Huang, X. Ding, C. Tang, Chem. Mater. 2008, 20, 2937–2941.

[311] Z. H. Ai, W. Ho, S. Lee, L. Z. Zhang, Environ. Sci. Technol. 2009, 43, 4143–4150.

[312] J. Xu, W. Meng, Y. Zhang, L. Li, C. S. Guo, Appl. Catal. B. 2011, 107, 355–362.

[313] H. F. Cheng, B. B. Huang, Z. Y. Wang, X. Y. Qin, X. Y. Zhang, Y. Dai, Chem. Eur. J. 2011, 17, 8039–8043.

[314] Y. J. Chen, M. Wen, Q. S. Wu, CrystEngComm, 2011, 13, 3035–3039.

[315] J. X. Xia, S. Yin, H. M. Li, H. Xu, L. Xu, Y. G. Xu, Dalton Trans. 2011, 40, 5249–5258.

[316] L. Zhang, X. F. Cao, X. T. Chen, Z. L. Xue, J. Colloid Interface Sci. 2011, 354, 630–636.

[317] D. Q. Zhang, M. C. Wen, B. Jiang, G. S. Li, J. C. Yu, J. Hazard. Mater. 2012, 211, 104–111.

[318] Y. C. Feng, L. Li, J. W. Li, J. F. Wang, L. Liu, J. Hazard. Mater. 2011, 192, 538–544.

[319] Y. N. Huo, J. Zhang, M. Miao, Y. Jin, Appl. Catal. B. 2012, 111, 334–341.

[320] H. T. Tian, J. W. Li, M. Ge, Y. P. Zhao, L. Liu, Catal. Sci. Technol. 2012, 2, 2351–2355.

[321] Y. Y. Li, J. S. Wang, H. C. Yao, L. Y. Dang, Z. J. Li, J. Mol. Catal. A: Chem. 2011, 334, 116–122.

[322] J. X. Xia, S. Yin, H. M. Li, H. Xu, Y. S. Yan, Q. Zhang, Langmuir. 2011, 27, 1200–1206.

[323] L. Chen, S. F. Yin, R. Huang, Y. Zhou, S. L. Luo, C. T. Au, Catal. Commun. 2012, 23, 54–57.

[324] K. Zhang, J. Liang, S. Wang, J. Liu, K. X. Ren, X. Zheng, H. Luo, Y. J. Peng, X. Zou, X. Bo, J. H. Li, X. B. Yu, Cryst. Growth Des. 2012, 12, 793–803.

[325] Y. Q. Lei, G. H. Wang, S. Y. Song, W. Q. Fan, M. Pang, J. K. Tang, H. J. Zhang, Dalton Trans. 2010, 39, 3273–3278.

[326] R. Hao, X. Xiao, X. X. Zuo, J. M. Nan, W. D. Zhang, J. Hazard. Mater. 2012, 209, 137–145.

[327] Y. Q. Lei, G. H. Wang, S. Y. Song, W. Q. Fan, H. J. Zhang, CrystEngComm, 2009, 11, 1857–1862.

[328] C. H. Deng, H. M. Guan, Mater. Lett. 2013, 107, 119–122.

[329] G. Cheng, J. Y. Xiong, F. J. Stadler, New J. Chem. 2013, 37, 3207–3213.

[330] X. Xiao, W. D. Zhang, J. Mater. Chem. 2010, 20, 5866–5870.

[331] J. Y. Xiong, Z. B. Jiao, G. X. Lu, W. Ren, J. H. Ye, Y. P. Bi, Chem. Eur. J. 2013, 19, 9472–9475.

[332] J. Jiang, K. Zhao, X. Y. Xiao, L. Z. Zhang, J. Am. Chem. Soc. 2012, 134, 4473–4476.

[333] L. Q. Ye, L. Zan, L. H. Tian, T. Y. Peng, J. J. Zhang, Chem. Commun. 2011, 47, 6951–6953.

[334] L. Q. Ye, K. J. Deng, F. Xu, L. H. Tian, T. Y. Peng, L. Zan, Phys. Chem. Chem. Phys. 2012, 14, 82–85.

[335] J. Jiang, L. Z. Zhang, H. Li, W. W. He, J. J. Yin, Nanoscale. 2013, 5, 10573–10581.

[336] A. Kudo, Y. Miseki, Chem. Soc. Rev. 2009, 38, 253–278.

[337] X. B. Chen, S. S. Mao, Chem. Rev. 2007, 107, 2891–2959.

[338] H. F. Cheng, B. B. Huang, Y Dai, Nanoscale, 2014, 6, 2009–2026

[339] S. Xuan, W. Jiang, X. Gong, Y. Hu, Z. Chen, J. Phys. Chem. C, 2008, 113, 553–558.

[340] Q. Yuan, N. Li, W. C. Geng, Y. Chi, X. T. Li, Mater. Res. Bull. 2012, 47, 2396–2402.

[341] Y. Z. Wang, X. B. Fan, S. L. Wang, G. L. Zhang, F. B. Zhang, Mater. Res. Bull. 2013, 48, 785–789.

[342] B. Cui, H. X. Peng, H. Q. Xia, X. H. Guo, H. L. Guo, Sep. Purif. Technol. 2013, 103, 251–257.

[343] Z. Wang, L. Shen, S. Zhu, Int. J. Photoenergy. 2012, 202, 519–524.

[344] R. Chalasani, S. Vasudevan, ACS Nano, 2013, 7, 4093–4104.

[345] H. Liu, L. Gao, J. Am. Ceram. Soc. 2006, 89, 370–373.

[346] W. Zhou, H. Fu, K. Pan, C. Tian, Y. Qu, P. Lu, C. C. Sun, J. Phys. Chem. C. 2008, 112, 19584-19589.

[347] F. X. Chen, W. Q. Fan, T. Y. Zhou, W. H. Huang, Acta Phys. Chim. Sin. 2013, 29, 167–175.

[348] W. S. Tung, W. A. Daoud, ACS Appl. Mater. Interfaces. 2009, 1, 2453–2461.

[349] B. Palanisamy, C. M. Babu, B. Sundaravel, S. Anandan, V. Murugesan, J. Hazard. Mater. 2013, 23, 233–242.

[350] M. Shang, W. Wang, L. Zhang, S. Sun, L. Wang, L. Zhou, J. Phys. Chem. C, 2009, 113, 14727–14731.

[351] C. Wang, C. Shao, X. Zhang, Y. Liu, Inorg. Chem. 2009, 48, 7261–7268.

[352] E. Gao, W. Wang, M. Shang, J. Xu, Phys. Chem. Chem. Phys. 2011, 13, 2887–2893.

[353] Y. H. Ng, A. Iwase, A. Kudo, R. Amal, J Phys Chem Lett, 2010, 1, 2607–2612.

[354] X. Zhang, L. Z. Zhang, T. F. Xie, D. J. Wang, J. Phys. Chem. C. 2009, 113, 7371–7378.

[355] Y. Li, Y. Liu, E. Uchaker, Q. Zhang, S. Sun, J. Wang, Y. Huang, J. Li, G. Cao, J. Mater. Chem. A. 2013, 1, 7949–7956.

[356] F. D. Gao, D. W. Zeng, Q. W. Huang, S. Q. Tian, C. S. Xie, Phys. Chem. Chem. Phys. 2012, 14, 10572–10578.

[357] Z. H. Ai, W. Ho, S. Lee, J. Phys. Chem. C. 2011, 115, 25330–25337.

[358] X. M. Tu, S. L. Luo, G. X. Chen, J. H. Li, Chem. Eur. J. 2012, 18, 14359–14366.

[359] S. Y. Song, W. Gao, X. Wang, X. Y. Li, D. P. Liu, Y. Xing, H. J. Zhang, Dalton Trans. 2012, 41, 10472–10476.

[360] H. Liu, W. R. Cao, Y. Su, Z. Chen, Y. Wang, J. Colloid Interface Sci. 2013, 398, 161–167.

[361] H. Tada, T. Mitsui, T. Kiyonaga, T. Akita, K. Tanaka, Nat. Mater. 2006, 5, 782–786.

[362] M. R. Elahifard, S. Rahimnejad, S. Haghighi, M. R. Gholami, J. Am. Chem. Soc. 2007, 129, 9552–9553.

[363] H. L. Wang, L. S. Zhang, Z. G. Chen, J. Q. Hu, S. J. Li, Z. H. Wang, J. S. Liu, X. C. Wang, Chem. Soc. Rev. 2014, 43, 5234–5244.

[364] L. S. Zhang, K. H. Wong, Z. G. Chen, J. C. Yu, J. C. Zhao, C. Hu, C. Y. Chan, P. K. Wong, Appl. Catal. A. 2009, 363,221–229.

[365] W. Xiong, Q. D Zhao, X. Y. Li, D. K. Zhang, Catalysis Communications. 2011, 16, 229–233.

[366] L. Q. Ye, J. Y. Liu, C. Q. Gong, L. H. Tian, T. Y. Peng, L. Zan. ACS Catal. 2012, 2, 1677–1683.

[367]   W. Y. Gao, M. Q. Wang, C. X. Ran, X Yao, H Yang, J Liu, D He, J. B. Bai. Nanoscale. 2014, 21, 5498–508.

[368]   W. Y. Gao, M. Q. Wang, C. X. Ran, L Li, Chem. Commun. 2015, 51, 1709–1712.